

**TOWARDS PICOTESLA SENSITIVITY MAGNETIC SENSOR FOR
TRANSFORMATIONAL BRAIN RESEARCH**

by

Angel Rafael Monroy-Pelaez

A Dissertation

Submitted to the Faculty of Purdue University

In Partial Fulfillment of the Requirements for the degree of

Master of Science in Engineering



School of Materials Engineering

West Lafayette, Indiana

May 2020

**THE PURDUE UNIVERSITY GRADUATE SCHOOL
STATEMENT OF COMMITTEE APPROVAL**

Dr. Ernesto E. Marinero, Chair

School of Materials Science Engineering

Dr. Lia A. Stanciu, co-Chair

School of Materials Science Engineering

Dr. Zhihong Chen

School of Electrical and Computer Engineering

Dr. Zhongming Liu

School of Biomedical Engineering

Approved by:

Dr. David F. Bahr

Dedicated to my parents and sisters

ACKNOWLEDGMENTS

I am thankful to my advisor Dr. Ernesto Marinero, whose guidance and mentoring helped me to move forward past the roadblocks I encountered while working on this challenging project. Without his challenging me I would not have fully realized the new knowledge I was acquiring. Special thanks and most profound appreciation for the support and kind words you and your wife, Dr. Hazel Marinero, gave me when my sister passed away.

To my committee members, Dr. Zhongming Liu, Dr. Zhihong Chen, and Dr. Lia A. Stanciu, thank you for your time, suggestions, and invaluable knowledge. Special thanks to Dr. Stanciu for your help and support in situations when I felt lost, and that enabled me to move forward.

I am thankful to my group members: Dr. Derek Schwanz, you introduced me to the group and was pending on how things were going. Besides being a research peer, you became a good friend; Dr. Andres A. Villa-Pulido, you started the journey with me, and we share many memories, so thanks for being there all the time and also thanks for the spinning classes; Bradley Beauchamp, thank you for your friendship, research talk, and being there for me; Aveek Dutta, thank you for the research talks and nanofabrication advice, which really helped me; Hannah Fowler, Luis Regalado, and Tara Goldberg, thank you for the ideas, research talk, and working with me; Tom Stegall and Keaton Klaff, thank you for working with me and helping me be a better mentor.

I am thankful to Dr. Yong P. Chen for letting me use your laboratory and equipment, and for your time and suggestion; Andres E. Llacsahuanga Allcca, thank you for your friendship, research talks, company while working in the laboratory, ideas, and for introducing me to “La causa de Pollo”; John F Ribeiro, thank you for your friendship, research talks, teaching me how to use the VTI, ideas, and nanofabrication advice,

Thank you, Dr. David B. Janes and Dr. Doosan Back, for introducing me to nanofabrication knowledge, for your time and suggestions, and the work that was done together.

Thank you, Dr. Yi Xuan for helping with the fabrication the CVD graphene magnetometers and Dr. Nithin Raghunathan, for his advice and assistance with device nanofabrication

Thank you, Keith Scott and Ryan Beasley from the ECE workshop, for lending me equipment to perform my research experiments, for letting me work in the workshop, for your time and suggestions.

Special thanks to Consejo Nacional de Ciencia y Tecnologia (CONACYT) for the awarded scholarship for a Ph.D. program.

Special thanks to my family and close friends, for being there in the good times and in the bad ones. Without you the journey would have been tougher.

TABLE OF CONTENTS

LIST OF TABLES	9
LIST OF FIGURES	10
LIST OF SYMBOLS	17
LIST OF ABBREVIATIONS.....	18
ABSTRACT.....	20
1. INTRODUCTION	22
1.1 Motivation.....	22
1.2 Biomagnetism	23
1.3 Neural Activity Source Origin.....	24
1.4 Neural Activity Magnetic Signal Characteristics	26
1.5 Noise Surrounding Magnetic Signals	27
1.6 Extraordinary Magnetoresistance (EMR).....	31
1.7 Mechanisms Affecting Mobility in Graphene	34
1.8 The Pathway Towards Picotesla (pT) and Femtotesla (fT) Sensitivity	36
1.9 Structure of the Dissertation	37
2. FABRICATION OF GRAPHENE-BASED MAGNETOMETERS.....	38
2.1 CVD Graphene–Based Magnetometers	38
2.1.1 CVD graphene transfer process	38
2.1.2 Device fabrication.....	39
2.2 Mechanically Exfoliated Graphene–based Magnetometers.....	40
2.2.1 2D material preparation samples	40
Material characterization.....	44
2.2.2 Device fabrication of h-BN/graphene/h-BN trilayer stacks	46
Hall cross nanofabrication.....	50
EMR device nanofabrication.....	52
2.3 Discussion.....	53
3. ELECTRIC AND MAGNETIC TRANSPORT CHARACTERIZATION OF GRAPHENE-BASED MAGNETOMETERS.....	54
3.1 CVD Graphene–Based Magnetometers	54

3.1.1	Electrical measurement definitions.....	55
3.1.2	Measurements under vacuum conditions.....	57
	Resistivity measurements	58
	Hall-effect measurements.....	59
	EMR measurements	62
3.1.3	Effect of environmental exposure on CVD graphene–based magnetometers	64
3.1.4	Discussion of CVD graphene–based magnetometers.....	67
3.2	Mechanical Exfoliated Graphene-Based Magnetometers.....	70
3.2.1	Experimental definition	70
3.2.2	Measurements under vacuum conditions.....	71
	Resistivity measurements	71
	Hall-effect measurements.....	72
	Noise measurements.....	74
3.2.3	Measurements under ambient conditions	76
	Resistivity measurements	77
	Hall effect measurements	82
	EMR measurements	84
	Noise measurements.....	87
3.2.4	Comparison with relevant published works	93
4.	FINITE ELEMENT MODELING (FEM) OF GRAPHENE-BASED MAGNETOMETERS .	
	98
4.1	Hall-cross Model Definition	98
4.1.1	Benchmarking under vacuum conditions	101
4.1.2	Comparison of model and experimental results for measurements done in ambient conditions.....	107
4.1.3	Modeling results for attaining Hall-cross devices with pT sensitivity	109
4.2	EMR Magnetometer Modeling.....	112
4.2.1	Modeling results for attaining EMR devices with pT sensitivity	114
4.3	Discussion.....	117
5.	CONCLUSIONS	120

APPENDIX A. METHOD FOR FABRICATION OF BUBBLE-FREE GRAPHENE/H-BN STACKS	123
APPENDIX B. MEASUREMENT OF CONTACT RESISTANCE WITH THE TLM METHOD	126
APPENDIX C. EFFECT OF THE SWEEPING RATE OF THE GATE VOLTAGE ON SIGNAL RESPONSE.....	129
APPENDIX D. MAGNETIC RESPONSE OF THE HALL CROSS-DEVICE AND THE EMR DEVICE.....	131
APPENDIX E. NOISE MEASUREMENTS OF THE CVD GRAPHENE EMR DEVICES UNDER AMBIENT CONDITIONS	135
APPENDIX F. COMPARISON OF FEM SIMULATION AND EXPERIMENTAL RESULTS	140
REFERENCES	142
PUBLICATIONS.....	151

LIST OF TABLES

Table 1.1. Summary of published carrier mobility measurements in graphene.	35
Table 3.1 Resistivity measurement results of CVD-grown graphene-based devices employing the PPMS at RT under vacuum conditions.	59
Table 3.2. Magnetic response summary results for CVD graphene-based magnetometers at RT under vacuum conditions.	64
Table 3.3. Summary of resistivity measurements of EMR devices after 24 months of environmental exposure at RT.	65
Table 3.4. Comparison between CVD-graphene magnetometers and an EMR device reported in the literature. The measurements were done under vacuum conditions at RT.	69
Table 3.5. Resistivity measurements for Hall-cross device fabricated from h-BN/graphene/h-BN trilayer structures	71
Table 3.6. Hall-cross device parameters and sensitivities at RT under vacuum conditions.	76
Table 3.7. Resistivity measurements results of the Hall-cross and EMR devices using VTI at RT under ambient conditions.	77
Table 3.8. Transport parameters and noise measurements for trilayer Hall-Cross and EMR devices at RT under ambient conditions.	92
Table 3.9. Comparison of transport parameters and sensitivities between our devices and representative examples from the literature.	94
Table 3.10. Extrapolated values assuming no significant hysteresis on the Hall-cross device. ...	97
Table 4.1. FEM-model inputs to benchmark the simulations with experimental results. The derived values of n_s , μ , and p_s at different applied magnetic fields and currents are the inputs under vacuum and ambient conditions.	101
Table 4.2. EMR device parameters employed for the FEM model simulation and comparison with experimental results	113
Table 4.3. FEM-model simulation results of the Hall cross under vacuum and ambient conditions.	118
Table 4.4. Comparison of FEM simulation results with experiments for EMR devices operating at RT under ambient conditions.	119

LIST OF FIGURES

Fig. 1.1. Processes involved in neural activity. (a) Synaptic activity generates PSP. (Inset) PSP amplitude and time duration. (b) Information is propagated to the next neuron. (Inset) Action potential amplitude and time duration. Figure from Ref. [6] [100], [101] 25

Fig. 1.2. Auditory magnetic response after an applied stimulus as a function in time. Figure from Ref. [6] 26

Fig. 1.3. Comparison between environmental spurious and biological magnetic signals generated by the human body in comparison to the human brain. From Ref. [5]..... 27

Fig. 1.4. (a) MEG 4D neuroimaging system inside a shielded room at Saint Louis University, Missouri, USA. Figure from Ref. [11]. (b) Integrated gradiometer with a flux transformer and the SQUID. Figure from Ref. [9]..... 28

Fig. 1.5. a) Schematic illustration of the OPM sensor operation: the lower figure depicts Larmor precession when an external field is present and the transmitted light is reduced; b) Image of OPM-MEG system on patient head; c) Schematic of the coils confined to 2 planes of a 40 cm^3 region of interest. Ref. [14]..... 30

Fig. 1.6. Schematic of the EMR graphene magnetic sensor. The colors represent: Purple: Si/SO₂ substrate; gray: graphene monolayer; yellow: shunt, current, and voltage leads. The curved arrows depict current, paths in the absence (black) and presence of an external magnetic field perpendicular to the plane of the hybrid structure. Figure from Ref. [1]..... 32

Fig. 1.7. Parameters that affect the EMR effect. (a) The effect of carrier mobility using a vdP geometry at 5 T. Figure from Ref. [36]. (b) The effect of contact resistance using planar and classic geometries at -1 T. Figure from Ref. [37]. 33

Fig. 2.1. Transfer process schematic of CVD graphene monolayer onto a Si/SiO₂ substrate. 39

Fig. 2.2. Fabrication process schematic of EMR and Hall bar devices. 40

Fig. 2.3. Mechanical exfoliation of graphene. a) Mother tape with bulk graphite flakes distributed to cover a large area. b) Steps to peel the new tape from the mother tape. c) Mother tape with five peeled tapes. d) Transfer of mother tape to the target substrate. e) Removal of the mother tape from the substrate while on the hot plate. f) Mother tape for further transfers of graphene flakes. 42

Fig. 2.4. Mechanical exfoliation of h-BN. a) Mother tape with h-BN crystals. b) Mother tape with four peeled tapes. c) Target substrate sitting on the hot plate prior to the final peeling. d) Mother tape ready for further h-BN transfers. 43

Fig. 2.5. Graphene characterization. (a) Optical image of a graphene monolayer (SL) and a trilayer (TL) on Si/SiO₂ substrate. The scale bar is 10 μm . (b) Raman spectrum of monolayer graphene showing the two main peaks at 1580 cm^{-1} (G) and 2690 cm^{-1} (2D). 44

Fig. 2.6. h-BN characterization. (a) Optical microscope image of an h-BN flake. Scale bar 10 μm . (b) Raman spectrum of h-BN samples with its characteristic peak at 1366 cm^{-1} . (c) AFM surface

image of h-BN depicting topography profiles. (d) h-BN flake thickness plots along the line profiles shown in (c). 45

Fig. 2.7. Photograph of the micromanipulator station for heterostructure stacks assembly. 46

Fig. 2.8. Procedure to produce h-BN/graphene/h-BN trilayer structures. (a-b) h-BN top layer pickup by the polymeric stamp by the van der Waals method. (c-d) Graphene pickup by the stamp containing the h-BN cap flake. (f-h) Stamp containing h-BN/G dropped onto the h-BN bottom flake. The black circle shows the localization of the h-BN cap, graphene, and h-BN bottom. Scale bar 200 μm 48

Fig. 2.9. Optical microscope images of the annealing treatment to remove bubbles within graphene's area. (a) Trilayer stack after assembly and after the first annealing process at 400 $^{\circ}\text{C}$. (b) Second annealing at 400 $^{\circ}\text{C}$. (c) Third annealing at 400 $^{\circ}\text{C}$. (d) Fourth annealing at 500 $^{\circ}\text{C}$. (e) Fifth annealing at 600 $^{\circ}\text{C}$. Annealing cycle duration was 4 hrs. in a flowing Ar/H₂ atmosphere (200 sccm). h-BN bottom (blue dashed line), graphene (black dashed line), and hBN cap (yellow dashed line). Scale bar 10 μm 49

Fig. 2.10. Characterization of the h-BN/G/h-BN stack. (a) Optical microscopy image of the stack, h-BN bottom (blue dashed line), graphene (black dashed line), and h-BN top layer (yellow dashed color). The scale bar is 10 μm . (b) Raman spectrum, showing the h-BN main peak at 1366 cm^{-1} and the graphene G and 2D main peaks at 1580 cm^{-1} and 2690 cm^{-1} , respectively. Inset in Fig. 2.10(b) displaying the Raman maps for monolayer graphene (green color) and for the h-BN flakes (red color), the scale bar is 10 μm . (c) AFM surface image indicating the regions of the trilayer from which topography profiles were obtained. (d) Surface profiles showing the thickness of the stack across the profile lines indicated in Fig. 2.10(c). 50

Fig. 2.11. Hall cross fabrication process. (a) Optical microscopy image of the stack covered with MAN4023. h-BN bottom (blue dashed line), graphene (black dashed line), and h-BN cap (red dashed color). (b) Hall cross patterning with e-beam lithography. (c) Hall cross etched exposing graphene edges after using RIE. (d) Optical microscope image of the Hall cross covered with PMMA. (e) PMMA patterning of the metal contacts using EBL. (f) Final Hall cross after metal deposition and lift-off. (a-f) Scale bar 10 μm 52

Fig. 2.12. Optical microscope image of the final EMR device with a metallic shunt after metal deposition and lift-off. Sensing area of 4.5 $\mu\text{m} \times 1.6 \mu\text{m}$ (white dashed rectangle). The scale bar is 10 μm 53

Fig. 3.1. Schematics of CVD graphene devices. (a) Hall bar with a sensing area of 1 mm \times 0.5 mm. (b) EMR device with a sensing area of 2.2 mm \times 1.1 mm. (c) EMR device with a sensing area of 1.2 mm \times 0.6 mm. All devices were fabricated on Si/SiO₂ substrates. The graphene layer is depicted in grey, while the metal contacts are shown in yellow. The sensing area is delineated by the white dashed line. The EMR devices have a metallic shunt (Ti/Au (10 nm/60 nm)) within the graphene area. Labeled numbers as reference for electrical connections. 55

Fig. 3.2. Two-terminal resistance as a function of spacing and twice the TLM contact resistance (R_c) for the EMR1 device (black) and the EMR2 device (blue). Arrows indicated R_c 58

Fig. 3.3. Magnetic response of the Hall bar longitudinal voltage (V_{xx}) as a function of the magnetic field for (a) bottom and (b) upper adjacent voltage tabs. The input current was $10 \mu\text{A}$ and magnetic field sweep was $\pm 5 \text{ T}$. Inset shows the electrical connections configuration. 60

Fig. 3.4. Magnetic response of the Hall bar Hall voltage (V_{xy}) as a function of the magnetic field for (a) first and (b) second bridge voltage tabs. The input current was $10 \mu\text{A}$ and magnetic field sweep was $\pm 5 \text{ T}$. Inset shows the electrical connections configuration. 61

Fig. 3.5. Magnetic response of the (a) EMR1 device and (b) EMR2 device. V_{diff} as a function of applied magnetic field and input current. Inset show the electrical connections configuration. .. 62

Fig. 3.6. Magnetic response of (a) EMR1 device and (b) EMR2 device voltage as a function of the magnetic field after aging time. Applied current, $150 \mu\text{A}$, and magnetic field, $\pm 5 \text{ T}$. The inset shows the electrical connections configuration. 66

Fig. 3.7. Devices fabricated using h-BN/graphene/h-BN trilayers. (a) Hall cross device, sensing area of $1.65 \mu\text{m} \times 1.65 \mu\text{m}$. (b) EMR device schematic with sensing area of $4.5 \mu\text{m} \times 1.6 \mu\text{m}$. The color reference is graphene (grey), h-BN (green), and the metal contacts (yellow). Label numbers are reference for describing the electrical connections during device measurements. .. 70

Fig. 3.8. Voltage response at RT of the Hall-cross device as a function of applied magnetic field at (a) $\pm 50 \text{ mT}$ and (b) $\pm 5000 \text{ mT}$. Measurements conducted injected an AC current of $1 \mu\text{A}$ and without V_g . Arrows indicate the direction of the magnetic field sweep. Insets show the tabs configuration used for the measurements. 73

Fig. 3.9. Hall cross noise response at RT under vacuum conditions. (a) Hall cross schematic of the electrical connections used for the measurements. (b) PSD as a function of f . (c) B_{min} as a function of f . Measurement conditions: injected AC current $1 \mu\text{A}$, absence of the magnetic field, and without gate voltage. The red dashed line illustrates $1/f$ dependency. 75

Fig. 3.10. Ambient condition experimental setup (a) lateral view and (b) upper view. A permanent magnet is used to induce a magnetic field of $\pm 50 \text{ mT}$ 77

Fig. 3.11. Transfer curves measured at orthogonal channels of the Hall cross in ambient conditions and without applied magnetic field. (a) Longitudinal direction, CNP at $V_g = -0.1 \text{ V}$ and $V_g = 1.8 \text{ V}$. (b) Transversal direction, CNP at $V_g = 0.8 \text{ V}$ and $V_g = 2.3 \text{ V}$. The applied current was $1 \mu\text{A}$. The arrows show the direction of gate voltage sweep. The inset shows the electrical connections used for the measurements. 79

Fig. 3.12. Hall cross longitudinal orthogonal direction sweeping rates of gate voltage dependence. (a-d) R as a function of V_g . Applied current, $1 \mu\text{A}$. Sweep moves from positive to negative polarity (red line) and sweeps back to positive (blue line). Inset shows the schematic of the electrical connections used for the measurements. 81

Fig. 3.13. Hall cross average R_s as a function of V_g . employing the van der Pauw configuration. Applied current, $1 \mu\text{A}$. CNP at $V_g = 1.9 \text{ V}$ 82

Fig. 3.14. Voltage response of the Hall cross at RT under ambient conditions at 0 and $\pm 50 \text{ mT}$. (a) V as a function of V_g . (b) μ as a function of n_s . (c) S_I as a function of V_g at V_{H+} ($V_H (50\text{mT}) - V_H (0\text{mT})$, blue line) and V_{H-} ($V_H (-50\text{mT}) - V_H (0\text{mT})$, red line). The injection current was $100 \mu\text{A}$. Fixed magnetic fields of -50 mT (blue line), 0 mT (black line), and 50 mT (red line). Inset show

the electrical connections used for the measurements. From the schematic, I_b on the left side, V_H on the top side, and V_g on the right side..... 83

Fig. 3.15. Magnetic response of the EMR device at RT under ambient conditions. The applied gate voltage is swept from -20 V to 20 V for (a, c and d) whereas for (b, d and e) it is swept from -40V to 20V. (a) V_{diff} vs. V_g ; (b) V_{diff} vs. V_g for the wider gate voltage range (-40 V to 20 V); (c) μ as a function of n_s ; (d) μ as a function of n_s ; (e) S_I as a function of V_g . and (f) S_I as a function of V_g . V_{H+} (V_H (50mT) – V_H (0mT), blue line) and V_{H-} (V_H (-50mT) – V_H (0mT), red line) is presented in (e) & (f). Applied current, 100 μ A. Fixed magnetic fields of -50 mT (blue line), 0 mT (black line), and 50 mT (red line). Inset show the electrical connections used for the measurements. From the schematic, I_b on the left side, V_H on the top side, and V_g on the right side. 85

Fig. 3.16. Hall cross noise response at different gate voltages at RT under ambient conditions. PSD as a function of V_g . at (a) 10 Hz and at (b) 3 kHz. B_{min} as a function of V_g at (c) 10 Hz and at (d) 3 kHz. Applied currents, 1 μ A (square markers), 10 μ A (circle markers), and 100 μ A (diamond markers). The blank (filled) markers correspond to the frequency of 10 Hz (3 kHz).. 87

Fig. 3.17. a). PSD of B_{min} vs. f . Values are obtained at the gate bias voltage at which B_{min} minimizes. (b) B_{min} vs. f for different injected currents, 1 μ A (red), 10 μ A (blue), and 100 μ A (black). Reference of the 1/f noise dependency (red dashed line). 88

Fig. 3.18. EMR noise response vs. gate voltages at RT under ambient conditions. PSD vs. V_g . at (a) 10 Hz and at (b) 3 kHz. B_{min} vs. V_g at (c) 10 Hz and at (d) 3 kHz. Injected currents, 1 μ A (squares), 10 μ A (circles), and 100 μ A (diamonds). The blank (filled) markers correspond to the frequency of 10 Hz (3 kHz). 89

Fig. 4.1. FEM Hall cross model definition. (a) 2D geometry showing the h-BN/G/h-BN stack (grey) and the metal contacts (yellow). (b) Model boundary conditions: applied current (I_b) (red line), ground (purple line), contact resistance (p_s) (blue lines), acquired potential difference (V_{diff}) (green and orange line). (c) Mesh generated for the Hall cross..... 99

Fig. 4.2. FEM Hall simulations of the surface electric potential (E) distribution along the Hall cross arms in the presence of external fields perpendicular to the plane of the figure of: (a) -50 mT, (b) 50 mT, and (c) 0 mT. Current flow direction streamlines (black lines). (d) Electric Potential (E) distribution along the arm orthogonal to the current flow. Applied current, 1 μ A. 102

Fig. 4.3. Simulation of the magnetic response of the Hall cross under vacuum conditions at RT. (a) Longitudinal direction V as a function of B . (b) Transversal direction V as a function of B . Applied current 1 μ A and magnetic field ± 50 mT..... 103

Fig. 4.4. FEM results comparison with of experimental data at RT under vacuum conditions. V vs of B of (a) dataset 1, (b) dataset 2 and (c) simulated average. Applied current, 1 μ A and magnetic field, ± 50 mT. Dataset values are given in Table 4.1..... 104

Fig. 4.5. FEM Hall simulations of the surface electric potential (E) distribution along the Hall cross arms in the presence of external fields perpendicular to the plane of the figure of: (a) -5 T and (b) 5 T. (a-b) Current flow direction streamlines (black lines). (d) Electric Potential (E) distribution along the arm orthogonal to the current flow. Applied current, 1 μ A..... 105

Fig. 4.6. FEM Hall simulations of voltage vs. applied magnetic field for: (a) field measured perpendicular to the injected current path and (b) along the current path. (c) Comparison between simulation and experiment of V vs. B measured perpendicular to the current path..... 107

Fig. 4.7. Comparison of FEM results with experiments: (a) V vs. V_g as a function of applied magnetic field: $B = -50$ mT, 0 mT, and 50 mT (blue, black, and red lines); simulation $B = -50$ mT, 0 mT, and 50 mT (orange, purple, and cyan line). (b) μ vs. n_s : experimental data (blue circles) and simulation data (red diamonds). (c) Absolute S_I vs. V_g . Experimental data (blue and red lines) and simulation data (cyan and orange lines). Applied current, 1 μ A. 108

Fig. 4.8. Simulation magnetic response of the Hall cross-device at RT to predict the pT sensitivity. V as function of B for (a) $n_s = 1.3 \times 10^{11}$ cm⁻², $\mu = 180,000$ cm²/Vs, and $p_s = 150$ Ω μ m and for (b) $n_s = 1.66 \times 10^{10}$ cm⁻², $\mu = 245,000$ cm²/Vs, and $p_s = 30$ Ω μ m. Applied current, 100 μ A and magnetic field, ± 50 mT. 111

Fig. 4.9. Schematics of FEM modeling of the EMR graphene-hBN magnetometer. (a) 2D geometry, h-BN/G/h-BN (grey), metallic shunt and metal contacts (yellow), and sensing area (cyan). (b) Model boundary conditions: applied current (I_b) (red line), ground (purple line), contact resistance (p_s) (blue lines), potential difference (V_{diff}) (green and orange lines). (c) Mesh employed for the EMR device simulation. 112

Fig. 4.10. Comparison of FEM results with experiments: (a) V vs. V_g as a function of applied magnetic field: $B = -50$ mT, 0 mT, and 50 mT (blue, black, and red lines). Simulation results $B = -50$ mT, 0 mT, and 50 mT (orange, purple, and cyan lines). (b) μ as a function of n_s . Experimental data (blue circles) and simulation data (red diamonds). (c) S_I vs. V_g . Experimental data (blue and red lines) and simulation data (cyan and orange lines). Applied current, 100 μ A. 114

Fig. 4.11. FEM simulation of surface potentials and current paths for an EMR magnetometer with $n_s \sim 1.3 \times 10^{11}$ cm⁻², $\mu \sim 180,000$ cm²/Vs, and $p_s = 150$ Ω μ m. Surface electric potential (E) distribution along with the device at (a) $B = -50$ mT, (b) $B = 50$ mT, and (c) $B = 0$ mT. (a-c) Streamlines showing the current flow path direction (black lines)..... 115

Fig. 4.12. Simulation of the magnetic response of an EMR device at with (a) $n_s = 1.3 \times 10^{11}$ cm⁻², $\mu = 180,000$ cm²/Vs, and $p_s = 150$ Ω μ m and for (b) $n_s = 1.66 \times 10^{10}$ cm⁻², $\mu = 245,000$ cm²/Vs, and $p_s = 30$ Ω μ m. Applied current, 100 μ A..... 116

Fig. A.1. Procedure to encapsulated graphene on h-BN. (a-d) h-BN cap pickup by the polymeric stamp by the van der Waals method. (e-h) Graphene pickup by the stamp containing h-BN. (i-l) h-BN bottom pickup by the stamp containing h-BN/G stack. (m-p) Transfer of the stack to substrate with alignment marks. The black circle shows the localization of the h-BN cap, graphene, and h-BN bottom. Scale bar 200 μ m.....124

Fig. A.1. Characterization of the h-BN/G/h-BN stack. (a) Optical microscopy image of the stack: the h-BN bottom layer is outlined by with the blue dashed line, the graphene layer with the black dashed line, and h-BN cap with the red dashed line. The scale bar is 10 μ m. (b) Raman spectrum showing the h-BN main peak at 1366 cm⁻¹ and the graphene G and 2D main peaks at 1580 cm⁻¹ and 2690 cm⁻¹. The inset displays the Raman map identifying the graphene (green) and h-BN

(red) flakes. The scale bar 10 μm . (c) AFM surface image showing the regions used to measure topography profiles. (d) Topography profiles across the line regions shown in (c).....125

Fig. B. 1. Two-terminal resistance vs. contact spacing yields the value (at intercept) of twice the contact resistance (R_c). The measurements correspond to EMR1 (black) and EMR2 devices (blue) measured 24 months after fabrication. Arrows indicate the value of $2xR_c$126

Fig. B. 2. Two-terminal resistance vs. contact spacing yields the value (at intercept) of twice the contact resistance (R_c). The measurements correspond to the Hall cross-device at RT under vacuum (black) and ambient (blue) conditions. Arrows indicate the value of $2xR_c$127

Fig. B. 3. Two-terminal resistance vs. contact spacing yields the value (at intercept) of twice the contact resistance (R_c). The measurements correspond to an unaged EMR device at RT under ambient conditions Arrows indicate the value of $2xR_c$128

Fig. C.1. Hall cross device resistance vs. gate voltage as a function of the gate-voltage sweep rate measured perpendicular to the injection current channel. The input current was 10 μA and the gate voltage is swept from positive (blue line) to negative polarity (red line) and repeated. The inset shows the electrical connections used for the measurements.....129

Fig. C.2. Hall cross device resistance vs gate voltage as a function of the gate-voltage sweep rate measured perpendicular to the injection current channel. The input current was 100 μA and the gate voltage is swept from positive (blue line) to negative polarity (red line) and repeated. The inset shows the electrical connections used for the measurements.....130

Fig. D.1. Magnetic response of the Hall cross at RT under ambient conditions. (a) V vs. V_g at three different values of the applied magnetic field: -50 mT (blue line), 0 mT (black line), and 50 mT (red line). (b) Correlation of μ and n_s . (c) S_I as a function of V_g at V_{H+} (V_H (50 mT) – V_H (0 mT), blue line) and V_{H-} (V_H (-50 mT) – V_H (0 mT), red line). The injection current was 1 μA . Inset shows the electrical connections used for the measurements. From the schematic, I_b on the left side, V_H on the top side, and V_g on the right side.....131

Fig. D.2. Magnetic response of the Hall cross at RT under ambient conditions. (a) V vs. V_g at three different values of the applied magnetic field: -50 mT (blue line), 0 mT (black line), and 50 mT (red line) (b) correlation of μ and n_s . (c) S_I as a function of V_g at V_{H+} (V_H (50 mT) – V_H (0 mT), blue line) and V_{H-} (V_H (-50 mT) – V_H (0 mT), red line). The injection current was 10 μA . Inset show the electrical connections used for the measurements. From the schematic, I_b on the left side, V_H on the top side, and V_g on the right side.....132

Fig. D. 3. Magnetic response of an EMR device at RT under ambient conditions. (a) V vs. V_g at three different values of the applied magnetic field: -50 mT (blue line), 0 mT (black line), and 50 mT (red line). The gate voltage bias range in (b) is twice that of (a). The correlation between μ and n_s is presented in (c) and (d) and are derived from the measurements in (a) & (b). The dependence of S_I vs. V_g at V_{H+} (V_H (50 mT) – V_H (0 mT), blue line) and V_{H-} (V_H (-50 mT) – V_H (0 mT), red line) is presented in (e) & (f). The injection current was 1 μA . Inset show the electrical

connections used for the measurements. From the schematic, I_b on the left side, V_H on the top side, and V_g on the right side.....133

Fig. D. 4. Magnetic response of an EMR device at RT under ambient conditions. (a) V vs. V_g at three different values of the applied magnetic field: -50 mT (blue line), 0 mT (black line), and 50 mT (red line). The gate voltage bias range in (b) is twice that of (a). The correlation between μ and n_s is presented in (c) and (d) and are derived from the measurements in (a) & (b). The dependence of S_I vs. V_g at V_{H+} (V_H (50 mT) – V_H (0 mT), blue line) and V_{H-} (V_H (-50 mT) – V_H (0 mT), red line) is presented in (e) & (f). The injection current was 10 μ A. Inset shows the electrical connections used for the measurements. From the schematic, I_b on the left side, V_H on the top side, and V_g on the right side.....134

Fig. E. 1. Experimental setup for noise measurements in ambient conditions at RT. (a) Electrical circuit diagram showing the utilized components utilized, including signal amplification of 100x. (b) Photograph of the circuit employed to perform noise measurements of EMR1 and EMR2 devices.....136

Fig. E. 2. Noise measurements for the EMR1 device, performed at RT and ambient conditions without applied magnetic field. This device was measured after being stored in the lab environment for 24 months. (a) PSD vs f . (b) B_{min} vs. f . The injection currents were: 1 μ A (blue trace), 10 μ A (red trace) and 100 μ A (black trace). The red dashed line is drawn to illustrate I/f dependency.....137

Fig. E. 3. Noise measurements for the EMR2 device, performed at RT and ambient conditions without applied magnetic field. This device was measured after being stored in the lab environment for 24 months. (a) PSD vs f . (b) B_{min} vs. f . The injection currents were: 1 μ A (blue trace), 10 μ A (red trace) and 100 μ A (black trace). The red dashed line is drawn to illustrate I/f dependency.....139

Fig. F. 1. Comparison of FEM results with experiments: (a) V vs. V_g as a function of applied magnetic field: $B = -50$ mT, 0 mT, and 50 mT (blue, black, and red lines). Simulation results $B = -50$ mT, 0 mT, and 50 mT (orange, purple, and cyan lines). (b) μ as a function of n_s . Experimental data (blue circles) and simulation data (red diamonds). (c) S_I vs, of V_g . Experimental data (blue and red lines) and simulation data (cyan and orange lines). Applied current, 10 μ A.....140

Fig. F. 2. Comparison of FEM results with experiments: (a) V vs. V_g as a function of applied magnetic field: $B = -50$ mT, 0 mT, and 50 mT (blue, black, and red lines). Simulation results $B = -50$ mT, 0 mT, and 50 mT (orange, purple, and cyan lines). (b) μ as a function of n_s . Experimental data (blue circles) and simulation data (red diamonds). (c) S_I vs, of V_g . Experimental data (blue and red lines) and simulation data (cyan and orange lines). Applied current, 100 μ A.....141

LIST OF SYMBOLS

I_b	Bias current
n_s	Carrier density
μ	Carrier mobility
ρ_s	Contact resistance
S_I	Current sensitivity
q	Electron charge
V_g	Gate voltage
R_H	Hall resistance
V_H	Hall voltage
hrs.	Hours
$R_{\text{longitudinal}}$	Longitudinal resistance
B	Magnetic field
B_{min}	Magnetic resolution
min	Minutes
PSD	Noise power spectral density
V_{diff}	Potential difference
R	Resistance
ρ	Resistivity
f_s	Sample frequency
s	Seconds
R_s	Sheet resistance
R_c	TLM contact resistance
$R_{\text{transversal}}$	Transversal resistance
S_v	Voltage sensitivity

LIST OF ABBREVIATIONS

AC	Alternating current
AFM	Atomic Force Microscopy
CVD	Chemical Vapor Deposition
CNP	Charge-Neutral Dirac Point
DI	Deionized
ECE	Electrical and Computer Engineering
ETO	Electrical Transport Option
ECG	Electrocardiography
EEG	Electroencephalography
EMG	Electromyography
EBL	Electron Beam Lithography
EMR	Extraordinary Magnetoresistance
FFT	Fast Fourier Transformation
fT	femtotesla
FEM	Finite Element Modeling
G	Graphene
hBN	hexagonal Boron Nitride
HCP	Human Connectome Project
INAMP	Instrumentation amplifier
IPA	Isopropyl alcohol
MRI	Magnetic Resonance Imaging
MCG	Magnetocardiography
MEG	Magnetoencephalography
MMG	Magnetomyography
MR	Magnetoresistive
mT	millitesla
mV	millivolt
nT	nanotesla
OPMs	Optically pumped magnetometers

PPMS	Physical Properties Measurement System
pT	picotesla
PC	Polycarbonate
PDMS	Polydimethylsiloxane
PSP	Postsynaptic potential
RIE	Reactive Ion Etching
RT	Room Temperature
SERF	Spin-exchange relaxation free
SL	Single Layer
sccm	Standard cubic centimeters per minute
SQUIDs	Superconducting Quantum Interference Devices
TMAH	Tetramethylammonium hydroxide
TLM	Transfer Length Method
TL	Trilayer
2D	Two-dimensional
UV	Ultraviolet
XPS	X-ray photoelectron spectroscopy
vdP	van der Pauw
VTI	Variable temperature insert

ABSTRACT

During neural activity, action potentials travel down axons, generating effective charge current pulses, which are central in neuron-to-neuron communication. Consequently, said current pulses generate associated magnetic fields with amplitudes on the order of picotesla (pT) and femtotesla (fT) and durations of 10's of ms. Magnetoencephalography (MEG) is a technique used to measure the cortical magnetic fields associated with neural activity. MEG limitations include the inability to detect signals from deeper regions of the brain, the need to house the equipment in special magnetically shielded rooms to cancel out environmental noise, and the use of superconducting magnets, requiring cryogenic temperatures, bringing opportunities for new magnetic sensors to overcome these limitations and to further advance neuroscience. An extraordinary magnetoresistance (EMR) tunable graphene magnetometer could potentially achieve this goal. Its advantages are linear response at room temperature (RT), sensitivity enhancement owing to combination of geometric and Hall effects, microscale size to place the sensor closer to the source or macroscale size for large source area, and noise and sensitivity tailoring. The magnetic sensitivity of EMR sensors is, among others, strongly dependent on the charge mobility of the sensing graphene layer. Mechanisms affecting the carrier mobility in graphene monolayers include interactions between the substrate and graphene, such as electron-phonon scattering, charge impurities, and surface roughness. The present work reviews and proposes a material set for increasing graphene mobility, thus providing a pathway towards pT and fT detection. The successful fabrication of large-size magnetic sensors employing CVD graphene is described, as well as the fabrication of trilayer magnetic sensors employing mechanical exfoliation of h-BN and graphene. The magneto-transport response of CVD graphene Hall bar and EMR magnetic sensors is compared to that obtained in equivalent trilayer devices. The sensor response characteristics are reported, and a determination is provided for key performance parameters such as current and voltage sensitivity and magnetic resolution. These parameters crucially depend on the material's intrinsic properties. The Hall cross magnetic sensor here reported has a magnetic sensitivity of ~ 600 nanotesla (nT). We find that the attained sensitivity of the devices here reported is limited by contaminants on the graphene surface, which negatively impact carrier mobility and carrier density, and by high contact resistance of $\sim 2.7 \text{ k}\Omega \mu\text{m}$ at the metallic contacts. Reducing the contact resistance to $< 150 \Omega \mu\text{m}$ and

eliminating surface contamination, as discussed in this work, paves the way towards pT and ultimately fT sensitivity using these novel magnetic sensors. Finite element modeling (FEM) is used to simulate the sensor response, which agrees with experimental data with an error of less than 3%. This enables the prediction and optimization of the magnetic sensor performance as a function of material parameters and fabrication changes. Predictive studies indicate that an EMR magnetic sensor could attain a sensitivity of $1.9 \text{ nT}/\sqrt{\text{Hz}}$ employing graphene with carrier mobilities of $180,000 \text{ cm}^2/\text{Vs}$, carrier densities of $1.3 \times 10^{11} \text{ cm}^{-2}$ and a device contact resistance of $150 \text{ } \Omega \text{ } \mu\text{m}$. This sensitivity increments to $443 \text{ pT}/\sqrt{\text{Hz}}$ if the mobility is $245,000 \text{ cm}^2/\text{Vs}$, carrier density is $1.6 \times 10^{10} \text{ cm}^{-2}$, and a lower contact resistance of $30 \text{ } \Omega \text{ } \mu\text{m}$. Such devices could readily be deployed in wearable devices to detect biomagnetic signals originating from the human heart and skeletal muscles and for developing advanced human-machine interfaces.

1. INTRODUCTION

This chapter describes the processes responsible for the generation of picotesla (pT) and femtotesla (fT) magnetic fields arising from neural activity, as well as the noise factors hindering the detection of such ultra-weak signals. Additionally, two noninvasive technologies that are currently employed for monitoring such magnetic fields and their limitations are outlined. To circumvent the inherent problems with the above referenced techniques, a graphene-based magnetic sensor whose response could potentially achieve pT sensitivity is described.

1.1 Motivation

The human brain's ability to process, store, and retrieve information relies on neural activity and communication. During neural activity, pulses of electrical current that are generated by ion transport transmit information, and consequently, said current pulses generate associated magnetic fields. The amplitude of these magnetic fields is of the order of fT and currently can be studied only in clinical environments, utilizing special ultra-sensitive equipment that cancels out ambient magnetic signals by housing the sensor devices in magnetically-shielded room environments.

Magnetoencephalography (MEG) employing superconducting quantum interference devices (SQUIDS) is a noninvasive technology available only in a few laboratories around the world. Among its limitations are its intrusiveness that requires patient immobilization and insertion into hardware comprising superconducting magnets and cryo-refrigeration. Whereas MEG attains fT sensitivity, its disadvantages include its inability to directly measure neural activity below the brain cortex, its limited spatial and temporal resolution, and the prohibitive cost of the instrumentation. MEG utilizing optically pumped magnetometers (OPMs) is also a noninvasive technique that allows head movement owing to a wearable setup of sensors. Limitations are its inability to detect magnetic fields from deeper parts of the brain, and the requirement magnetically shielded environments.

An extraordinary magnetoresistance (EMR) tunable nanoscale graphene magnetometer [1] has demonstrated sensitivities at the millitesla (mT) level at room temperature. Some of the key parameters determining the sensitivity of this type of device are the carrier mobility and density

as well as the contact resistance. The carrier mobilities of the graphene device described in [1] were reported to be in the range of 1,000 – 5,000 cm²/Vs at room temperature (RT). Recent progress in graphene synthesis has yielded mobilities at RT of ~ 180,000 cm²/Vs, thereby paving the way for dramatically incrementing the sensitivity of EMR magnetometers, potentially into to the pT and fT regions. The sensitivity and frequency response of these graphene-based EMR devices can be tuned by applying a voltage perpendicular to the film plane (gate voltage) to shift the Fermi level with respect to the Dirac point. The sensor frequency response spans the sub-Hz to GHz range, and the spacing between the voltage leads in the four terminal configuration of the device, I_{in} - V_1 - I_{out} - V_2 (I_{in} , I_{out} are the input and exit current leads and V_1 , V_2 are the voltage leads) defines its spatial resolution and can be adjusted continuously from the nano- to the macroscale. These unique attributes make this magnetic sensor ideally suited for the fabrication of wearable device arrays to study brain function and cognitive behavior non-intrusively without requiring cryogenic temperatures or magnetically shielded rooms.

Among the novel contributions that the proposed arrays could provide to neuroscience is the study in real time and noninvasively of local and distributed synchronized responses of the brain to external stimuli. Arrays can be designed as gradiometer arrays to sense signals arising from sub-cortical areas. In addition, the proposed sensors are applicable for the detection of other biological magnetic signals arising from organs such as the human heart and muscles. Conversely, the sensor operation can potentially be modified to provide localized magnetic fields to stimulate neural response at the cellular and neural network levels.

1.2 Biomagnetism

Biomagnetism involves weak magnetic fields arising from different organ activity of the human body. The physiological origin comes from electrical activity generated by ion currents, which produce associated magnetic fields and body-surface electric fields. The latter were introduced earlier as medical diagnostic tools and widely used over the years for recording the activity of organs such as heart, muscle, and brain; the techniques employed for such studies are electrocardiography (ECG), electromyography (EMG), and electroencephalography (EEG), respectively. Magnetocardiography (MCG), magnetomyography (MMG), and magnetoencephalography (MEG) are the techniques used to record the corresponding magnetic field activity of the aforementioned organs.

The development of MEG has become an essential tool to further neuroscience in the understanding of healthy and diseased brain functionality by tracking the activity and cessation of electrophysiological networks in real time with high spatial precision [2], [3]. Brain biomagnetism enables the localization of magnetic field sources based on measurements of field gradient distribution. Superposing the brain's functional information measured by MEG with structural images obtained with magnetic resonance imaging (MRI) provides source location maps, which are used in clinical practice, for example, to localize epileptic foci.

1.3 Neural Activity Source Origin

Neurons communicate information to other neurons by electrical impulses. Such impulses occur when the transmembrane potential, that is, the electrical potential of the interior of cells relative to its surroundings, changes [4]. Neural activity begins when it's the resting potential of -70 millivolt (mV) changes upon response to a stimulus. A graded potential, the postsynaptic potential (PSP), spreads from the stimulated site and decreases in amplitude with distance. If the PSP surpasses a threshold of -55 mV, an action potential is triggered.

In synaptic activity (illustrated in Fig. 1.1(a)), the synaptic knob depolarizes upon arrival of the action potential, and the voltage-gated calcium channels are activated, letting Ca^{2+} ions flow into the knob. Neurotransmitters are released and diffuse towards the receptors of the postsynaptic cell, generating the PSP.

During the action potential (illustrated in Fig. 1.1(b)), sodium channels are activated, allowing Na^{+} ions to diffuse into the cell owing to electrical attraction and the development of a chemical gradient concentration. The transmembrane potential becomes more electrically positive until it reaches 30 mV (sodium equilibrium potential). At this point, the sodium channels inactivate, and voltage-gated potassium channels are triggered, allowing K^{+} ions to diffuse outside the cell. At -70 mV, the potassium channels begin to close, but not all channels close simultaneously, producing hyperpolarization because K^{+} ions continue flowing until the potential reaches -90 mV (potassium equilibrium potential).

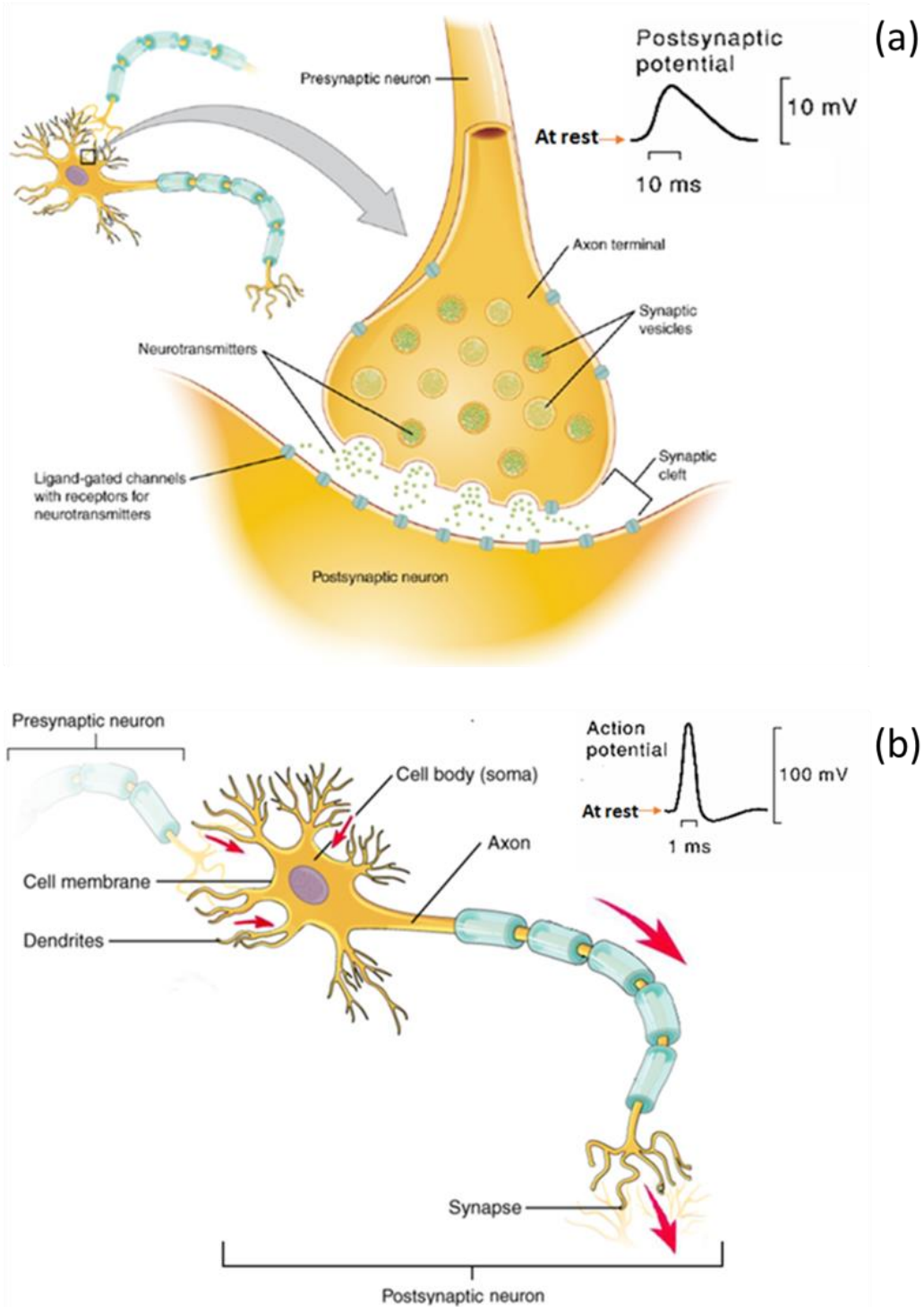


Fig. 1.1. Processes involved in neural activity. (a) Synaptic activity generates PSP. (Inset) PSP amplitude and time duration. (b) Information is propagated to the next neuron. (Inset) Action potential amplitude and time duration. Figure from Ref. [6] [100], [101]

1.4 Neural Activity Magnetic Signal Characteristics

Action potentials and PSP are the sources of electrical currents that produce the associated magnetic fields. Collective neuron responses generate magnetic fields on the order of pT and fT at frequencies ranging from a fraction of one Hz to kHz. The higher response observed is in the alpha rhythm, a brain wave that originates in relaxation states with closed eyes, with an amplitude of ~ 1 pT, whereas visual, auditory, and sensorial responses are weaker, having amplitudes of tens to hundreds of fT [5]. Fig. 1.2 illustrates the magnetic response near the auditory cortex after a sound stimulus.

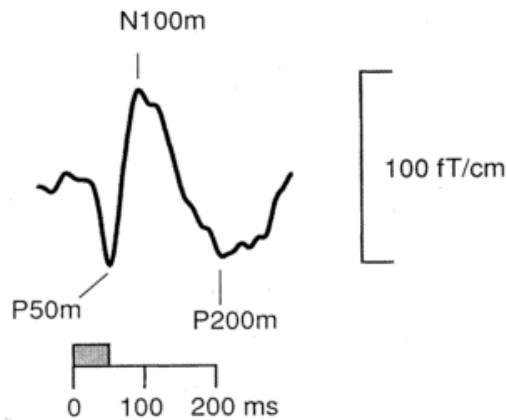


Fig. 1.2. Auditory magnetic response after an applied stimulus as a function in time. Figure from Ref. [6]

Hämäläinen et al. [6] proposed a current-dipole framework to model a PSP event and conclude that a single neuron response has a magnetic dipole strength of 20 fA.m. On the other hand, a quadrupole model yields an action potential with a 100 fA.m dipole strength for a single response. The authors state that in 1 mm^2 there are approximately 10^5 neurons, and their synchronous response increases the PSP dipole strength to 20 nA.m and that of the action potential to 100 nA.m. The magnitude of the magnetic fields associated with these dipole strengths at the scalp is 29 nT and 143 nT, respectively. In principle, this response should yield detectable magnetic signals. Nevertheless, owing to partial cancellations of magnetic fields from adjacent regions, a larger active area must be measured.

Actual MEG measurements provide a more quantitative estimate of the signals generated in the activated area [7]. For example, the primary motor cortex activity is prominent at 20 Hz, and changes in its level are used as indicators of its functional state. Results from studies of motor

cortex activity at 20 Hz shows that EMG and MEG signals are coherent during isometric contraction of hand and foot muscles. The magnitude of the signal activity for this motor activity is ~ 300 fT, and MEG is employed to detect and identify its source location.

1.5 Noise Surrounding Magnetic Signals

The noise factors in measuring magnetic fields from neural activity arise from contributions from the human body and the environment. The combined noise contributions from these sources are seven to nine orders of magnitude stronger than brain magnetic signals. The primary sources of the environmental disturbances are the magnetic field of the earth and urban noise, such as vibrations and power lines. The noise from within the body, like eyes, heart, and muscle, is up to four orders of magnitude stronger. Therefore, reducing the noise below the expected environmental and biomagnetic signals is a problem that needs to be addressed for successful sensor operation. Fig. 1.3 displays a comparison of noise factors at the fT level.

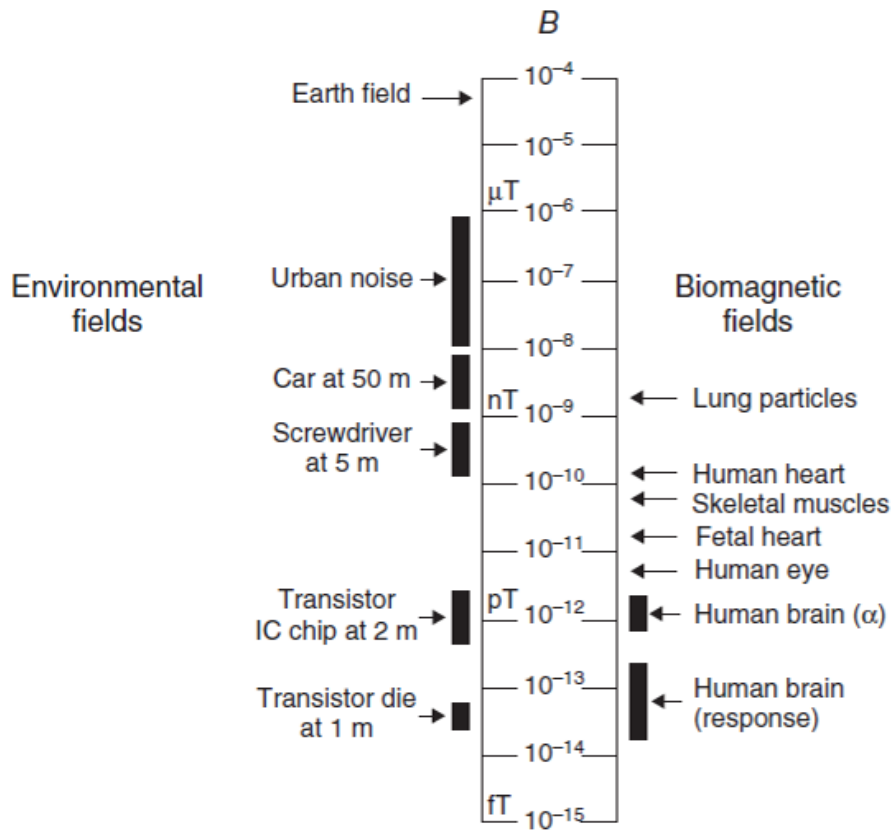


Fig. 1.3. Comparison between environmental spurious and biological magnetic signals generated by the human body in comparison to the human brain. From Ref. [5]

In MEG, magnetic fields are detected using superconducting quantum interference devices (SQUIDs) that need to be operated at cryogenic temperatures (4.2K). The SQUID magnetometer sensing areas are in the cm^2 scale; to improve signal/noise ratio, a superconductive flux transformer with a large area is used to gather the external magnetic flux to be measured. The size of the SQUID chip is in \sim tens of mm^2 where the diameter of the SQUID loop is 0.1 mm, while the flux transformer diameter is larger than 10 mm; see Fig. 1.4(b). Then, by induction, the input is transferred to the SQUID sensors, providing a significant improvement in its sensitivity.

Most MEG equipment utilizes integrated gradiometers [8] to cancel noise by measuring the difference in magnetic fields between SQUID coils connected in series. The pick-up coil (lower coil in Fig. 1.4(b)) is closer to the source of the signal, while the reference coil (upper coil in Fig. 1.4(b)) compensates for variations in background noise. When the signal of interest arises, the pick-up coil change of field will be greater compared to the reference coil, producing a net change in the output. Additionally, the usage of magnetically shielded rooms [8] equipped with Faraday cages (see Fig. 1.4(a)), reject the environmental noise, which is the dominant factor of the total root mean square (RMS) noise contributions [9] to the sensed signal.

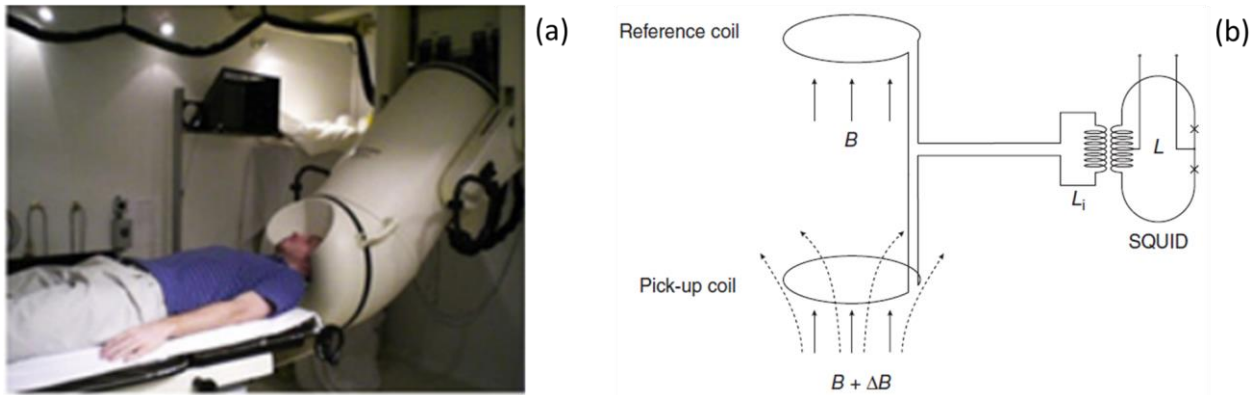


Fig. 1.4. (a) MEG 4D neuroimaging system inside a shielded room at Saint Louis University, Missouri, USA. Figure from Ref. [11]. (b) Integrated gradiometer with a flux transformer and the SQUID. Figure from Ref. [9].

The detection of magnetic fields employing MEG-SQUIDs is reviewed by Aine, C. J. [10], showing early sensory studies and clinical applications. Some example studies include evoked responses in the auditory and visual cortex, sensorimotor response during motor tasks, disabilities in language function, examination of the auditory cortex in Alzheimer's disease and schizophrenia patients, and characterization of brain development in fetuses, neonates, and

infants. Lastly, using the dipole model allows pre-surgical mapping of the somatosensory cortex and localization of interictal epileptic foci in epilepsy patients. These are examples of contributions that MEG has made to neuroscience studies that other imaging techniques could not provide.

Larson-Prior et al. [11], as part of an effort known as the Human Connectome Project (HCP), to map the structure and functionality of the human brain, reported that MEG is employed to provide information of dynamic brain network connectivity. Resting-stage and task-evoked MEG data are processed and analyzed using pipelines for calculating functional connectivity matrices and mapped in anatomical representations. The results from the HCP are available to the research community and relevant to new investigators in the field.

In a study reported by Liu et al. [12], MEG data from eyes-open and eyes-closed wakefulness and light sleep were recorded and analyzed to identify correlation with coherent spontaneous BOLD-fMRI signals. Results show spatio-temporal properties like ultraslow (<0.1 Hz) spontaneous power modulation between opposite hemisphere regions (large-scale synchrony) and power modulations in the inter-hemispheric synchronization. The latter is also revealed in resting-state fMRI, while the first mimics the spontaneous fMRI signal. In addition, the authors discuss issues with MEG limitations regarding spatial specificity owing to the overlapping of signals that originate from different brain regions, resulting in interference effects. Therefore, magnetometers capable of overcoming spatial specificity are highly desirable and valuable for identifying synchrony from specific regions of the brain.

Optically pumped magnetometers (OPM) are capable of measuring fT signals without the need for cryogenic cooling and rely on spectroscopic properties of alkali metals such as K, Rb, and Cs, and they operate in the spin-exchange relaxation free (SERF) regimen [13]. A glass cell contains one of these alkali metals in its vapor phase. The cell is heated at temperatures between $150\text{ }^{\circ}\text{C}$ and $200\text{ }^{\circ}\text{C}$ to provide high vapor densities. A circularly polarized laser beam of the correct wavelength induces atomic electronic transitions to specific magnetic states; following photon emission, the electrons relax to lower energy states. The light transmitted by the gas vapor is measured by a photodetector. In the absence of a magnetic field, the laser-light transmission is a maximum (see schematic representation of the OPM principles in Fig 1.5(a) top). However, a magnetic field perpendicular to the laser beam causes Larmor precession, which changes the direction of the spin moments and results in a drop of the light transmission

[14]; see Fig. 1.5(a) bottom. Progress in the development of OPMs [15]–[17] has made them suitable for MEG measurements [18]–[20]. Boto et al. [14] reported a wearable OPM-MEG that allows head movement in a volume of 40 cm^3 . Interference from the earth’s field is canceled with a set of bi-planar electromagnetic coils designed to generate fields equal and opposite to that of the earth. Coil details are shown in Fig. 1.5(b), three coils generate spatially uniform fields in B_x , B_y , and B_z , while two coils are employed to remove $\delta B_x/\delta z$ and $\delta B_z/\delta z$, designed on two $1.6 \times 1.6 \text{ m}^2$ planes.

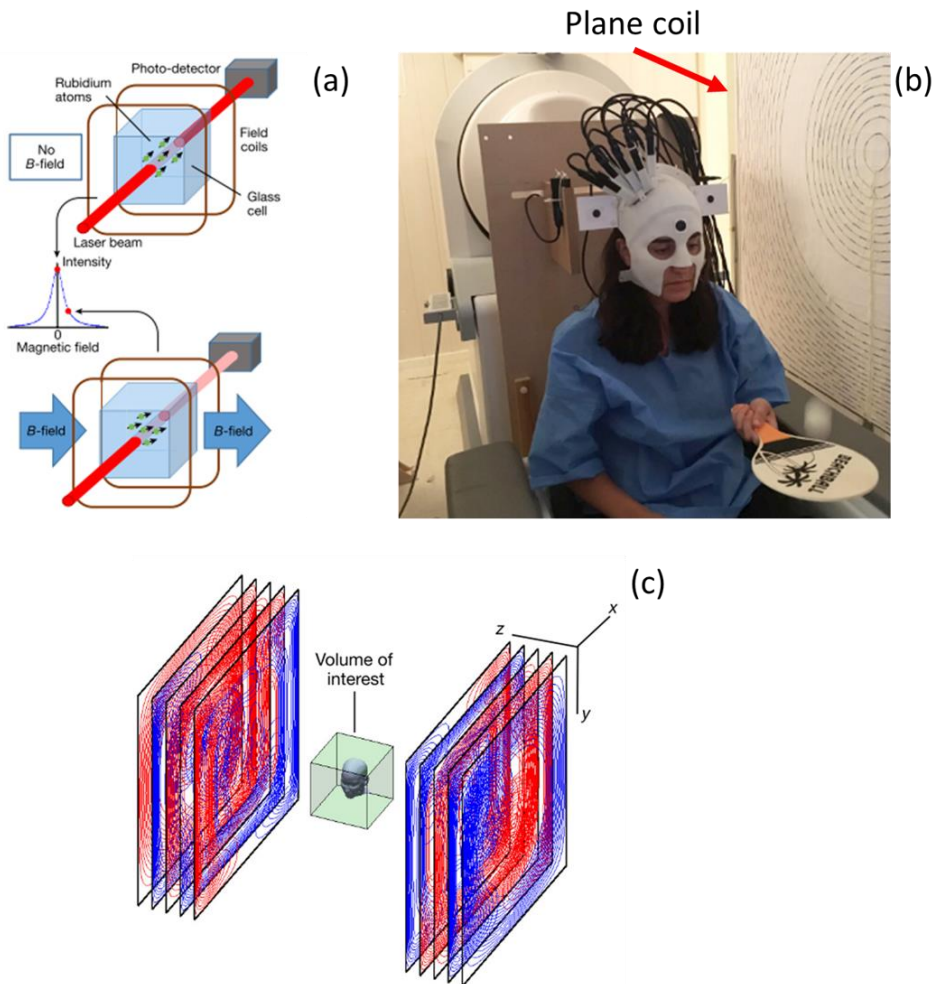


Fig. 1.5. a) Schematic illustration of the OPM sensor operation: the lower figure depicts Larmor precession when an external field is present and the transmitted light is reduced; b) Image of OPM-MEG system on patient head; c) Schematic of the coils confined to 2 planes of a 40 cm^3 region of interest. Ref. [14]

1.6 Extraordinary Magnetoresistance (EMR)

Solin et al. [21] discovered that metals included within nonmagnetic semiconductor materials exhibit an enhancement in their magnetoresistance. Their experiment used a symmetric van der Pauw (vdP) disk geometry and different filling factors between the semiconductor and the metallic inclusion radii. Results show that a filling factor of 12/16 produced the highest MR response because the current that passes through the device is deflected from the metallic inclusion to the semiconductor region on account of the Lorentz force when a magnetic field perpendicular to the current plane is applied. Further investigation on the MR showed that in linear geometries, a considerable response, named by the authors as extraordinary magnetoresistance, is attained as a result of the increment of the Hall angle in high-mobility quantum-well semiconductor structures [22].

Graphene is a monolayer, two-dimensional (2D) honeycomb lattice of carbon atoms whose remarkable transport properties were first reported by Novoselov et al. [23] in 2004. Its unique electronic [24]–[27], mechanical [28], thermal [29]–[32], and optical [33], [34] properties make it a promising candidate for technological applications. The graphene-based sensor first reported by Pisana et al. [1] is an EMR sensor with linear geometry. Its structure consists of an n-doped Si substrate that provides a gate voltage to graphene, covered with 300 nm of SiO₂ as an insulator layer, upon which an exfoliated monolayer of graphene was transferred. The device is completed by depositing a layer of Ta/Au as a shunt and nanofabricating the current and voltage leads. Ta is an adhesion-promoting layer for Au deposited onto graphene.

Advantages of the EMR graphene magnetic sensor over other MR devices include the ability to tune its sensitivity and SNR by applying a gate voltage to change the band gap in graphene [23], RT operation from sub-Hz to GHz frequencies, sensitivity improvements through a combination of geometric and Hall effects [35], and ability to select the size and geometric arrangement of current leads and voltage measurement tabs. Fig. 1.6 provides a schematic diagram of the device and the flow of the current in the absence and presence of a magnetic field applied perpendicular to the plane of the figure. Note that the sensor area is defined by the size of the graphene region between the voltage tabs.

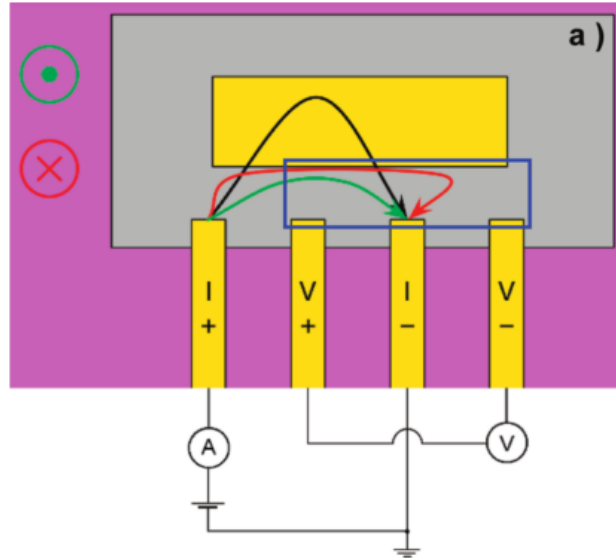


Fig. 1.6. Schematic of the EMR graphene magnetic sensor. The colors represent: Purple: Si/SO₂ substrate; gray: graphene monolayer; yellow: shunt, current, and voltage leads. The curved arrows depict current, paths in the absence (black) and presence of an external magnetic field perpendicular to the plane of the hybrid structure. Figure from Ref. [1].

As stated earlier, the graphene sensors reported by Pisana et al. [1] had carrier mobilities ranging from 1,000 – 5,000 cm²/Vs and contact resistances $\sim 10^{-6} \Omega\text{cm}^2$, thus providing magnetic sensitivities in the sub-mT regime. In order to increase the sensitivity of the EMR graphene sensor for pT and fT detection, carrier mobility, contact resistance, and noise reduction need to be largely improved. Concerning the carrier mobility, Fig. 1.7(a) displays the simulation results obtained by Hewett et al. [36] regarding the effect of mobility on the EMR response in a device with vdP geometry. For the highest mobility transport channel (200,000 cm²/Vs), the magnetoresistance rapidly saturates in the presence of small applied magnetic fields (~ 0.25 T) owing to the attainment of the maximum value of the Hall angle. El-Ahmar et al. [37] reported simulation results of the effect of contact resistance (p_s) on the EMR response in devices with a classic or a planar geometry in the presence of an applied magnetic field of -1 T. Their results are shown in Fig. 1.7(b). In both geometries, the EMR effect diminishes above $p_s = 10^{-6} \Omega\text{m}^2$ owing to current charges not fully deflected from the metallic region. Conversely, the current deflection by the Lorentz force saturates below $10^{-8} \Omega\text{m}^2$. Thus, for the highest sensitivity in graphene-based sensors the desirable contact resistance should $< 10^{-9} \Omega\text{m}^2$.

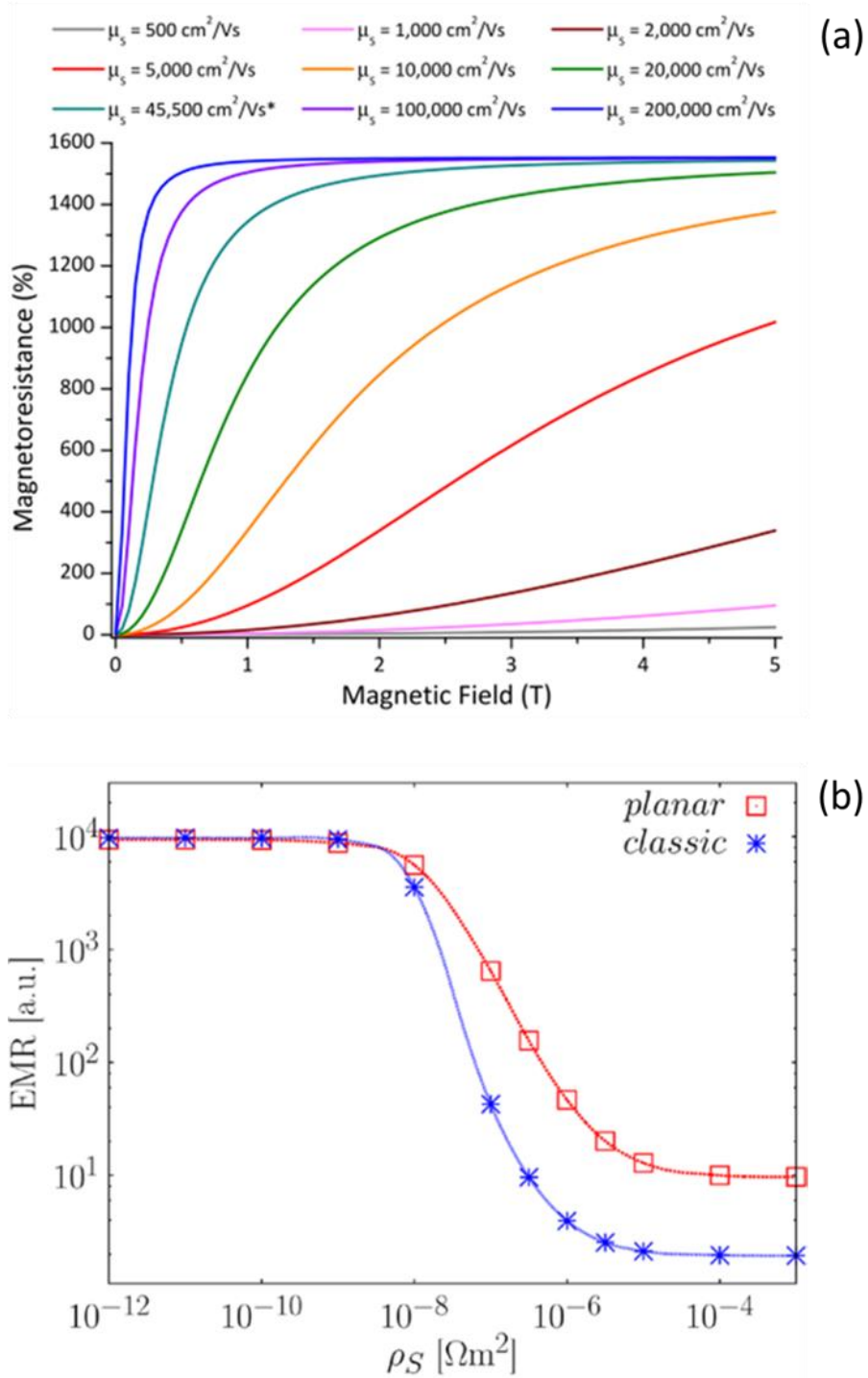


Fig. 1.7. Parameters that affect the EMR effect. (a) The effect of carrier mobility using a vdP geometry at 5 T. Figure from Ref. [36]. (b) The effect of contact resistance using planar and classic geometries at -1 T. Figure from Ref. [37].

1.7 Mechanisms Affecting Mobility in Graphene

The factors impacting the carrier mobility in suspended and supported graphene are the following. The mobility in suspended graphene is affected mainly by graphite defects and has a weak dependence on temperature, remaining high even at room temperature [24]. For multiple layers of graphene, carrier mobilities of around 15,000 cm²/Vs, and 60,000 cm²/Vs at 300K and 4K, respectively have been reported [23]. Additionally, graphene residual impurities or defects on its surface hinder mobility. Mobility in supported graphene is dominated by interactions between the substrate and graphene, which include electron-phonon interactions and scattering due to interface roughness [38].

In the case of our devices, the charge carrier interactions at the interface between graphene and the SiO₂ surface need to be considered. The transfer of graphene onto the SiO₂ surface, which is rougher than the graphene surface, results in roughness and deformation of the graphene overlayer [39]. Another source that limits the mobility of supported graphene layers is electron-phonon scattering [40], which is dependent on temperature. At room temperature, the motion of the atoms increases the probability of a scattering event, and collisions between electrons and phonons result in a decrease of mobility. Charge impurities on the surface of the substrate produce Coulomb scattering, which is most dominant at low temperatures [41].

Significant progress has been made in recent years to improve the mobility of supported graphene; this is an essential step for microelectronic applications of graphene. Table 1.1 summarizes recent published results aimed at improving supported-graphene mobility. The most promising results from the perspective of the development of the fT EMR sensor pertain to the exfoliation of graphene on hexagonal boron nitride (h-BN). The high mobility in this system is attributed to the reduction of electron-phonon scattering at the interface between h-BN and graphene owing to its atomically flat topography and the absence of charged impurity sites. Phonon-electron interactions at the interface are dominant only at elevated temperatures owing to the higher energies of the phonon modes. The small lattice mismatch between the two materials also provides a smooth interface free of corrugations [42]. Therefore, in this work, we have built devices for brain-sensing applications utilizing h-BN-supported graphene.

Table 1.1. Summary of published carrier mobility measurements in graphene.

Fabrication	Carrier mobility [cm ² /Vs]	Carrier density [cm ⁻²]	Temperature	Magnetic Field
Suspended graphene [43], [44]	60,000 to 120,000 230,000	2×10 ¹¹	~5 to 240 K	~250 to 700 mT
hBN/graphene [45]	55,000 to 125,000 18,000 to 46,000 274,000	4.3×10 ¹⁰ 7×10 ¹¹ 0.8×10 ¹⁰	RT RT 4.2 K	500 mT to 8 T
hBN/graphene [46]	21,000	1.5×10 ¹²	RT	0 to 40 mT
CVD graphene [47]	30,000 to 50,000	5×10 ¹¹	1.6 K	9 T
hBN/graphene/hBN [48]	140,000 40,000	0.2×10 ¹² 4.5×10 ¹²	RT RT	
hBN/graphene/hBN [49]	-	-	RT	-50 to 50 mT
hBN/graphene/hBN [50]	180,000 1.8×10 ⁶	~0.13×10 ¹² ~0.13×10 ¹²	RT 9 K	0.5 T

1.8 The Pathway Towards Picotesla (pT) and Femtotesla (fT) Sensitivity

High mobility is of paramount importance to achieve high sensitivity in graphene-based magnetic sensors, as discussed in Reference [36] and illustrated in Fig. 1.7(a) where a maximum response is attained for a mobility of 200,000 cm²/Vs at 0.25 T. Furthermore, a trilayer structure of h-BN/graphene/h-BN–supported on Si/SiO₂ provided mobilities of ~140,000 cm²/Vs and carrier densities of ~2×10¹¹ cm⁻². A magnetic sensor employing such trilayer structure exhibited a sensitivity of 50 nT/√Hz [48], [49]. As discussed in [50], further improvements in mobility (180,000 cm²/Vs) with low carrier densities (1.3×10¹¹ cm⁻²) are attainable by ensuring higher-quality interfaces between h-BN and graphene. Likewise, the attainment of low values of contact resistance values ~10⁻¹⁴ Ωm² (150 Ω μm) are reported in Reference [48].

Predictive studies using a FEM model, presented in chapter 4, indicate that the Hall-cross devices fabricated in this work could attain at RT a sensitivity of 2.1 nT/√Hz (180,000 cm²/Vs) and 639 pT/√Hz (245,000 cm²/Vs). Furthermore, the corresponding EMR device can achieve sensitivities of 1.9 nT/√Hz (180,000 cm²/Vs) and 443 pT/√Hz (245,000 cm²/Vs). The increased EMR device sensitivity over the Hall-cross device is due to the combinations of geometric and Hall effects.

The approach to cancel biomagnetic and environmental magnetic noise is to take advantage of the EMR graphene-based magnetometer ultrafast response. To this end, the magnetometer will be operated in pulsed-current mode. The pulse duration and frequency will be adapted to the signal of interest and detection will be synchronized with the pulse current frequency to eliminate asynchronous noise. This type of detection will result in significant suppression of the background noise, as the interference signals of interest are either continuous or have a different frequency signature.

1.9 Structure of the Dissertation

The work in this dissertation focuses on the enhancement of the magnetic sensitivity of graphene-based magnetometers for the detection of biological magnetic-field signals, in particular from ionic currents from neural activity. Chapter 1 provides an overview of the origin of the magnetic signals and associated noise factors and outlines noninvasive technologies that are capable of detecting such weak signals as well as their limitations. It presents material parameters that control the carrier mobility of the EMR graphene magnetometer needed for high magnetic sensitivity. Chapter 2 describes the fabrication process of graphene-based magnetometers employing graphene obtained from mechanical exfoliation and from chemical vapor deposition (CVD) growth. The latter permits studies of large populations of neurons because it provides large-size graphene monolayers. Exfoliation provides high-quality graphene with high mobilities, and in combination with exfoliated h-BN, the magnetic sensitivity can be significantly enhanced. The fabrication of Hall-bar, Hall-cross, and EMR devices is presented and their signal response is compared. Chapter 3 describes the electrical and magnetic transport characterization of the fabricated graphene-based magnetometers. It provides characterization data for Hall-bar and EMR devices fabricated from CVD-growth graphene and data for Hall-cross and EMR devices fabricated from mechanically exfoliated graphene. It presents results from resistivity, magnetoresistance, Hall-effect, and noise measurements. It compares and discusses device signal response, current and voltage sensitivities, and magnetic resolution, which depend strongly on carrier density and carrier mobility. Chapter 4 presents finite element modeling (FEM) of graphene-based magnetometers to allow studies of device behavior and performance as a function of material parameters. It also provides experimental and simulation results for benchmarking device response, since an agreement with experimental results is essential to trust the model in order to predict the optimization of future Hall-bar, Hall –cross, and EMR devices. In this chapter, results using the FEM model are presented for parameters required to achieve pT sensitivity. Finally, Chapter 5 presents the conclusions and outlines future work to develop graphene-based sensors suitable for neuroscience applications.

2. FABRICATION OF GRAPHENE-BASED MAGNETOMETERS

This chapter presents the methodology and techniques used for the fabrication of graphene-based magnetic sensors. Devices were fabricated employing graphene grown by chemical vapor deposition (CVD) and by mechanical exfoliation.

2.1 CVD Graphene-Based Magnetometers

CVD growth of graphene on Cu foil substrates [51] provides large-area single layers, permitting the fabrication of large devices for the study of large populations of interacting neurons. From a sensor perspective, comparing the signal response from small and large EMR devices enables an assessment of the device linearity response and comparison with simpler Hall-bar devices

2.1.1 CVD graphene transfer process

The transfer process of a commercial CVD graphene monolayer grown on copper foil (from ACS Material[®]) onto a Si/SiO₂ substrate is illustrated in Fig. 2.1. The figure shows the cross-section of a 10-mm² graphene layer on the Cu substrate. This is first spin-coated with polymethyl methacrylate (PMMA), a positive photoresist (PMMA 495 A4). Next, the sample is submerged in a FeCl etching solution for 24 hrs. to etch out the copper foil. Thereafter the graphene is transferred from the etching solution into a deionized (DI) water bath for 10 min to clean; the water bath process is repeated twice more. Afterward, the sample is transferred from DI water to HCl for final cleaning of any remnant copper for 10 min, followed by a final DI rinse. The CVD graphene is then placed on top of the Si/SiO₂ substrate and annealed at 220°C.

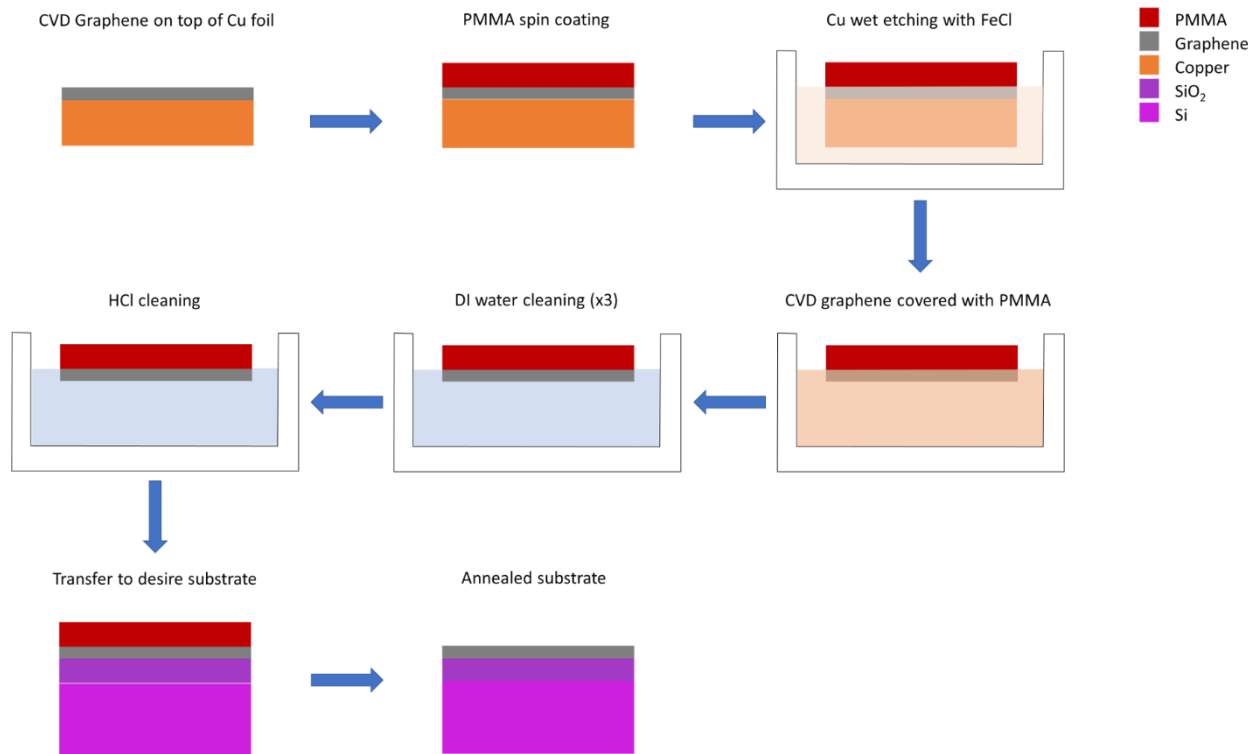


Fig. 2.1. Transfer process schematic of CVD graphene monolayer onto a Si/SiO₂ substrate.

2.1.2 Device fabrication

The fabrication process of EMR and Hall-bar devices (see Fig. 2.2) starts by spin coating PMMA onto the transferred graphene layer at 3000 rpm for 45 s; the resist is then baked on a hot plate for 2 min at 130 °C. An ultraviolet (UV) photolithography tool (MJB 3 Mask Aligner, from Karl Suss) was employed to pattern the PMMA to define the shape of the EMR and Hall-bar devices. Next, graphene is etched in a reactive ion etching (RIE) plasma tech system (RIE-80, from Oxford Instruments) using the following recipe: O₂ gas flow rate 50 sccm, 100 W etch power and a pressure of 50 mTorr (6.6 Pa) for 30 s. After exposure, PMMA is removed with acetone, and subsequently, PMMA is spin-coated onto the patterned structure as described above. A second photolithography step patterning is next conducted to define the metal contacts of the devices. Next, metal deposition of Ti (5 nm)/Au (90 nm) contacts is performed in a Lesker electron beam evaporator (multiple components, from Kurt J. Lesker Company®). The final step is to lift off the excess metal layer.

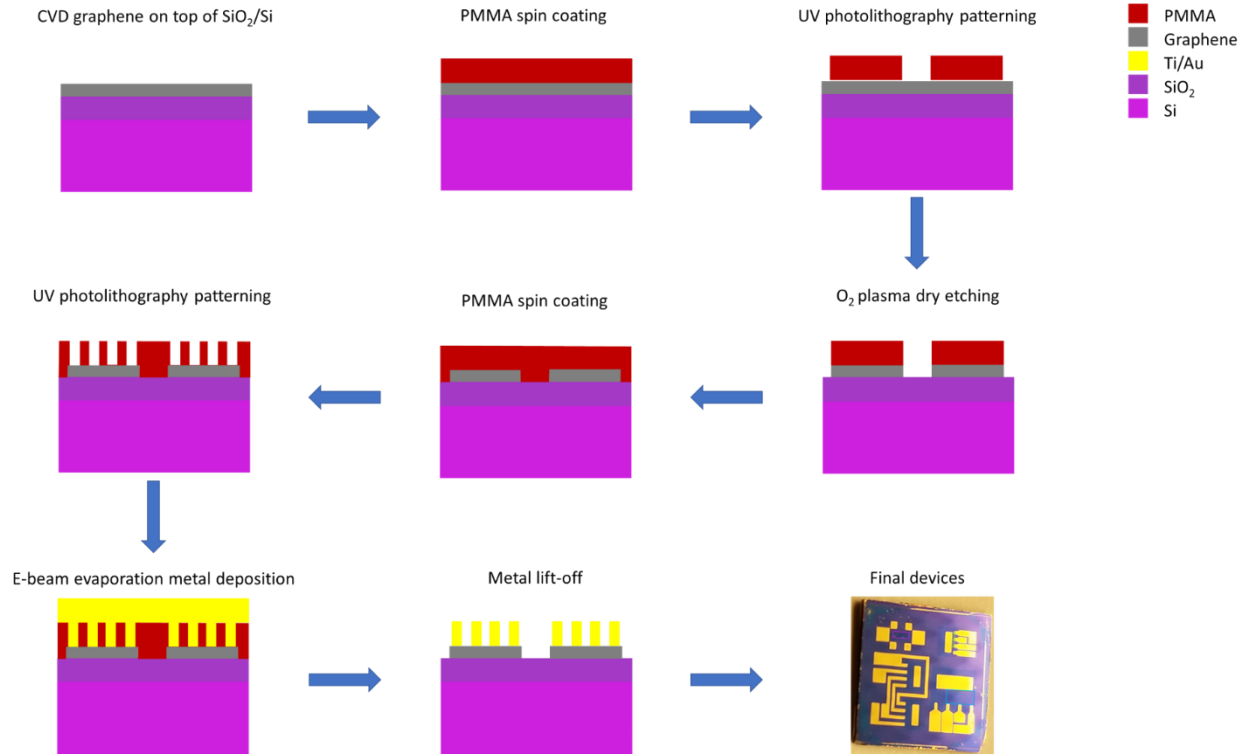


Fig. 2.2. Fabrication process schematic of EMR and Hall bar devices.

2.2 Mechanically Exfoliated Graphene-based Magnetometers

Mechanical exfoliation of bulk graphite with adhesive tape yields atomically thick graphene layers. Suspended graphene obtained by this method yields superior-quality layers with ballistic mobilities measured at 60 K of up to 1,000,000 cm²/Vs [52], [53]. As shown in Table 1.1, supported graphene on h-BN exhibits the highest mobilities measured at 300K. Therefore, mechanically exfoliated graphene and h-BN are employed in this work to fabricate magnetic sensors with enhanced sensitivity.

2.2.1 2D material preparation samples

Graphene (G) is obtained by mechanical exfoliation of Kish graphite [54] (from Covalent Materials Corp.) using scotch tape (from 3M[®]). Several bulk graphite flakes are first placed on a mother tape, as illustrated in Fig. 2.3(a). Then, another clean tape is used to cover the mother tape. Contact is ensured by pressing the tape using a cotton swab to rub the clean tape to ensure uniform adherence of the tapes. The reason to use a clear new tape is to prevent adhesive

contamination on the graphene surface, which happens frequently when the same tape is reused to do the peelings. Next, the top tape is slowly peeled, as indicated in Fig. 2.3(b), and the process is repeated four to five times. The graphite flakes exhibit a shiny gray color, which indicates that they are getting thinner. Fig.2.3(c) displays the mother tape and the subsequently peeled tapes. Each tape shows less adhered material. Too many peeling steps produce smaller flakes and decrease the yield of graphene monolayers.

After the final exfoliation step, the mother tape is pressed onto an acid (piranha) solution-cleaned Si/SiO₂ (285 nm) substrate, as illustrated in Fig. 2.3(d). Next, the substrate with the mother tape is placed on a hot plate for 4 min at ~ 80 °C. While on the hot plate, the mother tape is peeled off slowly (see Fig. 2.3(e)) leaving graphene layers on the substrate. This method facilitates the transfer of $\geq 30 \mu\text{m}$ size monolayers of graphene onto the substrate. The peeled mother tape can be re-used for further exfoliation and transfer of graphene flakes, as shown in Fig. 2.3(f).

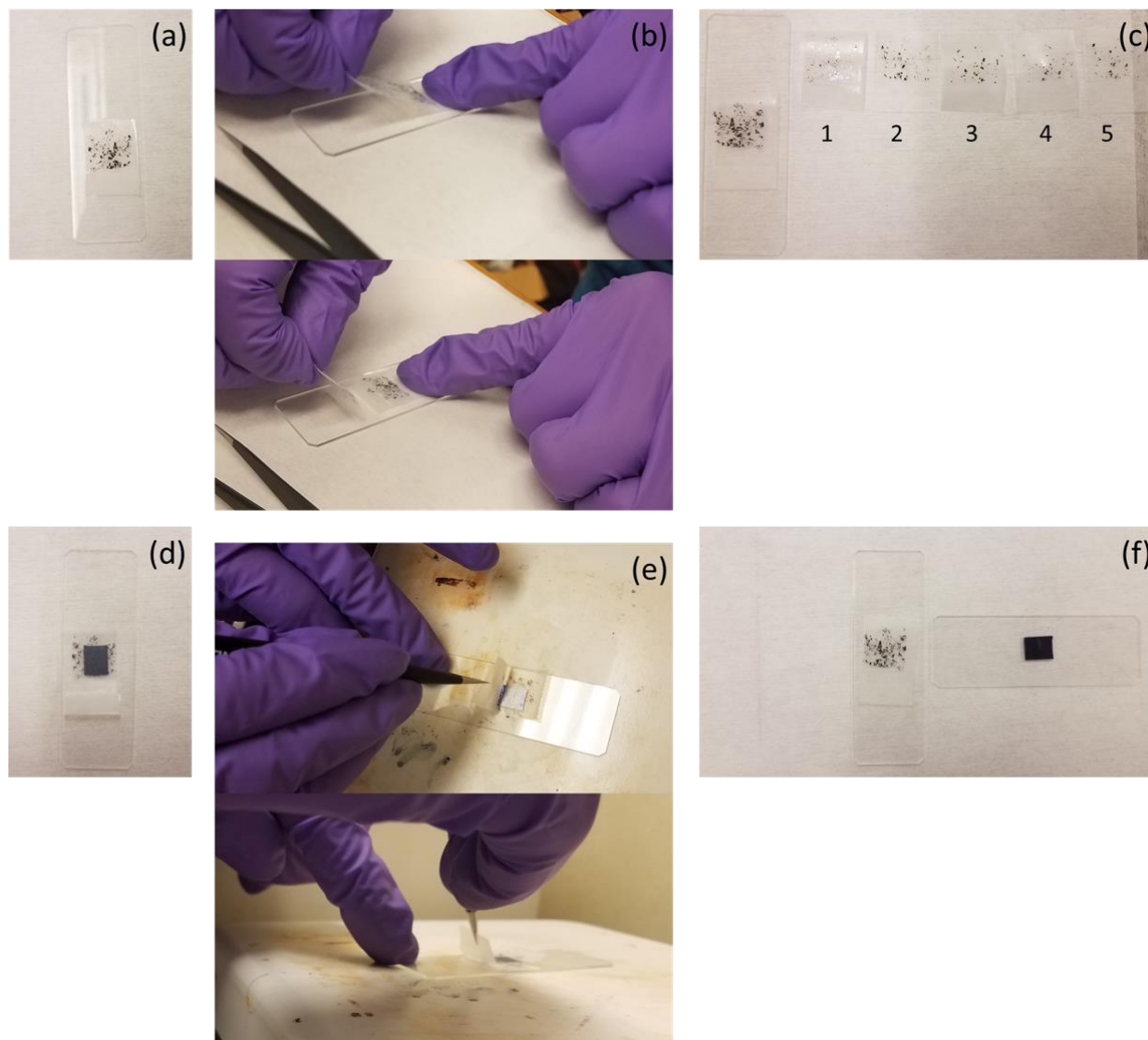


Fig. 2.3. Mechanical exfoliation of graphene. a) Mother tape with bulk graphite flakes distributed to cover a large area. b) Steps to peel the new tape from the mother tape. c) Mother tape with five peeled tapes. d) Transfer of mother tape to the target substrate. e) Removal of the mother tape from the substrate while on the hot plate. f) Mother tape for further transfers of graphene flakes.

The h-BN flakes are obtained using the same method. Fig. 2.4(a) shows the mother tape (from Nitto Denko Corp.) with several crystals of hBN [55]. The next step is the same as described above: use fresh tape, smooth the fresh tape onto the mother tape with a cotton swab, peel slowly, and repeat the procedure three to four times, as illustrated in Fig. 2.4(b). The goal is to obtain h-BN flakes with thicknesses of approximately 25 nm.

After repeated exfoliation cycles, the mother tape is adhered to a previously acid-cleaned Si/SiO₂ substrate. Afterward, the substrate is placed on the hot plate (see Fig. 2.4(c)), and the same process as described for graphene transfer onto the substrate is employed. The h-BN mother tape, as displayed in Fig. 2.4(d) is ready to use for further transfers.

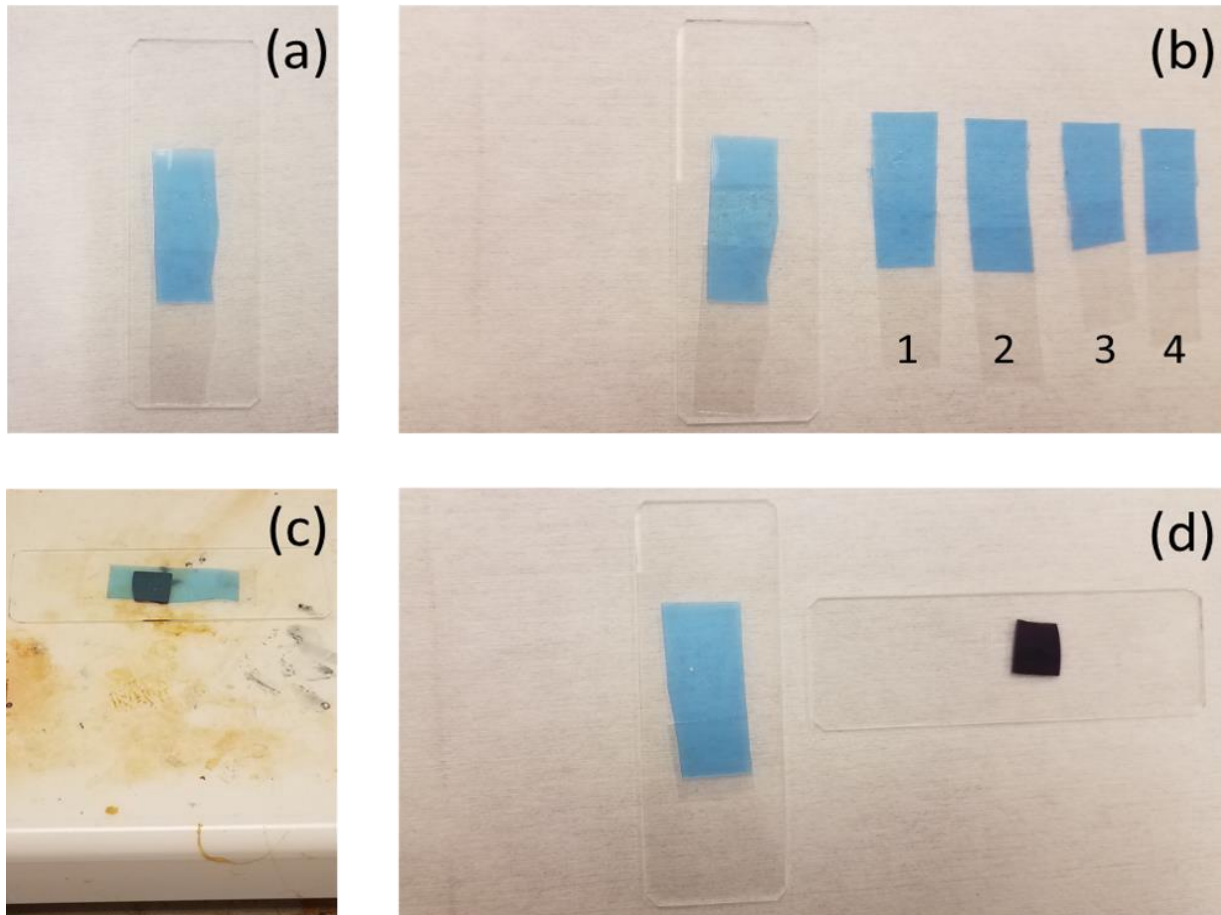


Fig. 2.4. Mechanical exfoliation of h-BN. a) Mother tape with h-BN crystals. b) Mother tape with four peeled tapes. c) Target substrate sitting on the hot plate prior to the final peeling. d) Mother tape ready for further h-BN transfers.

Material characterization

The transferred graphene layers are first optically inspected using a light microscope. The color contrast difference between the Si/SiO₂ substrate and the graphene flakes makes it easy to locate them. Fig 2.5(a) shows trilayer (TL) and monolayer (SL) graphene flakes; the latter has a size of $\sim 80\mu\text{m} \times 80\mu\text{m}$.

A Raman spectroscopy microscope system (Xplora, from Horiba) is employed to identify graphene monolayers [56]. The Raman spectrum in Fig. 2.5(b) (using a 532-nm excitation laser) exhibits two main peaks corresponding to G and 2D modes at 1580 cm^{-1} and 2690 cm^{-1} , respectively. As the number of graphene layers decreases, the Raman spectrum changes as follows: 1) for trilayers and thicker structures, the G peak intensity is higher than the 2D peak; 2) for a bilayer, both peaks have the same height, and 3) for a monolayer, the 2D peak is twice as high as the G peak. We use the intensity ratio of the 2D/G peaks to confirm the presence of graphene monolayers.

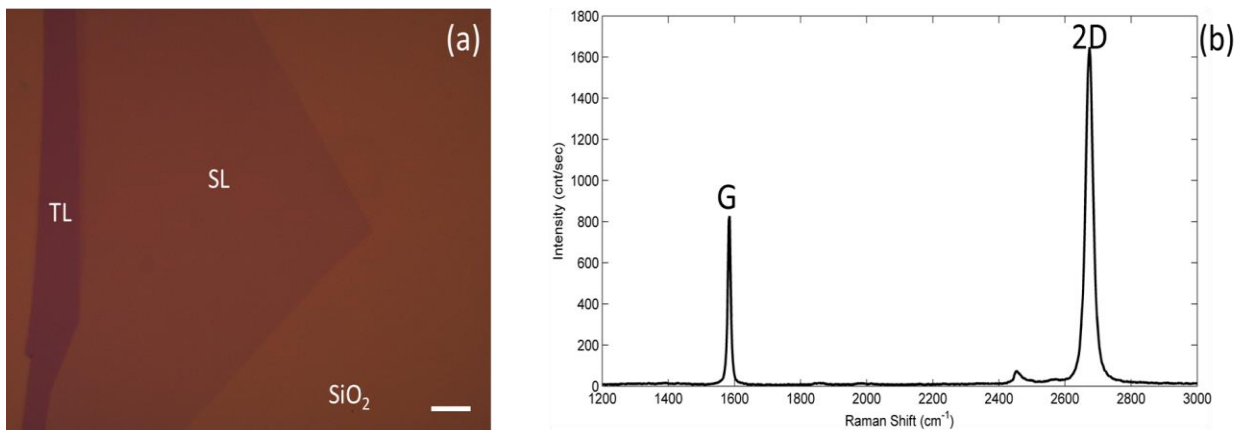


Fig. 2.5. Graphene characterization. (a) Optical image of a graphene monolayer (SL) and a trilayer (TL) on Si/SiO₂ substrate. The scale bar is $10\mu\text{m}$. (b) Raman spectrum of monolayer graphene showing the two main peaks at 1580 cm^{-1} (G) and 2690 cm^{-1} (2D).

The h-BN flakes are also identified with the optical microscope. Flakes fall in a thickness range of 10 nm to 60 nm and are identified by their optical contrast against the Si/SiO₂ substrate. Fig. 2.6(a) shows an h-BN flake of approximately $30\mu\text{m} \times 30\mu\text{m}$. The color variation within the flake represents variability in thickness across the sample. As the h-BN thickness is decreased, the color contrast resembles that of a few layers of graphene. Hence, the green region is thicker than the dark blue region.

The Raman spectrum of h-BN is obtained using the same equipment and conditions as described for graphene; in Fig. 2.6(b), the spectrum displays the characteristic peak of h-BN at 1366 cm^{-1} . The intensity in this Raman mode weakens and a shift from the primary peak position is observed as the number of layers decreases [57].

An atomic force microscopy (AFM) system (Ntegra, from NT-MDT) in the tapping mode [58] was utilized to image and measure the thickness of h-BN. A surface image of an h-BN flake is shown in Fig. 2.6(c). Line scans (1 - 4) are employed to determine the sample thickness. The topography profiles are given in Fig. 2.6 (d). This shows that the thickness of the green region in Fig. 2.6(a) is 30 nm, while that of the dark blue region is 8 nm. AFM surface scans enable one to selected h-BN flakes free of defects for the fabrication of sensor devices.

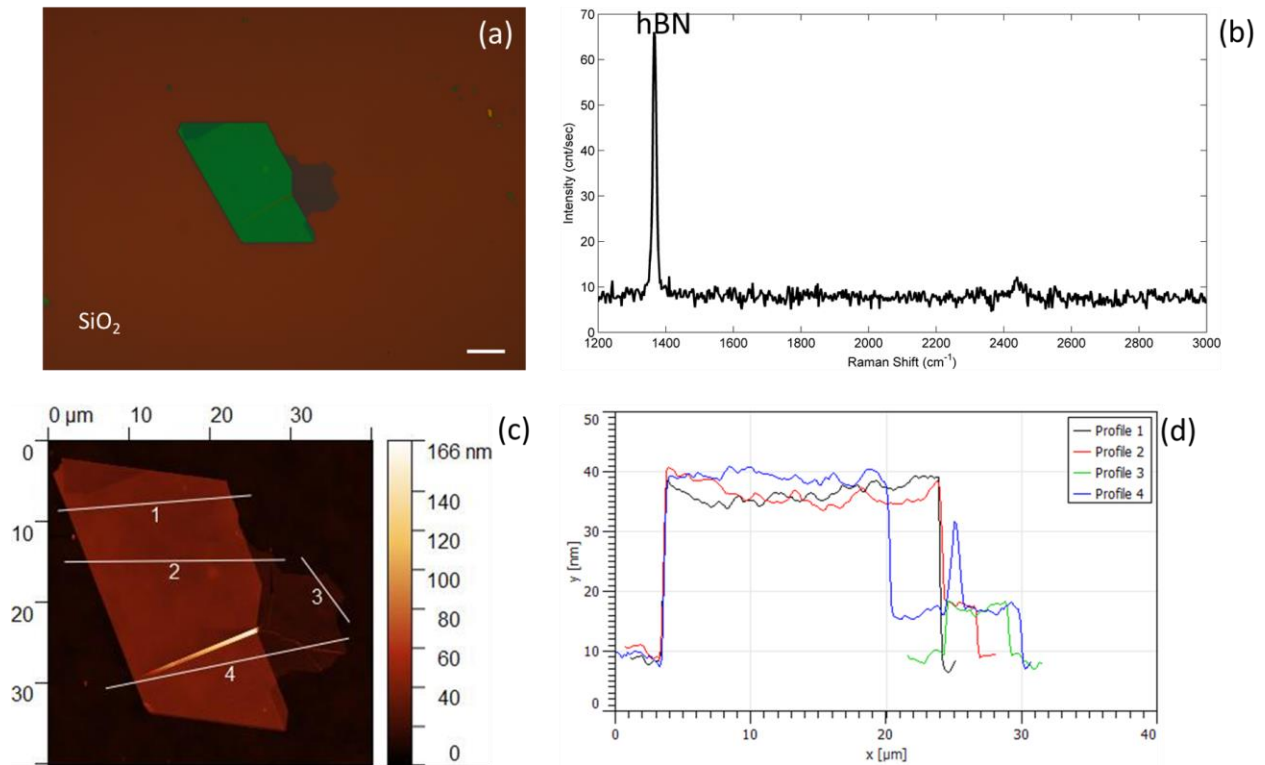


Fig. 2.6. h-BN characterization. (a) Optical microscope image of an h-BN flake. Scale bar 10 μm . (b) Raman spectrum of h-BN samples with its characteristic peak at 1366 cm^{-1} . (c) AFM surface image of h-BN depicting topography profiles. (d) h-BN flake thickness plots along the line profiles shown in (c).

2.2.2 Device fabrication of h-BN/graphene/h-BN trilayer stacks

Exfoliated graphene and h-BN layers are assembled together to form h-BN/graphene/h-BN trilayer stacks. Graphene is sandwiched between h-BN layers by the van der Waals method, wherein a polymer stamp is used to pick up the material sitting on top of the Si/SiO₂ substrates. The stamp preparation starts by placing polydimethylsiloxane (PDMS) on top of a glass slide. Then, a thin wrinkle- and bubble-free polycarbonate (PC) film is placed on top of the PDMS.

The heterostructure stack assembly is performed inside a glovebox (see Fig. 2.7) equipped with an optical microscope, a digital camera, a stage heater controller and a micromanipulator station. The latter has two micrometer stages, one with three axes (x, y, z) of motion and the second with three axes of motion and one of rotation (x, y, z, θ). The stamp and target substrate are placed on the three-axis stage (stamp holder) and the four-axis stage (sample holder), respectively.

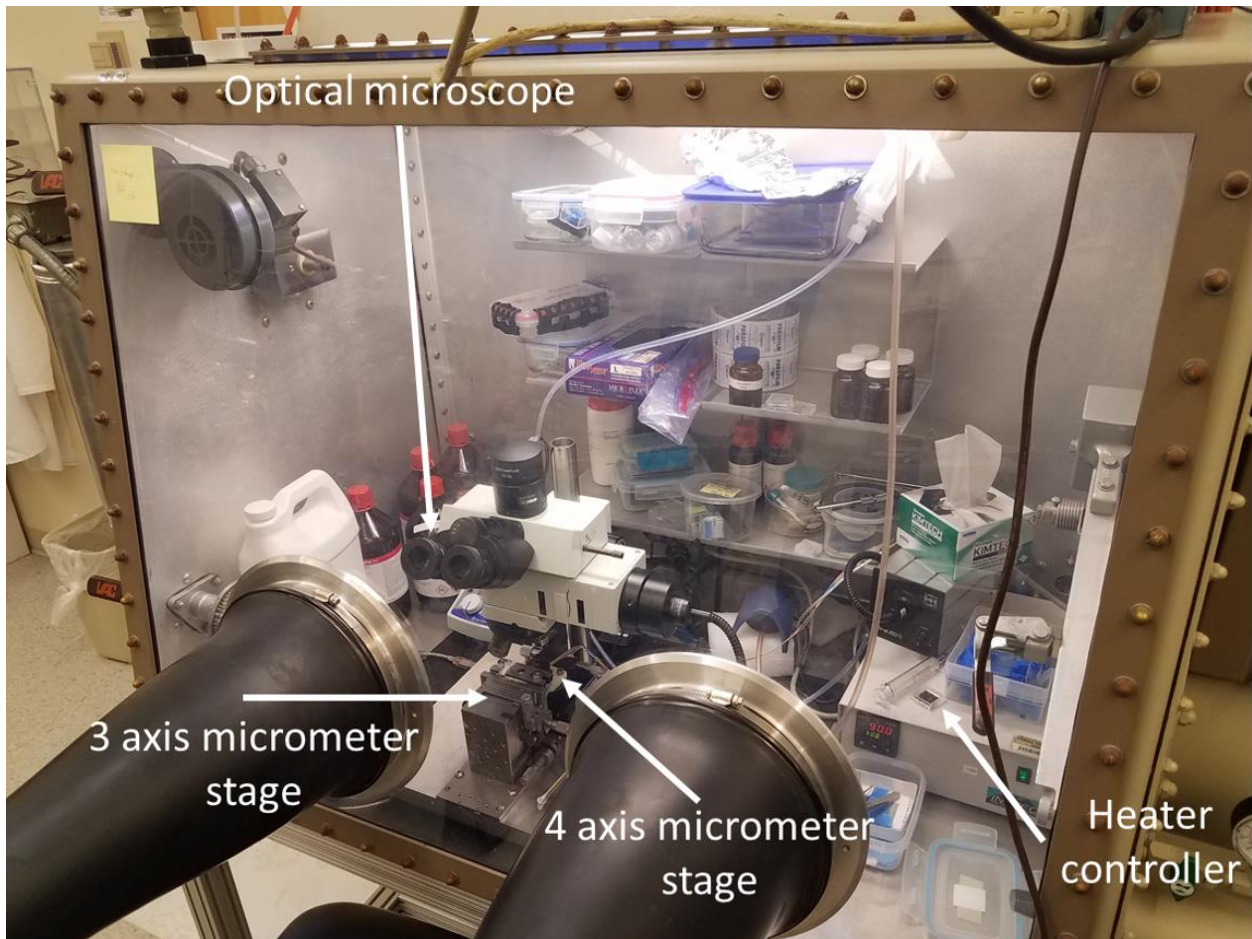


Fig. 2.7. Photograph of the micromanipulator station for heterostructure stacks assembly.

The trilayer-stack assembly procedure is as follows: the sample holder temperature is set at 40 °C, and the h-BN layer is first identified. Once it is localized, the stamp is lowered until the PC is very close to the h-BN flake. Next, the temperature is increased to 60 °C at a rate of 1 °C/min. This expands the PC and covers the h-BN flake, as illustrated in Fig. 2.8(a). As soon as the flake is completely covered, the temperature is brought back to 40 °C at a rate of 1 °C/min. While the temperature decreases, the PC contracts, peeling the h-BN flake from the substrate, as shown in Fig. 2.8(b). After the successful pickup of the h-BN flake, the stamp is raised to introduce the substrate that contains the graphene flake.

Once the graphene is located, the h-BN layer is positioned above the graphene monolayer, as shown in Fig. 2.8(c). The holder temperature is then increased from 40 °C to 60 °C at a rate of 0.1 °C/min, to expand the PC and make contact with the graphene flake. Fig. 2.8(d) shows the PC completely covering the area where graphene is located. Then, the temperature is brought back to 40 °C at 0.1 °C/min to perform the thermal peeling. The transfer of graphene by h-BN happens on account of the fact that the van der Waals interactions between h-BN and graphene are stronger than those between graphene and SiO₂. Fig. 2.8(e) shows the successful retrieval of graphene from the Si substrate.

The stamp, which now has the h-BN/G stack, is then aligned with the h-BN flake that completes the trilayer stack. Fig. 2.8(f) shows the PC as it begins to cover the substrate after the stamp is lowered. The same heating procedure described in the previous paragraph is employed to peel off the final h-BN layer. Once the bottom h-BN flake is wholly covered, the temperature is increased from 60 °C to 120 °C at a rate of 2 °C/min. This last step is employed to separate the PC from the PDMS and to affix the PC to the substrate. Fig. 2.8(h) shows the substrate entirely covered by the PC; a slight mechanical push is needed to achieve this. Next, the substrate with the h-BN/G/h-BN stack and covered with the PC is submerged in chloroform for 10 min. A final annealing cycle is performed in a tubular oven at 400 °C for 4 hrs. in a flowing Ar/H₂ atmosphere (200 sccm).

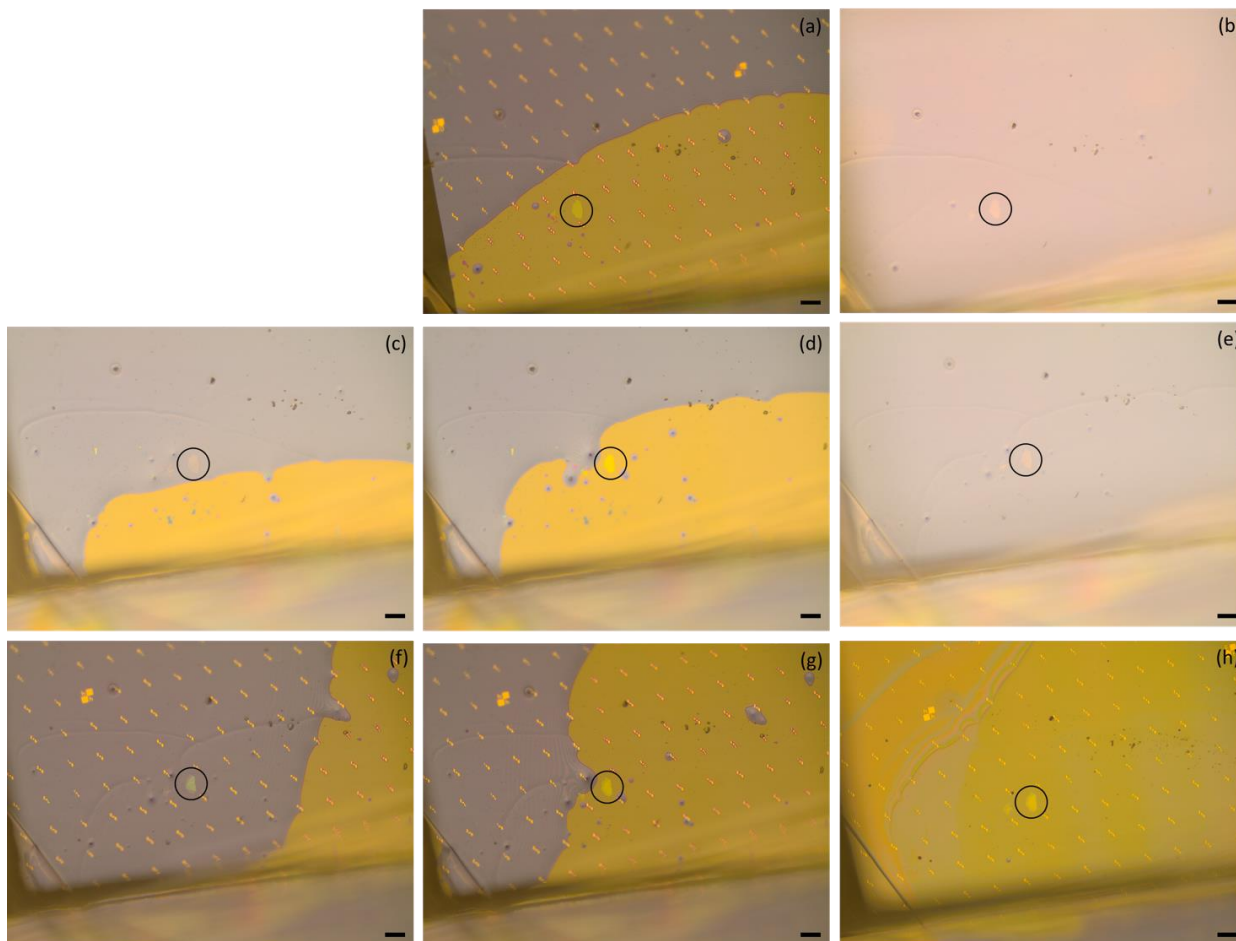


Fig. 2.8. Procedure to produce h-BN/graphene/h-BN trilayer structures. (a-b) h-BN top layer pickup by the polymeric stamp by the van der Waals method. (c-d) Graphene pickup by the stamp containing the h-BN cap flake. (f-h) Stamp containing h-BN/G dropped onto the h-BN bottom flake. The black circle shows the localization of the h-BN cap, graphene, and h-BN bottom. Scale bar 200 μm .

The stack is then inspected using an optical microscope; a corresponding image in Fig. 2.9(a) shows the graphene encapsulated between h-BN layers, as well as the presence of bubbles that remain after assembling the stack. To remove the bubbles, a second annealing cycle at 400 $^{\circ}\text{C}$ for 4 hrs. in a flowing (200 sccm) Ar/H₂ atmosphere was performed. Fig. 2.9(b) shows the results of the annealing, where some bubbles are observed to merge, in particular outside the graphene region. Further bubble removal is achieved by subjecting the stack to additional annealing cycles.

The effect of a third annealing cycle is displayed in Fig. 2.9(c), indicating that some bubbles still remain. A fourth annealing cycle at 500 $^{\circ}\text{C}$ for 4 hrs. in flowing Ar/H₂ (200 sccm) was next

conducted, and its effects are shown in Fig. 2.9(d). As expected, the region around the graphene shows fewer bubbles on account of enhanced bubble diffusion at higher temperatures. Therefore, a fifth annealing cycle was performed at 600 °C for 4 hrs. with the same gas flow conditions. Fig. 2.9(e) shows the stack after the fifth annealing. The image shows that within the graphene area, there is only one bubble; the rest are situated around the graphene perimeter. To identify a bubble-free area and to confirm that graphene was successfully encapsulated on hBN and was not damaged, Raman spectroscopy and AFM were employed.

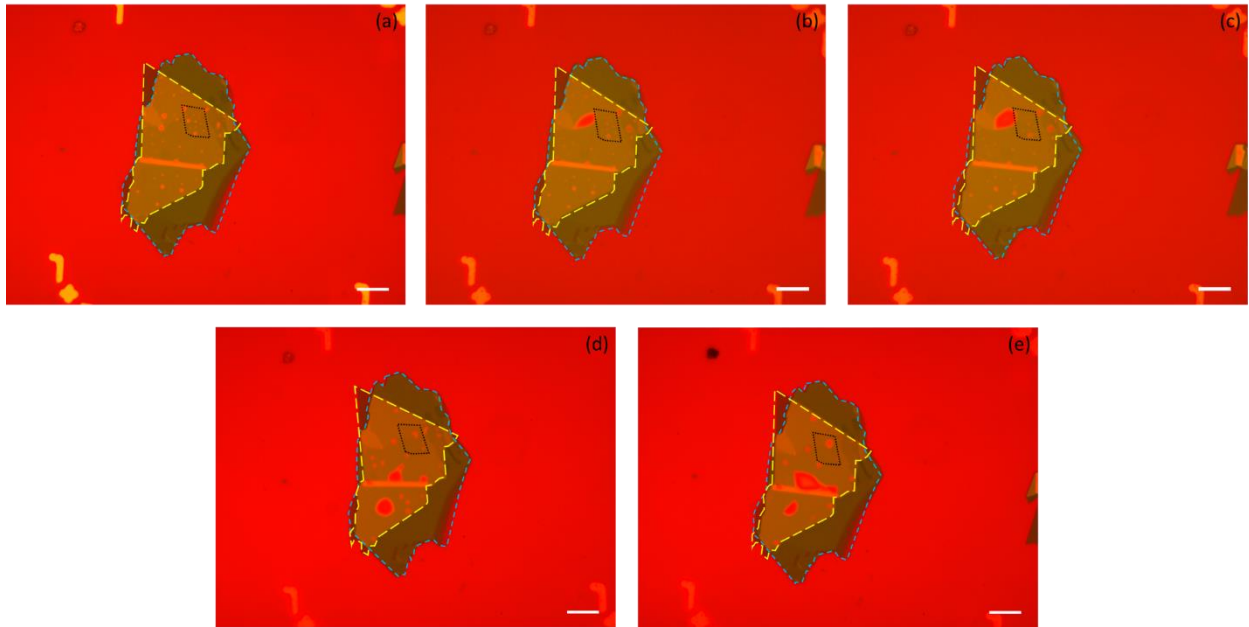


Fig. 2.9. Optical microscope images of the annealing treatment to remove bubbles within graphene's area. (a) Trilayer stack after assembly and after the first annealing process at 400 °C. (b) Second annealing at 400 °C. (c) Third annealing at 400 °C. (d) Fourth annealing at 500 °C. (e) Fifth annealing at 600 °C. Annealing cycle duration was 4 hrs. in a flowing Ar/H₂ atmosphere (200 sccm). h-BN bottom (blue dashed line), graphene (black dashed line), and hBN cap (yellow dashed line). Scale bar 10 μm.

Raman spectra and maps of the trilayer stacks are obtained using a Raman spectroscopy microscope system (inVia, from Renishaw®). The system has a map image acquisition mode that provides spectral collection while varying the sample x, y position. The spectral acquisition was performed in steps of 1 μm in raster mode. Fig. 2.10(b) displays a Raman spectrum showing the characteristic peak for h-BN positioned at 1366 cm⁻¹, as well as the graphene G and 2D peaks at 1580 cm⁻¹ and 2690 cm⁻¹, respectively.

The Raman map shows the location of the graphene monolayer (green) and the h-BN flakes (red). The corresponding AFM surface image is displayed in Fig. 2.10(c) showing the location of the remaining bubbles. Profilometry scans across different areas of the stack (Fig. 2.10(c)) were made to measure sample thickness. These are summarized in Fig. 2.10(d). The total stack height is ~ 40 nm, and the area free of bubbles is $\sim 7 \mu\text{m} \times 7 \mu\text{m}$.

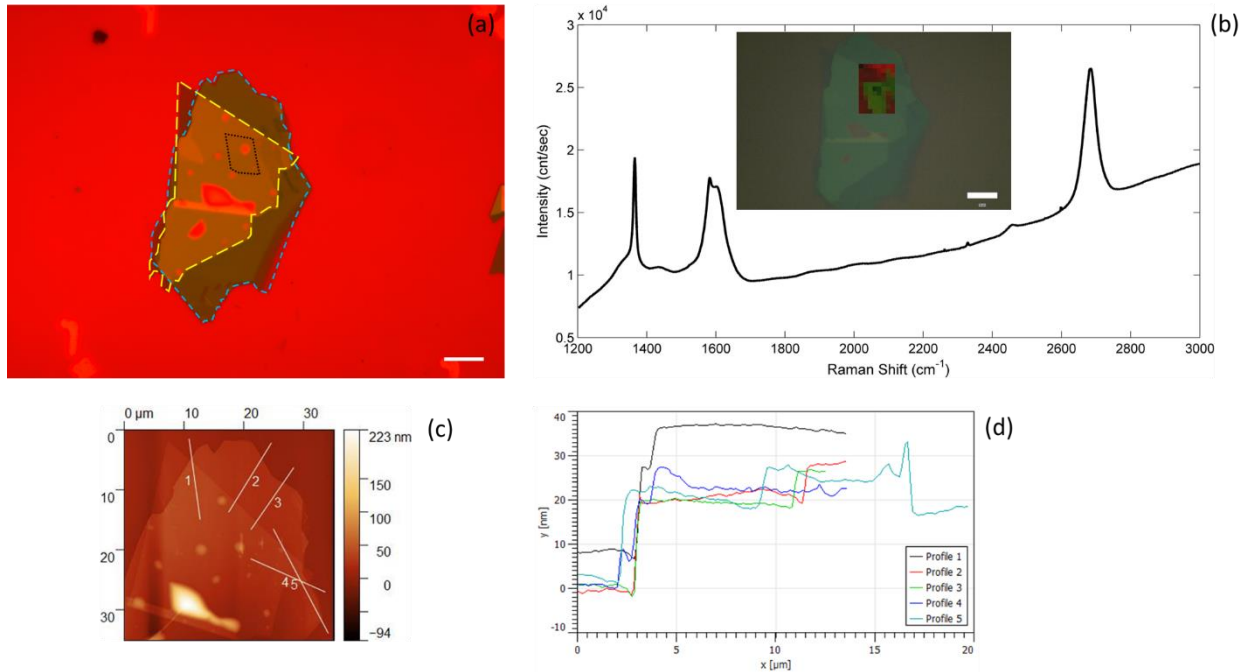


Fig. 2.10. Characterization of the h-BN/G/h-BN stack. (a) Optical microscopy image of the stack, h-BN bottom (blue dashed line), graphene (black dashed line), and h-BN top layer (yellow dashed color). The scale bar is $10 \mu\text{m}$. (b) Raman spectrum, showing the h-BN main peak at 1366 cm^{-1} and the graphene G and 2D main peaks at 1580 cm^{-1} and 2690 cm^{-1} , respectively. Inset in Fig. 2.10(b) displaying the Raman maps for monolayer graphene (green) and for the h-BN flakes (red), the scale bar is $10 \mu\text{m}$. (c) AFM surface image indicating the regions of the trilayer from which topography profiles were obtained. (d) Surface profiles showing the thickness of the stack across the profile lines indicated in Fig. 2.10(c).

Hall cross nanofabrication

The fabrication of a Hall cross starts by spin coating a negative photoresist (MAN 2403) onto the Si/SiO₂ (substrate)/h-BN/graphene/h-BN structures at 3000 rpm for 45 s and then baking it for 1 min at 90 °C. Fig. 2.11(a) shows an optical microscope image of the h-BN/G/h-BN stack covered by the photoresist. In the image, the black rectangle outlines the graphene monolayer. A smaller $5 \mu\text{m} \times 5 \mu\text{m}$ area free of bubbles is selected to fabricate the Hall cross.

Electron beam lithography (EBL) (eLiNE, from Raith Nanofabrication) was employed to pattern the MAN 2403 photoresist and define the profile of the Hall cross. Fig. 2.11(b) shows the device outline after developing the exposed photoresist with AZ 726 (a tetramethylammonium hydroxide (TMAH)-based developer) for 1 min and rinsing in DI water for 5 min. Next, the Hall cross is etched in a RIE system (E620, from Panasonic) using the following recipe. A gas mixture of Ar and SF₆ is used, with flow rates of 15 sccm and 25 sccm, respectively. At a power of 300 W inductively coupled RF plasma and 40 W capacitive bias. At a pressure of 50 mTorr (6.6 Pa), an etching time of 3 min + 30s is utilized to fully etch the structure.

The optical microscope image of Fig. 2.11(c) displays the etched Hall cross after the removal of the remaining MAN 2403 photoresist by employing acetone and isopropyl alcohol (IPA). From this image, it can be seen that the graphene edge is exposed. Next, the Hall cross is spin coated twice with PMMA for 45 s at 3000 rpm and baked for 2 min at 130 °C. Fig. 2.11(d) shows the optical image of the Hall cross covered with PMMA. Then, EBL was used to pattern the PMMA to define the shape of the Hall-cross metal contacts. Fig. 2.11(e) presents the metal-contact outline after development of the structure with IPA:DI water (3:1) for 1 min. The metal contacts were deposited in a Lesker electron beam evaporator and consist of a bilayer of Cr (40 nm) and Au (40 nm). The material that contacts the graphene edge first is Cr. This was selected because the Cr work function ($\Phi = 4.5$ eV [59]) is comparable to that of graphene ($\Phi \sim 4.6$ eV [60]–[62]) in comparison, for example, to that of Ti ($\Phi = 4.33$ eV [59]). Both Cr and Ti layers are used for adhesion promotion in the fabrication of metallic contacts.

The total thickness of the Cr/Au contact was selected to meet the recommended value of 80 nm for strong wire bonding. It is noted that given the project constraints this metal contact was not optimized to, for example, attain the lowest contact resistance by varying the total thickness or ratio of the Cr/Au bilayer or by examining adhesion-promoting materials other than Cr. Fig. 2.11(f) shows the final Hall-cross device after the residual metal lift-off.

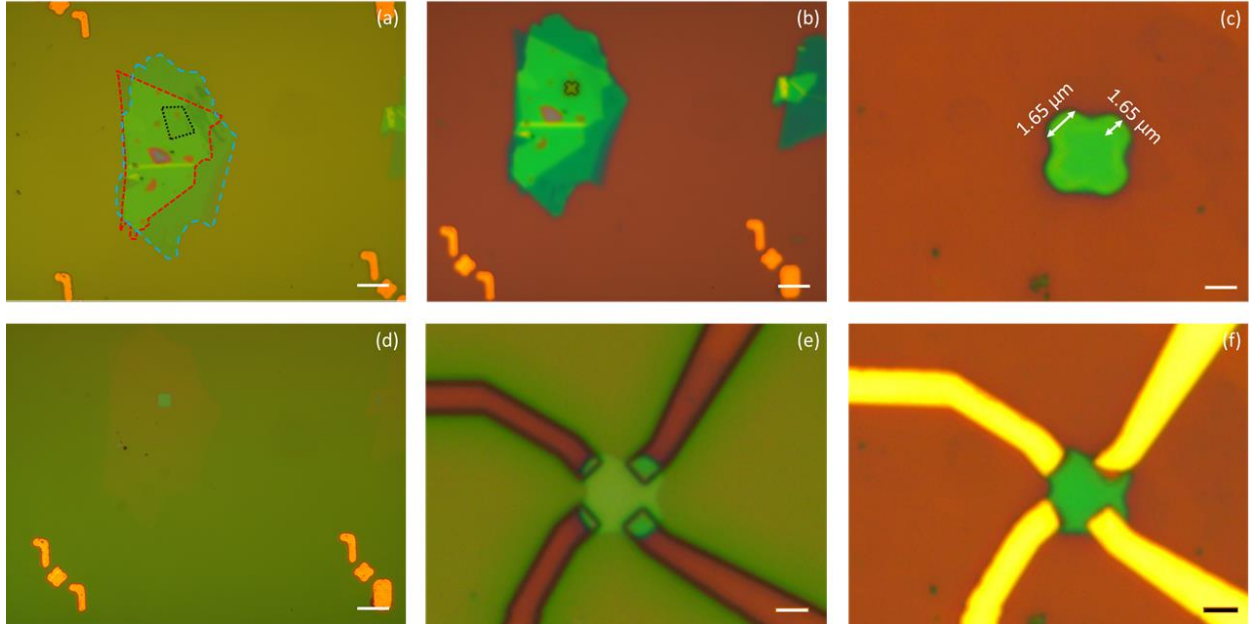


Fig. 2.11. Hall cross fabrication process. (a) Optical microscopy image of the stack covered with MAN4023. h-BN bottom (blue dashed line), graphene (black dashed line), and h-BN cap (red dashed color). (b) Hall cross patterning with e-beam lithography. (c) Hall cross etched exposing graphene edges after using RIE. (d) Optical microscope image of the Hall cross covered with PMMA. (e) PMMA patterning of the metal contacts using EBL. (f) Final Hall cross after metal deposition and lift-off. (a-f) Scale bar 10 μm .

EMR device nanofabrication

An alternative assembly and fabrication process of the trilayer stack based on an improved method reported in Reference [50] is presented in Appendix A. Also presented are characterization results for these heterostructure stacks, employing Raman spectroscopy and AFM techniques. The obtained h-BN/G/h-BN stack illustrated in Fig. A.2 shows a bubble-free area of $13\mu\text{m} \times 13\mu\text{m}$, which was employed to fabricate an EMR device. The nanofabrication process of the EMR devices is the same as that employed to fabricate the Hall cross. However, the metal contacts consist of a bilayer of Ti/Au (10 nm/60 nm) to investigate the impact of having a larger work-function difference between graphene and the adhesion layer. Fig. 2.12 shows the final EMR device after fabrication. The sensing area of $4.5\mu\text{m} \times 1.6\mu\text{m}$ is delineated by the white dashed rectangle. The electrical contact tabs are 500 nm wide.

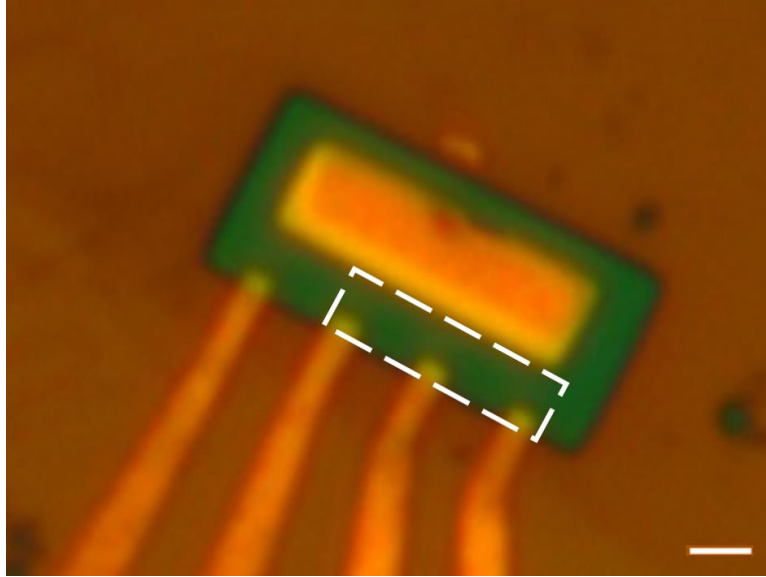


Fig. 2.12. Optical microscope image of the final EMR device with a metallic shunt after metal deposition and lift-off. Sensing area of $4.5 \mu\text{m} \times 1.6 \mu\text{m}$ (white dashed rectangle). The scale bar is $10\mu\text{m}$.

2.3 Discussion

The assembly of h-BN/graphene/h-BN trilayer structures requires bubble-free regions for device fabrication, as bubbles negatively impact transport properties [48], [63]–[68]. Several procedures to reduce defects in similar stacks have been reported by Pizzocchero et al. [68] and by Purdie et al. [50]. The latter utilizes mechanical pressure to obtain bubble-free regions of the same size as the exfoliated materials. These authors reported mobilities of $180,000 \text{ cm}^2/\text{Vs}$ at RT in Hall-bar devices having a channel width of $24 \mu\text{m}$.

The methodology presented in Appendix A for the fabrication of trilayer stacks provides bubble-free areas that are 26% larger than those produced by the procedure described above. Thus, employing said methodology should yield interfaces free of bubbles and contaminants and can potentially improve device performance, allowing higher sensitivity of graphene-based magnetometers at RT.

3. ELECTRIC AND MAGNETIC TRANSPORT CHARACTERIZATION OF GRAPHENE-BASED MAGNETOMETERS

The following chapter describes the electrical and magnetic characterization of the fabricated graphene-based magnetometers. The chapter is divided in two sections; the first presents characterization results for devices fabricated from CVD-grown graphene (Hall-bar and EMR devices). The goal was to investigate the EMR device response as a function of device dimensions and to compare the signal response to that of the Hall-bar devices. In addition, the need to protect the graphene layer from environmental contamination is discussed, as they dramatically change its intrinsic properties. The second section describes characterization results for devices fabricated from mechanical exfoliation of graphene (Hall-cross and EMR devices). The purpose was to demonstrate enhancement of the intrinsic properties of graphene-based magnetometers by encapsulating the graphene by h-BN layers. A comparison is also made between EMR and Hall-cross magnetoresistive sensors.

The characterization includes resistivity, magnetoresistance, and Hall voltage measurements, as well as signal-to-noise measurements to determine device voltage sensitivity (S_v), current sensitivity (S_I), and magnetic resolution (B_{min}). These parameters depend crucially on the carrier density (n_s) and carrier mobility (μ) of graphene as well as on the contact resistance at the graphene-metallic shunt and tab junctions.

3.1 CVD Graphene-Based Magnetometers

The Hall-bar and EMR devices fabricated on p-doped Si/SiO₂ substrates employing CVD graphene are illustrated in Fig. 3.1(a-c). The sensing area of the Hall bar is 1 mm × 0.5 mm and is marked in Fig. 3.1(a) by the white dashed rectangle. The larger EMR device (EMR1) has a sensing area of 2.2 mm × 1.1 mm and the small EMR device (EMR2) a corresponding one of 1.2 mm × 0.6 mm (see Fig. 3.1(b) and Fig. 3.1(c)). Note that the sensing area of the EMR devices reported in Reference [1] was at the micron scale.

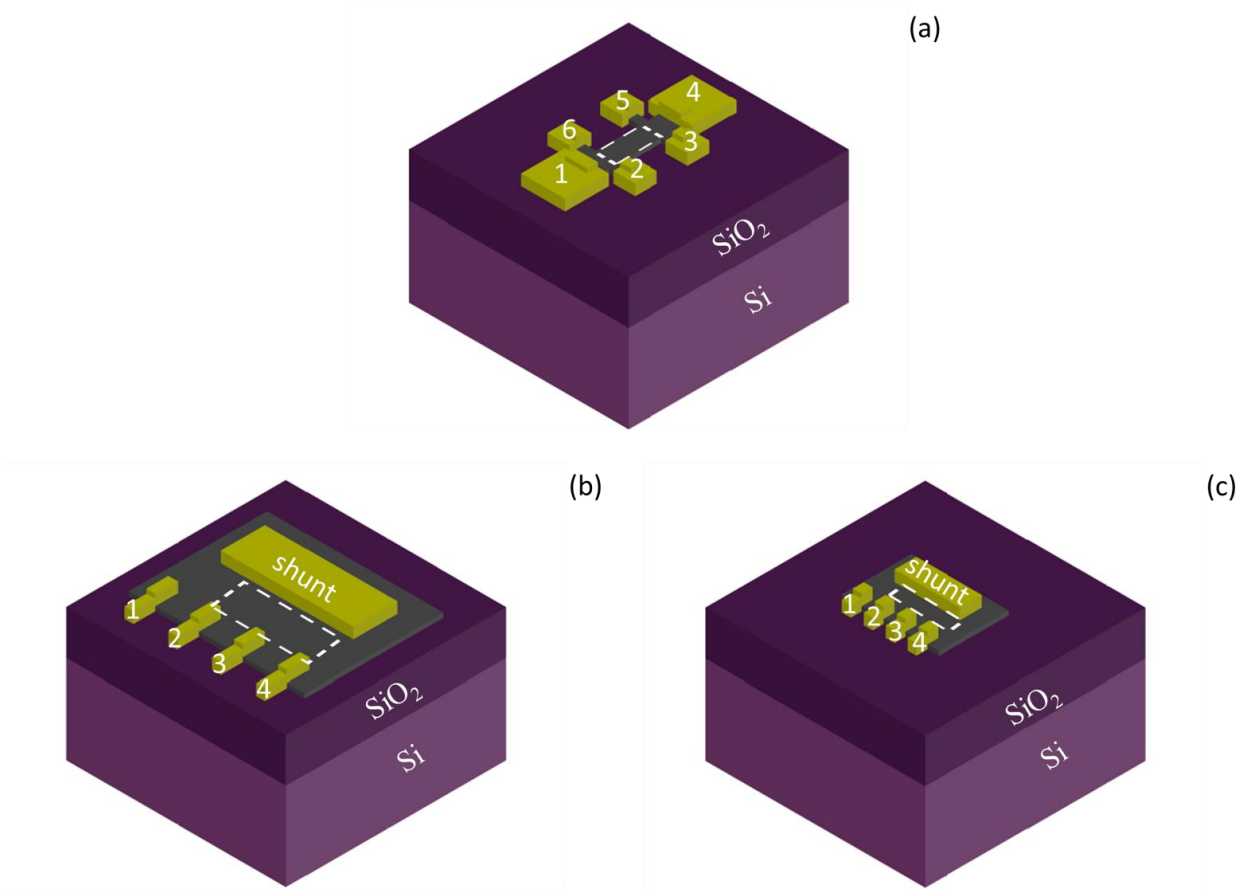


Fig. 3.1. Schematics of CVD graphene devices. (a) Hall bar with a sensing area of $1 \text{ mm} \times 0.5 \text{ mm}$. (b) EMR device with a sensing area of $2.2 \text{ mm} \times 1.1 \text{ mm}$. (c) EMR device with a sensing area of $1.2 \text{ mm} \times 0.6 \text{ mm}$. All devices were fabricated on Si/SiO₂ substrates. The graphene layer is depicted in grey, while the metal contacts are shown in yellow. The sensing area is delineated by the white dashed line. The EMR devices have a metallic shunt (Ti/Au (10 nm/60 nm)) within the graphene area. Labeled numbers as reference for electrical connections.

3.1.1 Electrical measurement definitions

Two-point resistance measurements were made with the following lead configuration:

$$R_{ij,kl} = \frac{V_i - V_j}{I_{kl}} \quad (3.1)$$

$V_i - V_j$ is the voltage difference, and the applied current (I_b) flows from tab k to tab l .

The total resistance (R) for the Hall bar is given by

$$R = \frac{(R_{23,14} + R_{65,14})}{2} \quad (3.2)$$

and the corresponding value for the EMR is

$$R = \frac{(R_{23,14} + R_{32,41})}{2} \quad (3.3)$$

The resistivity (ρ) is given by

$$\rho = R \frac{Wt}{L} \quad (3.4)$$

where W is the width and L the length of the sensing area, and t is the conducting-layer thickness.

From Equation (3.4) the sheet resistance (R_s) is given by

$$R_s = \frac{\rho}{t} \quad (3.5)$$

The contact resistance (ρ_s) between metal tabs, shunt, and graphene, as described earlier, is an important parameter that strongly influences device performance. The transfer-length method (TLM), consisting of an array of contacts with different spacing, is used to determine contact resistance. The measured resistance is plotted as a function of contact spacing; from it, ρ_s is derived [69] and given by the expression

$$\rho_s = R_c \cdot W \quad (3.6)$$

Hall measurements are made by applying an injection current (I_b) in the presence of an applied magnetic field (B) perpendicular to the plane of the sample. From the Hall voltage (V_H) measurement, the charge carrier density (n_s) can be determined from the expression

$$n_s = \frac{I_b B}{q |V_H|} \quad (3.7)$$

where q is the electron charge, and from the definition of n_s , the carrier mobility (μ) can be estimated from

$$\mu = \frac{1}{q n_s R_s} \quad (3.8)$$

Hall measurements are employed to determine the magnetometer sensitivity. The sensor can be operated in two modes, current and voltage, by applying either a constant current or a constant voltage, respectively. The following relations give the current sensitivity (S_I) and the voltage sensitivity (S_V):

$$S_I = \frac{1}{I_b} \left| \frac{V_H}{B} \right| \quad (3.9)$$

$$S_V = \frac{1}{V_b} \left| \frac{V_H}{B} \right| \quad (3.10)$$

where the Hall voltage (V_H) is given by

$$V_H = V_H(B) - V_H(0) \quad (3.11)$$

$V_H(B)$ and $V_H(0)$ are the voltages measured in the presence and absence of an applied magnetic field, respectively.

The current sensitivity and voltage sensitivity are crucially dependent on the carrier density and carrier mobility [70]. This dependency is given by

$$S_I = \frac{1}{qn_s} \quad (3.12)$$

$$S_v = \mu \frac{W}{L} \quad (3.13)$$

where W and L are the width and length of the sensing area.

In addition, another critical device performance parameter is the magnetic resolution (B_{min}), which indicates the smallest magnetic field the sensor can detect. This requires noise power spectrum density (PSD) and Hall voltage (V_H) measurements. Depending on the device operation mode, B_{min} is given by equation (3.14) or (3.15) for voltage and current mode device operation, respectively.

$$B_{min} = \frac{\sqrt{PSD}}{(S_v \cdot V_b)} \quad (3.14)$$

$$B_{min} = \frac{\sqrt{PSD}}{(S_I \cdot I_b)}. \quad (3.15)$$

The dependence of the sensitivity on carrier density (n_s) and mobility (μ) implies that the magnetic resolution at a fixed frequency depends on these parameters. B_{min} improves by decreasing n_s and increasing μ .

Finally, the EMR effect is given by

$$EMR = \frac{R(B) - R(0)}{R_{kl}(0)}, \quad (3.16)$$

where $R(B)$ and $R(0)$, are the measured four-terminal resistances in the presence and absence of an applied magnetic field. $R_{kl}(0)$ is the measured two-terminal resistance through the current leads in the absence of an applied magnetic field.

3.1.2 Measurements under vacuum conditions

Transport measurements were performed using a physical property measurement system (PPMS) (DynaCool™, from Quantum Design). All measurements were performed in vacuum (0.1mTorr) over the temperature range 1.8K to 400K and magnetic fields ranging -9 to +9 T. The maximum field sweeping rate is 20 mT/s, the minimum 10 μ T/s. The electrical transport option

(ETO) hardware (D605), utilizing a digital lock-in amplifier and input current amplitudes ranging from 10 nA to 100 mA at frequencies from 0.1 to 200 Hz, was employed. The ETO sensitivity is ~ 10 n Ω RMS. The device resistance can be measured using either two- or four-terminal contact configurations. In two-terminal contact measurements, the total resistance is obtained; this comprises the wiring resistance (R_w), the contact resistance (p_s), and the sheet resistance (R_s). In four-terminal resistance measurement, the sheet resistance (R_s) is measured directly. The Hall-effect measurements, as described in section 3.1.1, are used to determine the carrier density and mobility, and the device sensitivity.

Resistivity measurements

Measurements were performed using two-terminal contact configurations with an injection current of 10 μ A. Fig. 3.2 shows the resistance as a function of contact spacing for EMR1 (black circle marker) and EMR2 devices (blue square marker). From the linear fit, the resistance (at zero spacing) is given as twice the TLM contact resistance (R_c), and the values in the figure are indicated by the black (EMR1) and blue (EMR2) arrows [69]. Using R_c in Equation (3.6), the contact resistance for the EMR1 device and the EMR2 device is calculated to be 29 k Ω μ m and 35 k Ω μ m, respectively.

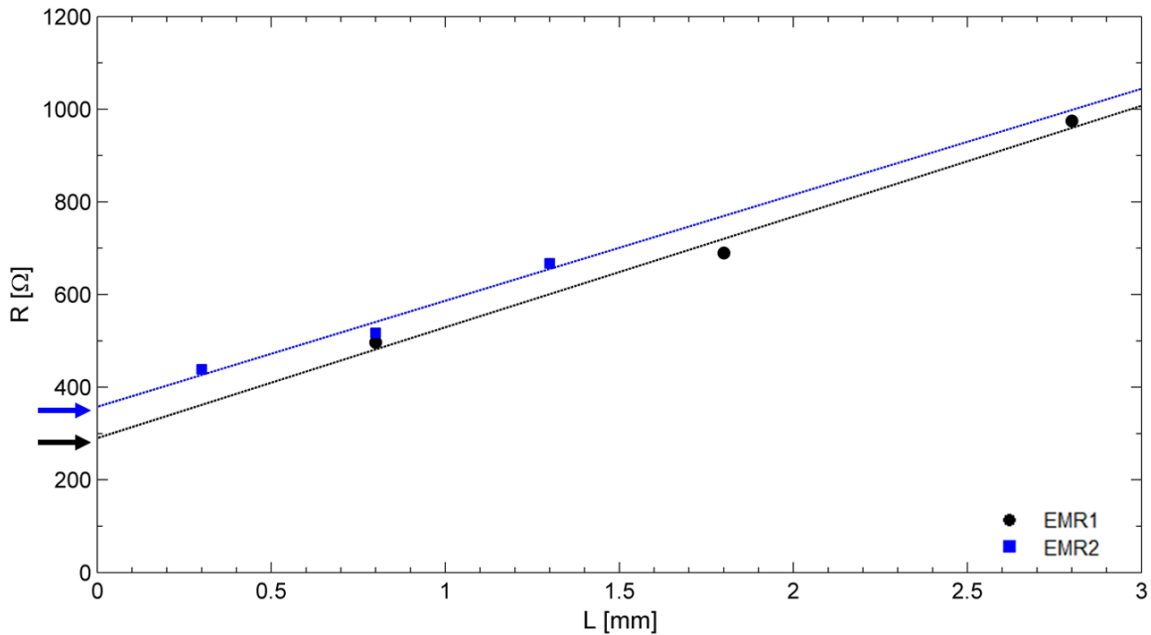


Fig. 3.2. Two-terminal resistance as a function of spacing and twice the TLM contact resistance (R_c) for the EMR1 device (black) and the EMR2 device (blue). Arrows indicated R_c .

The four-terminal configuration was employed to obtain the total device resistance, estimated using Equations (3.2) and (3.3); the injected current for these measurements was also 10 μ A. The subscript number given in the equations identifies the tabs through which current was injected and the corresponding tabs used for voltage measurements. Resistivity (p) and sheet resistance (R_s) for the devices are calculated using Equations (3.4) and (3.5) and displayed in Table 3.1. The values obtained show that the Hall bar is more resistive by 31.3% and 43.7% than the EMR1 and EMR2 devices, respectively. This is attributed to the metallic shunt in the EMR devices, since charge carriers are attracted to the metallic region, making a smaller total device resistance.

Table 3.1 Resistivity measurement results of CVD-grown graphene-based devices employing the PPMS at RT under vacuum conditions.

	R (Ω)	p (Ωm)	R_s ($\Omega/sq.$)	p_s ($k\Omega \mu m$)
Hall bar	1,320	2.24×10^{-7}	660	*
EMR1	690	1.17×10^{-7}	345	29
EMR2	517	8.79×10^{-8}	259	35

EMR1, device with sensing area of 2.2 mm \times 1.1 mm.

EMR2, device with sensing area of 1.2 mm \times 0.6 mm.

* measurements were not performed.

Hall-effect measurements

Longitudinal voltage (V_{xx}) measurements obtained from adjacent voltage tabs located on both sides of the Hall bar are presented in Fig. 3.3(a) and Fig. 3.3(b); a parabolic dependence of V_{xx} versus applied magnetic field is observed. In the presence of the magnetic field, the Lorentz force deflects charge current, and both polarities exhibit an increment of the voltage because the measured voltage is parallel to the flow of the current. Comparison of these results reveals a difference of 7.8% in V_{xx} in Fig. 3.3(b) for measurements at the highest values of the applied magnetic field. An offset of 190 μ V at zero applied magnetic fields is also evident between these two measurement configurations. These differences are attributed to the grain boundary scattering in the CVD graphene channel.

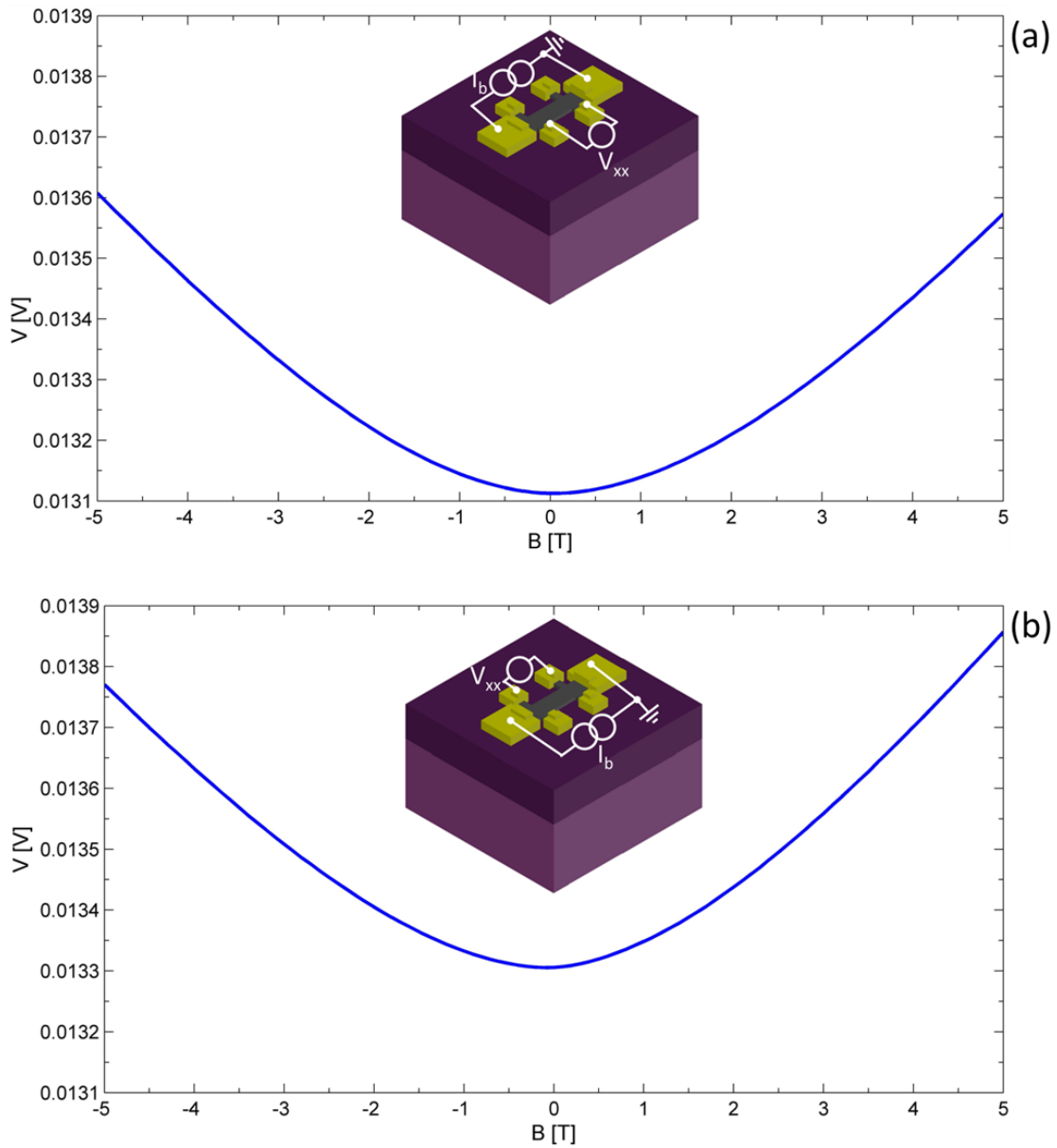


Fig. 3.3. Magnetic response of the Hall bar longitudinal voltage (V_{xx}) as a function of the magnetic field for (a) bottom and (b) upper adjacent voltage tabs. The input current was $10 \mu\text{A}$ and magnetic field sweep was ± 5 T. Inset shows the electrical connections configuration.

The Hall voltage (V_{xy}) measurements from tabs along the transverse direction (xy) of the Hall bar are presented in Fig. 3.4(a) and 3.4(b). As expected, a linear response of V_{xy} versus magnetic field is observed, and the sign of the slope of the response indicates that the charge carriers are p-type.

The carrier density (n_s) is determined from Equation (3.7) and from the slope value, whereas the carrier mobility (μ) is estimated using Equation (3.8) and the calculated values of R_s and n_s (see Table 3.1) These parameters are utilized together with the relevant equations previously given to derive current (S_I) and voltage (S_V) sensitivities. The values obtained are displayed in Table 3.2, which shows a comparison with the extracted EMR device values.

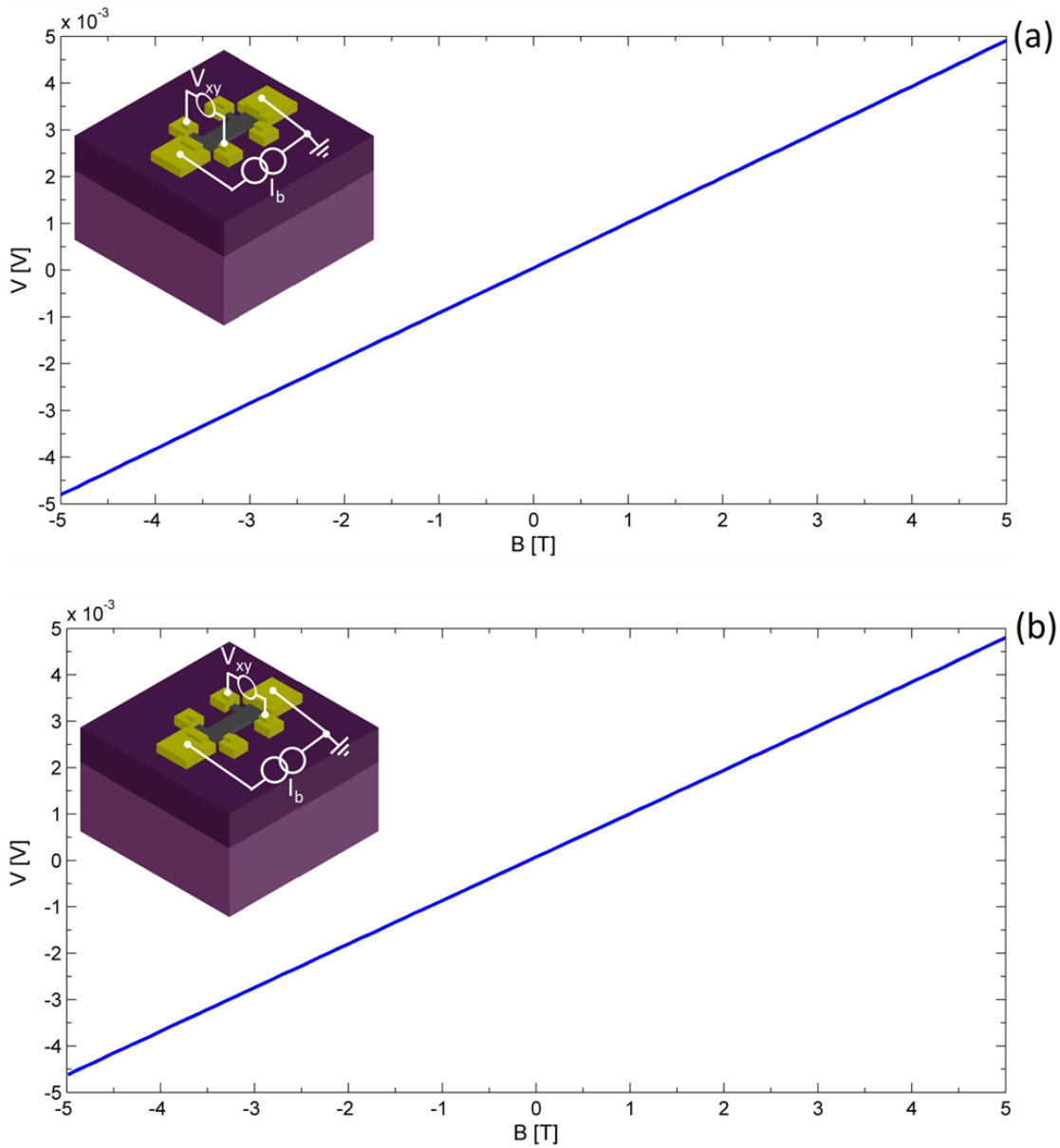


Fig. 3.4. Magnetic response of the Hall bar Hall voltage (V_{xy}) as a function of the magnetic field for (a) first and (b) second bridge voltage tabs. The input current was $10 \mu\text{A}$ and magnetic field sweep was ± 5 T. Inset shows the electrical connections configuration.

EMR measurements

The EMR measurements were conducted with bias currents of $10\ \mu\text{A}$, $150\ \mu\text{A}$, and $500\ \mu\text{A}$ and sweeping the magnetic field from $-5\ \text{T}$ to $5\ \text{T}$ in steps of $0.1\ \text{T}$ at RT. The EMR1 voltage difference (V_{diff}) for different bias currents (see Fig. 3.5(a)) increases proportionally with the value of the injected current. Similar behavior is exhibited in the EMR2 voltage curves versus magnetic field shown in Fig. 3.5(b).

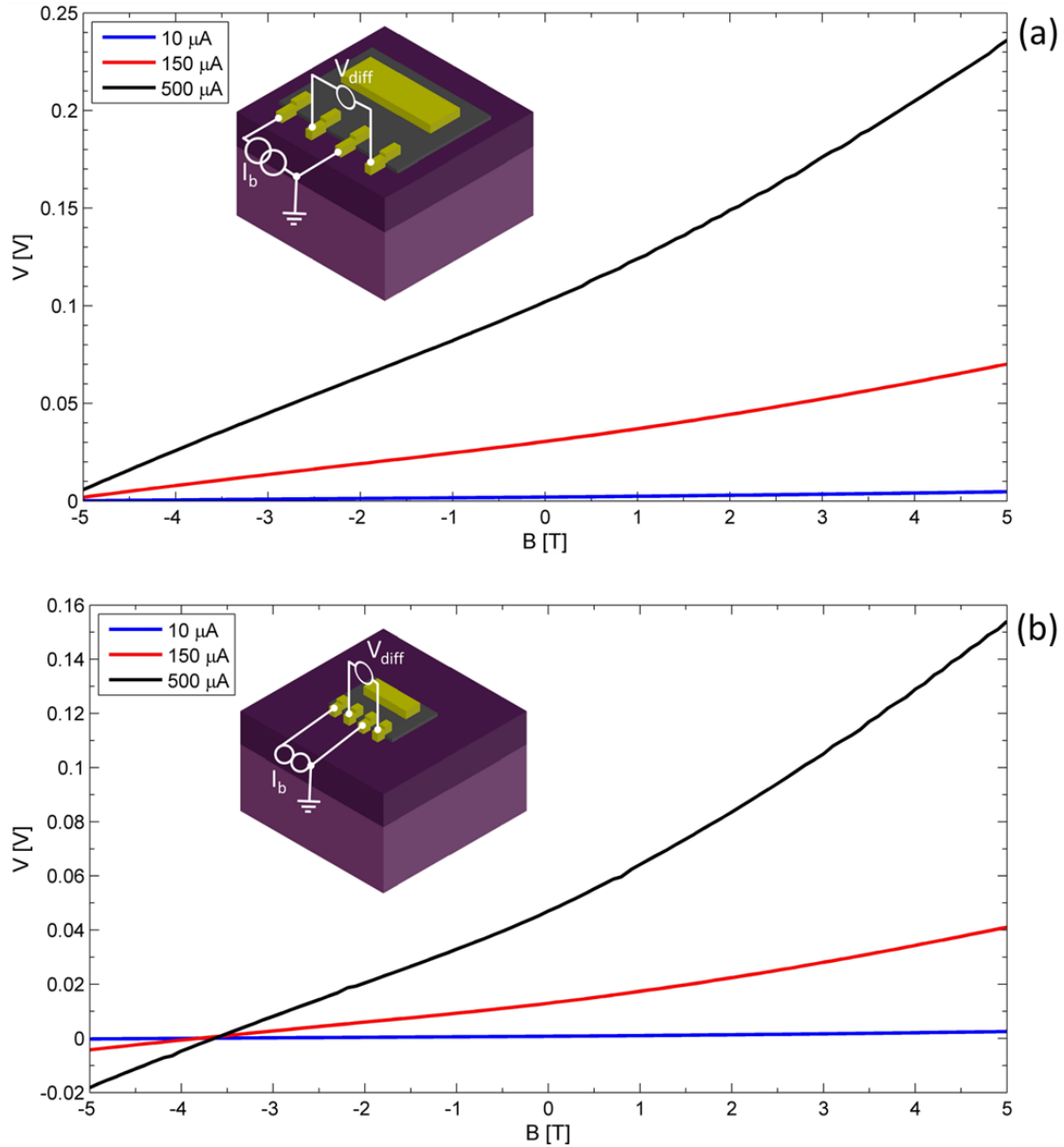


Fig. 3.5. Magnetic response of the (a) EMR1 device and (b) EMR2 device. V_{diff} as a function of applied magnetic field and input current. Inset show the electrical connections configuration.

A comparison between these devices shows that the EMR1 $\Delta V/\Delta B$ is higher compared to that of the EMR2 since its sensing area is larger by a factor of 3. The sign of the slope of the voltage curves for both devices indicates p-type charge carriers. The EMR-device carrier density (n_s), mobility (μ), current (S_I), and voltage (S_V) sensitivities are calculated as described previously for the Hall-bar device. Furthermore, the EMR effect is estimated using Equation (3.16) and the results from Fig. 3.5(a-b).

The magnetic response values of the Hall-bar and EMR devices are summarized in Table 3.2. The table compares the intrinsic properties n_s and μ as well as the sensitivities, S_I and S_V , and shows the magneto-resistive enhancement in the EMR devices. Measurements derived from the Hall bar are employed to determine accurately n_s and μ of materials for the CVD-graphene layers. In comparison, the estimated parameter values reported for the EMR devices are an approximation, as they can be expected to be influenced by the shunt and by geometrical effects, as there are two materials involved, the graphene sheet and the metal used for the metallic shunt.

The parameters provided in the table show that n_s for the Hall bar is one order of magnitude smaller compared to EMR1 and EMR2. The difference can be attributed to the difference in magnetoresistance response. The value of the slope response for an injection current of 10 μA in the Hall bar is 969 $\mu\text{V/T}$, while for the EMR1 and the EMR2 at the same current is 441 $\mu\text{V/T}$ and 259 $\mu\text{V/T}$, respectively. This shows that the Hall bar $\Delta V/\Delta B$ is higher by factors of 2 and 3 than for the EMR1 and EMR2 devices, respectively. Interestingly, the mobility values between these devices are not significantly different on account of differences in R_s . Table 3.1 shows that R_s is smaller for the EMR devices than for the Hall bar because of the metallic shunt. The higher n_s but smaller R_s in the case of the EMR devices, or vice versa for the case of the Hall bar, compensate for variations in μ (see Equation (3.8)) reflecting the small difference of mobility values reported.

The current and voltage sensitivities of the Hall bar are higher than those of the EMR devices. This can be understood from examining Equations (3.12) and (3.13): S_I increases as n_s decreases, and S_V increases as μ increases. The table also indicates that S_I and S_V are independent of the value of the injected current, whereas for EMR2 a strong dependence is noted. As a result, with increasing injection current, n_s decreases, whereas μ , S_I , and S_V increase.

Another observation is that the current sensitivity of the EMR devices maximizes for positive values of the applied magnetic field, as the charge carriers travel longer current paths thereby resulting in a higher $\Delta V/\Delta B$. In the presence of negative applied magnetic fields, the charge carriers travel shorter paths, giving a smaller $\Delta V/\Delta B$. The same magnetic-field dependence is observed for the voltage sensitivity.

Table 3.2. Magnetic response summary results for CVD graphene-based magnetometers at RT under vacuum conditions.

	I_b (μA)	n_s (cm^{-2})	μ (cm^2/Vs)	S_I (V/AT)		S_v (V/VT)		EMR (%)	
				-5 T	5 T	-5 T	5 T	-5 T	5 T
Hall bar	10	6.54×10^{12}	1,440	96	98	0.073	0.075	-	-
EMR1	10	1.41×10^{13}	1,278	37	54	0.054	0.078	27	39
	150	1.42×10^{13}	1,276	38	52	0.055	0.076	27	38
	500	1.40×10^{13}	1,290	38	53	0.055	0.077	27	38
EMR2	10	2.41×10^{13}	1,002	20	35	0.038	0.067	19	33
	150	2.15×10^{13}	1,121	22	37	0.044	0.072	22	36
	500	1.88×10^{13}	1,284	26	42	0.050	0.082	25	41

EMR1, device with sensing area of $2.2 \text{ mm} \times 1.1 \text{ mm}$.

EMR2, device with sensing area of $1.2 \text{ mm} \times 0.6 \text{ mm}$.

3.1.3 Effect of environmental exposure on CVD graphene-based magnetometers

Exposure of uncapped graphene devices to ambient conditions is known to degrade their intrinsic properties [72]. Therefore, we investigated the effect of prolonged ambient exposure on our devices after storage in the lab environment for 24 months.

Measurements were performed using the PPMS with the ETO module. The resistivity measurements using the two-terminal configuration are shown in Appendix B, Fig. B.1. From the plots, p_s for EMR1 and EMR2 is determined to be $120 \text{ k}\Omega \mu\text{m}$ and $160 \text{ k}\Omega \mu\text{m}$, respectively. These values show an increment of 61.1% for the EMR1 and of 63.5% for the EMR2. Resistivity (p) and sheet resistance (R_s) were also obtained using the four-terminal configuration. Measurements are given in Table 3.3 and were performed using an injection current of $10 \mu\text{A}$.

Table 3.3. Summary of resistivity measurements of EMR devices after 24 months of environmental exposure at RT.

	R (Ω)	p (Ωm)	R_s ($\Omega/sq.$)	p_s ($k\Omega \mu m$)
EMR1	1,830	3.11×10^{-7}	915	120
EMR2	1,850	3.14×10^{-7}	925	160

EMR1, device with sensing area of $2.2 \text{ mm} \times 1.1 \text{ mm}$.

EMR2, device with sensing area of $1.2 \text{ mm} \times 0.6 \text{ mm}$.

The EMR measurements at RT were performed using a four-terminal configuration with an injected current of $150 \mu\text{A}$ and a magnetic field sweep of from -5 to $+5$ T. The EMR1 and EMR2 V_{diff} responses as a function of the magnetic field are shown in Fig. 3.6(a) and Fig. 3.6(b), respectively. We note that their $\Delta V/\Delta B$ response is not very different (17 mV/T and 16 mV/T for EMR1 and EMR2 respectively). A summary of n_s , μ , S_I , S_V , and the EMR effect are tabulated and compared to non-aged samples in Table 3.4.

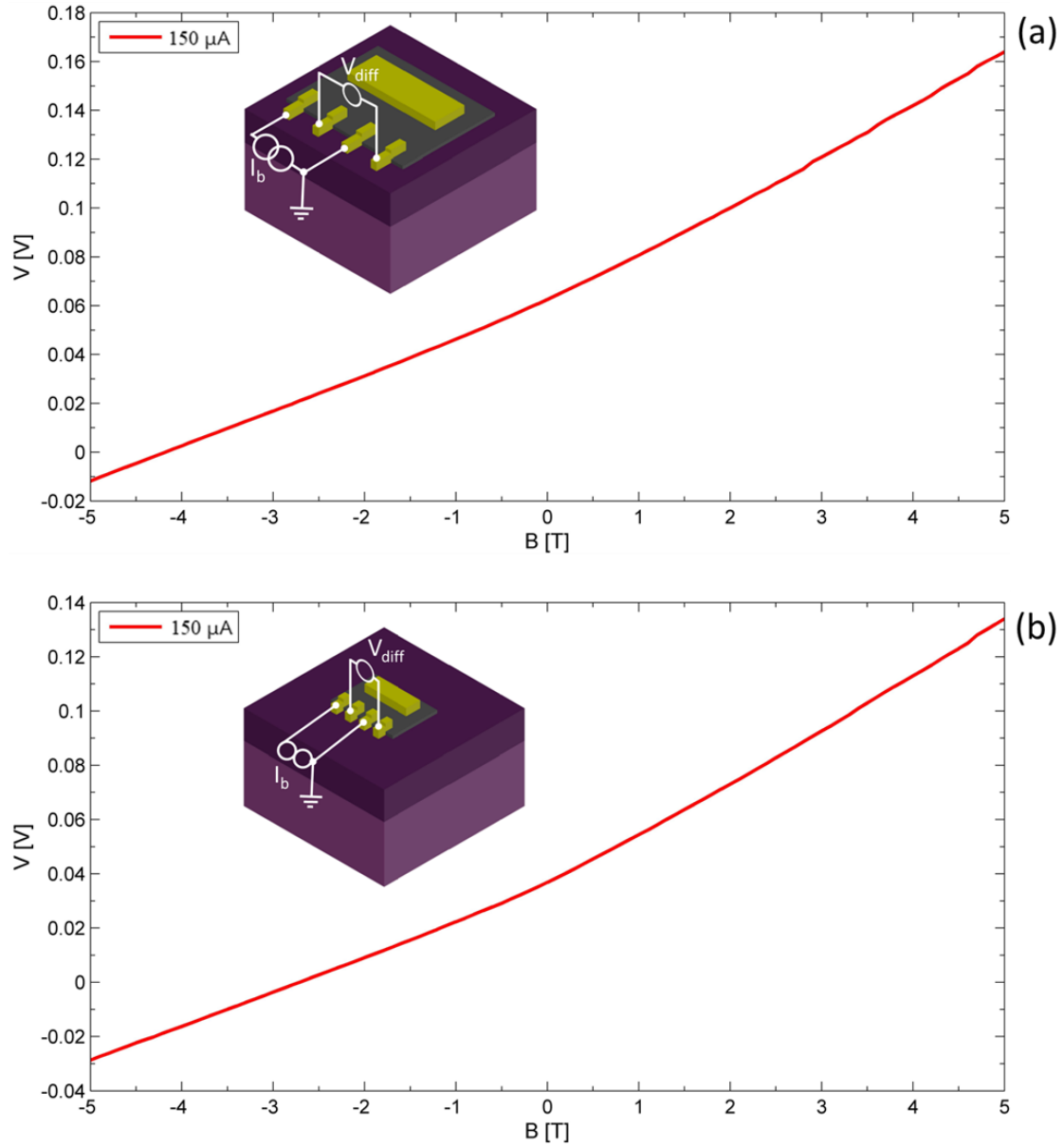


Fig. 3.6. Magnetic response of (a) EMR1 device and (b) EMR2 device voltage as a function of the magnetic field after aging time. Applied current, $150 \mu A$, and magnetic field, $\pm 5 T$. The inset shows the electrical connections configuration.

3.1.4 Discussion of CVD graphene-based magnetometers

A summary of measurements for the CVD-graphene magnetometers is given in Table 3.4. The table compares the device reported in Reference [1] with the CVD devices. The performance of our devices, we note, is limited by the fact that they were fabricated without the ability to supply gate voltage (V_g), which as reported in ref. [1] dramatically increments device performance and provides response tunability. Application of gate bias voltage changes the energy location of the Fermi level in graphene towards the conduction or valence band, depending on the polarity of gate voltages. Consequently, the resistivity of graphene varies with carrier concentration, and the maximum value attainable corresponds to the device run at the charge-neutral Dirac point (CNP). Our inability to perform measurements under gate bias stems from the fact that the substrates employed to fabricate our devices had oxide layers on either side of the Si substrate ($\text{SiO}_2/\text{Si}/\text{SiO}_2$), precluding the formation of electrical contacts on either side of the graphene device. Therefore, we compare results of ref. [1] only at $V_g = 0$ V; The contact resistance (p_s) of EMR0 is five and four orders of magnitude smaller compared to that of EMR1 and EMR2, respectively. The difference is attributed to the size of the contact area between graphene and the metal as well as to contact-material properties. The contact area of the EMR0 is $100 \text{ nm} \times 200 \text{ nm}$, while for the EMR1 and EMR2 they are $200 \text{ }\mu\text{m} \times 500 \text{ }\mu\text{m}$ and $200 \text{ }\mu\text{m} \times 250 \text{ }\mu\text{m}$, respectively. The material employed as an adhesion promoter between graphene and Au in the EMR0 device is Ta, which has a work function of $\Phi = 4.25 \text{ eV}$ [59], whereas the Ti layer employed in our devices has a work function of $\Phi = 4.33 \text{ eV}$ [59]. A significant work function difference between the adhesive layer and graphene has been reported to reduce p_s owing to graphene doping [74]. The possibility exists that differences in microstructure between Ti and Ta may result in higher grain-boundary scattering, formation of secondary oxide phases that can severely hinder transport. This must be investigated in future studies. Finally, we note that the metal contacts of EMR0 are Ta/Au (2.5 nm/20 nm), whereas for our CVD graphene magnetometers are Ti/Au (5 nm/90 nm). The adhesion-promoter layer and the Au thickness can be expected to influence the Au microstructure and impact p_s .

We note also the effect of exposure to ambient air on p_s , which increased by one order of magnitude for EMR2 and by a factor of six for the EMR1. Reactions of ambient oxygen and water with the metal contacts and interfaces can be expected to have a more deleterious effect on the smaller devices, as the oxidized volumes for the same diffusion rates are larger. Similarly,

chemisorption of oxygen by the unprotected graphene layer can be expected to negatively impact mobility and change carrier density, leading to pronounced p-doping, as reported in [75].

The carrier density (n_s) of the EMR0 is three times and one order of magnitude smaller than the n_s for the CVD Hall bar and EMR devices, respectively. This implies that the $\Delta V/\Delta B$ of EMR0 is higher compared to the aforementioned devices, and thus its current sensitivity (S_I) surpasses that of our magnetometers. After aging, an interesting effect is observed in EMR1 and EMR2: the carrier density, n_s , decreases by one order of magnitude. This decrement is attributed to the p-doping induced by absorption of oxygen on the graphene surface as mentioned above. A slight shift of the CNP voltage changes the sheet resistance, resulting in a higher $\Delta V/\Delta B$, thus in S_I enhancement for both EMR devices.

Mobility and S_V reported for EMR1 and EMR2 devices before and after aging are similar, as are those for the EMR enhancements. The EMR enhancement for EMR0 is smaller, as it was measured at a lower applied field (1.6 T rather vs 5 T).

The mobility in CVD-graphene magnetometers is limited by grain-boundary scattering in polycrystalline graphene and by the mechanisms described in section 1.7. As mentioned previously, using h-BN [77] as an interlayer between graphene and the substrate enhances mobility and carrier density. Additionally, capping graphene to protect it from environmental conditions is expected to improve the performance parameters. Finally, the use of gate voltage bias is needed to optimize mobility and the carrier density. As an example, the EMR0 maximum sensitivity is 250 V/AT at a gate voltage of 5 V.

Table 3.4. Comparison between CVD-graphene magnetometers and an EMR device reported in the literature. The measurements were done under vacuum conditions at RT.

	P_s (Ωm^2)	n_s (cm^{-2})	μ (cm^2/Vs)	B (T)	I_b (μA)	S_I (V/AT) $V_g=0$ V	S_v (V/VT) $V_g=0$ V	EMR (%) $V_g=0$ V
After fabrication								
EMR0	3×10^{-10}	2×10^{12}	1,000 – 5,000	± 1.6	150	175	-	4.37
EMR1	1.5×10^{-5}	1.41×10^{13}	1,278	± 5	10	54	0.078	39
		1.42×10^{13}	1,276		150	52	0.076	38
		1.40×10^{13}	1,290		500	54	0.077	38
EMR2	8.9×10^{-6}	2.41×10^{13}	1,002	± 5	10	35	0.067	33
		2.15×10^{13}	1,121		150	37	0.072	36
		1.88×10^{13}	1,284		500	42	0.082	41
Hall bar	-	6.54×10^{12}	1,440	± 5	10	98	0.075	-
After 24 months of aging								
EMR1	6.0×10^{-5}	5.38×10^{12}	1,266	± 5	150	135	0.074	37
EMR2	4.0×10^{-5}	5.81×10^{12}	1,160	± 5	150	129	0.069	34

EMR0, device reported by Pisana et al. [1]

EMR1, device with sensing area of $2.2 \text{ mm} \times 1.1 \text{ mm}$

EMR2, device with sensing area of $1.2 \text{ mm} \times 0.6 \text{ mm}$

3.2 Mechanical Exfoliated Graphene-Based Magnetometers

The Hall-cross and EMR devices fabricated from exfoliated graphene and h-BN trilayer stacks are illustrated in Fig. 3.7(a-b). The contact label numbers are used to describe how current injection and voltage measurements are performed. We are interested in comparing these two device architectures to quantify the sensitivity gains attained on account of geometrical effects in the case of the EMR devices. These devices were fabricated on substrates (p-doped Si) that permitted gate bias voltage applications.

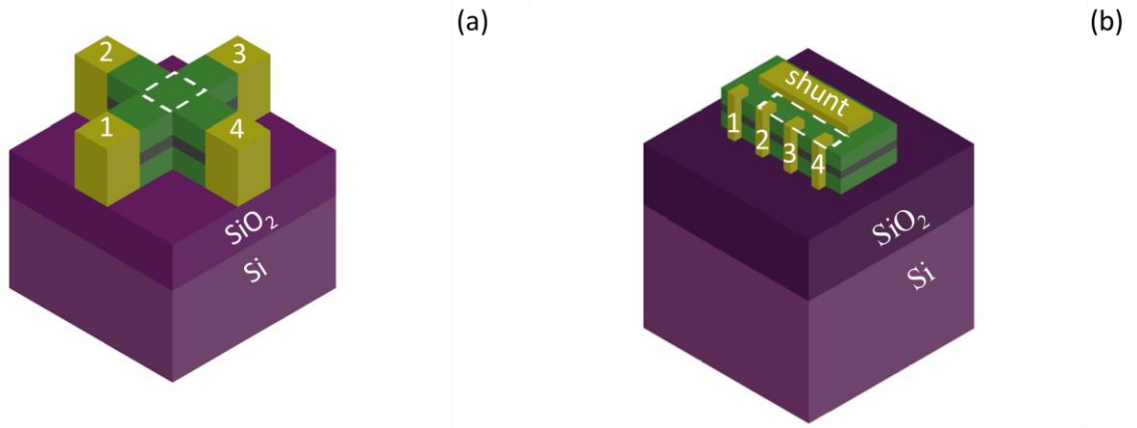


Fig. 3.7. Devices fabricated using h-BN/graphene/h-BN trilayers. (a) Hall cross device, sensing area of $1.65 \mu\text{m} \times 1.65 \mu\text{m}$. (b) EMR device schematic with sensing area of $4.5 \mu\text{m} \times 1.6 \mu\text{m}$. The color reference is graphene (grey), h-BN (green), and the metal contacts (yellow). Label numbers are reference for describing the electrical connections during device measurements.

3.2.1 Experimental definition

The Van der Pauw technique is used to determine the resistivity of uniform devices [71]. From resistivity measurements, the associated resistances ($R_{longitudinal}$ and $R_{transversal}$) can be estimated from

$$R_{longitudinal} = \frac{(R_{43,12} + R_{12,43})}{2}, \quad (3.17)$$

$$R_{transversal} = \frac{(R_{23,14} + R_{14,23})}{2}. \quad (3.18)$$

Using Equations (3.17) and (3.18), one can obtain the total resistance R , given by

$$R = \frac{(R_{longitudinal} + R_{transversal})}{2}. \quad (3.19)$$

3.2.2 Measurements under vacuum conditions

The Hall-cross devices were characterized employing the PPMS together with a 16-pin custom probe sample holder. A lock-in amplifier (SR830, from Stanford Research) was used to apply AC currents and to measure resistivity, Hall effect, and noise. For the last, an oscilloscope (MSO-X 3014T, from Keysight Technologies) was used with the probe connected in parallel to the lock-in amplifier differential input.

Resistivity measurements

The resistivity measurements were performed employing the two-terminal contact configuration and applying a sine-wave current (AC) of 1 μA at 7.7 Hz. The data from Fig. B.2 (Appendix B) are used to determine the contact resistance (p_s). Using the four-terminal contact configuration measurement and Equations (3.17) and (3.18), $R_{\text{longitudinal}}$ and $R_{\text{transversal}}$ are calculated, respectively. The subscript numbers displayed in the equations indicate the tabs where current is injected, and the voltage measured. Then, using the calculated resistance and Equation (3.19), the Hall-cross device total resistance (R) is inferred. This enables us to calculate the resistivity (p) and sheet resistance (R_s). Table 3.5 summarizes these measurements.

Table 3.5. Resistivity measurements for Hall-cross device fabricated from h-BN/graphene/h-BN trilayer structures

$R_{\text{longitudinal}} (\Omega)$	$R_{\text{transversal}} (\Omega)$	$R (\Omega)$	$p (\Omega m)$	$R_s (\Omega/\text{sq.})$	$p_s (k\Omega \mu\text{m})$
271	360	315	1.07×10^{-7}	315	2.78

Hall-effect measurements

The Hall-effect measurements were performed by applying an AC current of 1 μA at 7.7 Hz, while sweeping the external magnetic field from -50 mT to 50 mT in steps of 1 mT, as well as from -5,000 mT to 5,000 mT in 100 mT steps; both measurements were made without gate voltage. The magnetic response of the Hall cross at RT is displayed in Fig. 3.8(a-b). The voltage vs. magnetic field response Fig. 3.8(a) shows a linear, non-hysteretic response. The charge carrier type is positive, as inferred from the sign of the slope. For the case of the response when the magnetic field is swept $\pm 5,000$ mT, the voltage response exhibit saturation for fields higher than $\pm 1,500$ mT, and hysteresis behavior occurs, as seen in Fig. 3.8(b). It is noted that the maximum voltage value measured at -5,000 mT is 28% smaller than that measured at 5,000 mT. The total voltage changes at 50 mT and 5,000 mT are 249 μV and 13.5 mV, respectively. The Hall-cross device carrier density (n_s), mobility (μ), current (S_I), and voltage (S_V) sensitivities are calculated as described in section 3.1.2 and presented in Table 3.6.

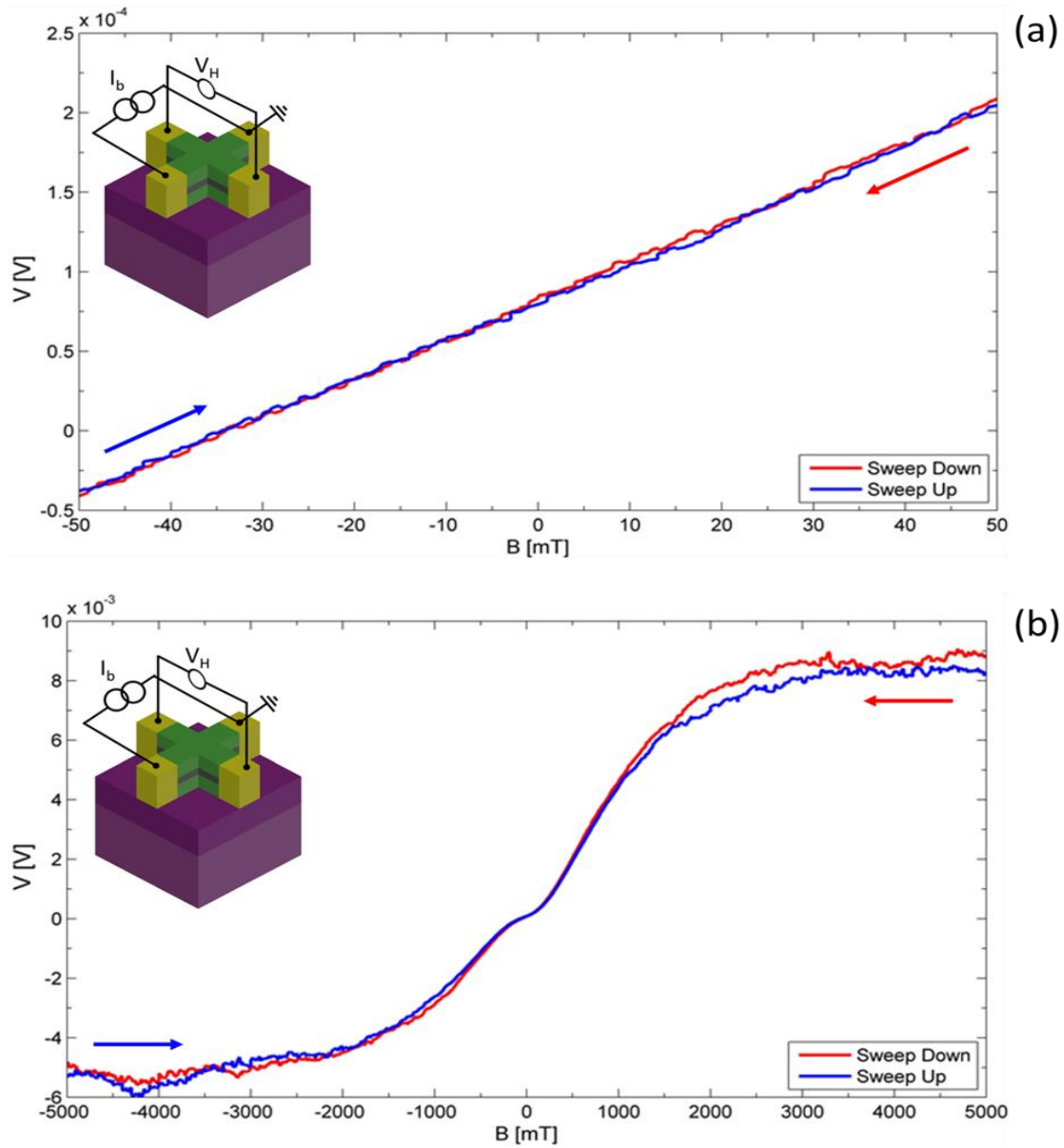


Fig. 3.8. Voltage response at RT of the Hall-cross device as a function of applied magnetic field at (a) ± 50 mT and (b) ± 5000 mT. Measurements conducted injected an AC current of $1 \mu\text{A}$ and without V_g . Arrows indicate the direction of the magnetic field sweep. Insets show the tabs configuration used for the measurements.

Noise measurements

The noise measurements were also performed by applying an AC current of $1\ \mu\text{A}$ at $7.7\ \text{Hz}$, in the absence of a magnetic field and without gate voltage. The Hall-cross device noise response is shown in Fig. 3.9(a-b). From the oscilloscope, 10-s windows were recorded using a time window of 1-s at 6.25-kHz sample frequency (f_s). Using the oscilloscope's fast Fourier transform (FFT) and a Hanning-window function, the time domain is converted to the frequency domain (10 Hz to 3 kHz window).

Further analysis of the FFT signal using Matlab[®] was made to obtain the *PSD*. The plotted *PSD* as a function of frequency (f) shows $1/f$ noise dependency whose magnitude decreases by three orders of magnitude from 10 Hz to 3 kHz, as shown in Fig. 3.9(b). The $1/f$ noise is dominant at frequencies below 100 kHz, and its spectrum reaches a noise floor equal to Johnson-noise level at the cutoff frequency. It originates from fluctuations of charge carriers due to trapping and de-trapping from the charge traps or fluctuations in the charge mobility [72]. Johnson noise is dominant at high frequencies owing to the random motion of charge carriers and depends on temperature and device resistance [72]. Johnson noise is considered as white noise because it is constant through the frequency spectrum [69].

The magnetic resolution (B_{min}) is derived from the *PSD* data and using Equation (3.15). In Fig. 3.9(c) B_{min} as a function of f is plotted; it exhibits a similar $1/f$ dependency. The *PSD* and B_{min} values at 10 Hz and 3 kHz are displayed in Table. 3.6.

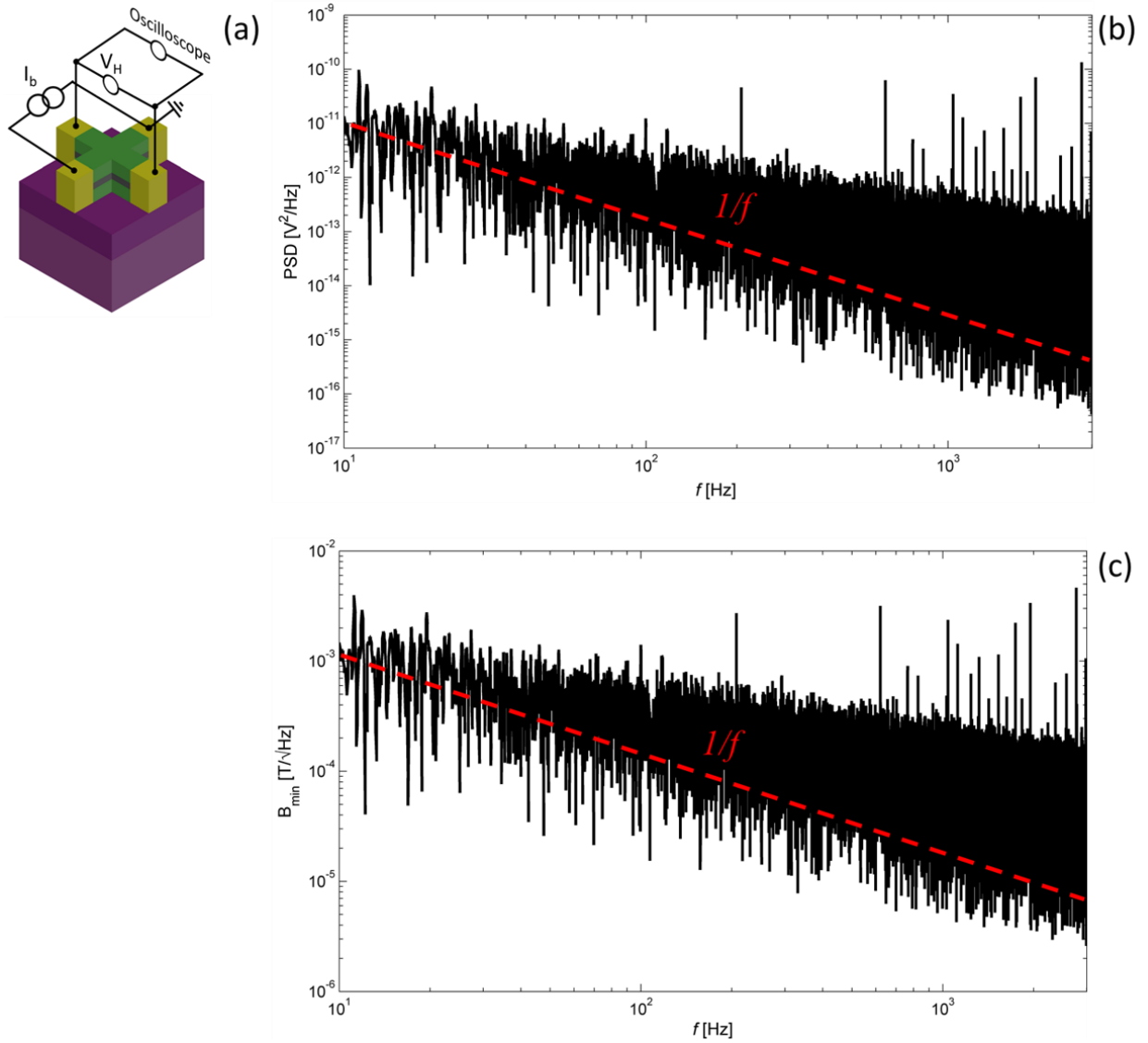


Fig. 3.9. Hall cross noise response at RT under vacuum conditions. (a) Hall cross schematic of the electrical connections used for the measurements. (b) PSD as a function of f . (c) B_{\min} as a function of f . Measurement conditions: injected AC current $1 \mu\text{A}$, absence of the magnetic field, and without gate voltage. The red dashed line illustrates $1/f$ dependency.

Table 3.6 provides a comparison of Hall-cross parameters at ± 50 mT and ± 5000 mT and no-gated voltage. n_s and μ differ by 12%, while S_I and S_V differ by 18%. S_I and S_V are also largest for positive magnetic fields. In addition, this Hall-cross device attained a sensitivity at the microtesla (μ T) level.

Table 3.6. Hall-cross device parameters and sensitivities at RT under vacuum conditions.

I_b (μ A)	n_s (cm^{-2})	μ (cm^2/Vs)	B (mT)	S_I (V/AT)	S_V (V/VT)	PSD (V^2/Hz)		B_{min} (T/\sqrt{Hz})	
						10 Hz	3 kHz	10 Hz	3 kHz
1	2.53×10^{11}	78,229	-50	2,486	0.62	10^{-11}	10^{-14}	1^{-3}	41^{-6}
			50	2,505	0.63				
1	3.22×10^{11}	61,446	-5,000	987	0.25				
			5,000	1,752	0.44				

3.2.3 Measurements under ambient conditions

The Hall cross- and EMR-device transport measurements were performed using a variable temperature insert (VTI) with a 16-pin custom probe sample holder together with a lock-in amplifier (SR830) and an oscilloscope (MSO-X 3014T), connected in parallel to the differential inputs of the lock-in amplifier for the noise measurements. A source meter (Keithley 2400) was used to control the gate voltage applied to the graphene device.

The experimental setup is shown in Fig. 3.10. A permanent magnet provided the applied magnetic field; its intensity was controlled by changing the distance between the magnet surface and the devices. The correct spacing to provide magnetic fields of ± 50 mT at the devices was set by using a commercial Gauss meter. Measurements were performed at RT and without environmental noise cancellation.

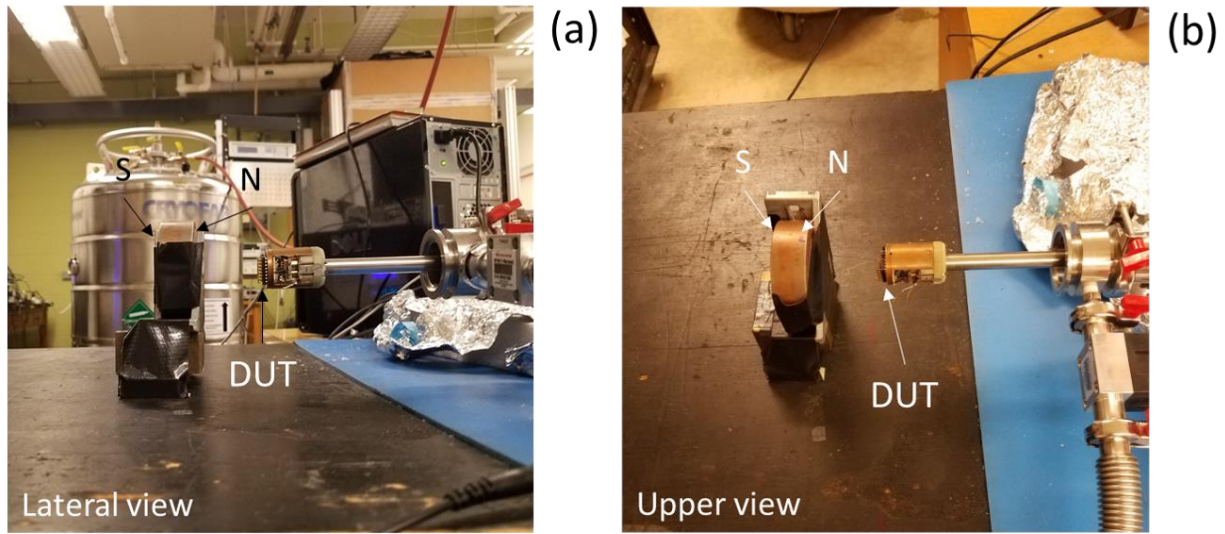


Fig. 3.10. Ambient condition experimental setup (a) lateral view and (b) upper view. A permanent magnet is used to induce a magnetic field of ± 50 mT.

Resistivity measurements

The measurements were conducted with the same current conditions as described in the resistivity measurements from section 3.2.2 using the VTI. The values obtained for both devices are presented in Table 3.7. Comparison of parameters for the Hall-cross and EMR devices indicates that the resistivity (p) and sheet resistance (R_s) are smaller for the Hall cross, while the total resistance (R) and the contact resistance (p_s) difference are not significant.

Table 3.7. Resistivity measurements results of the Hall-cross and EMR devices using VTI at RT under ambient conditions

	$R_{longitudinal} (\Omega)$	$R_{transversal} (\Omega)$	$R (\Omega)$	$p (\Omega m)$	$R_s (\Omega/sq.)$	$p_s (k\Omega \mu m)$
Hall cross	298	305	301	1.02×10^{-7}	301	2.68
EMR	-	-	329	3.97×10^{-8}	116	2.34

The gate voltage measurements are performed by applying a DC voltage from -20 V to 20 V with a 0.1 V/s rate. Sweeps started from positive to negative voltages and then back to positive. This cycle was repeated twice. The resistance as a function of gate voltage measured with the injected current into the Hall cross along orthogonal directions is displayed in Fig. 3.11(a-b). Fig. 3.11(a) shows the longitudinal-direction transfer curve, which exhibits hysteresis; the resistance values at the maximum negative and positive gate voltages differ by 24%. A similar behavior is observed in the case of the transversal-direction transfer curve shown in Fig. 3.11(b). Note that the shift of the CNP is narrower for this case. Last, there is a difference of 3.5% between the maximum peaks of the longitudinal and transversal directions.

Wang et al. [73] reported that two mechanisms explain the hysteresis and shift of the maximum resistivity peak (CNP): charge transfer and capacitive gating. In charge transfer, a hole (electron) transfer from graphene (charge traps) to charge traps (graphene) causes a right shift. In capacitive gating, when inversely charged ions move towards graphene, dipoles align with the external electric-field direction and the local electric field near graphene is enhanced. This leads to a significant attraction of charges from the metallic contacts, thereby incrementing the carrier density, and a left shift occurs.

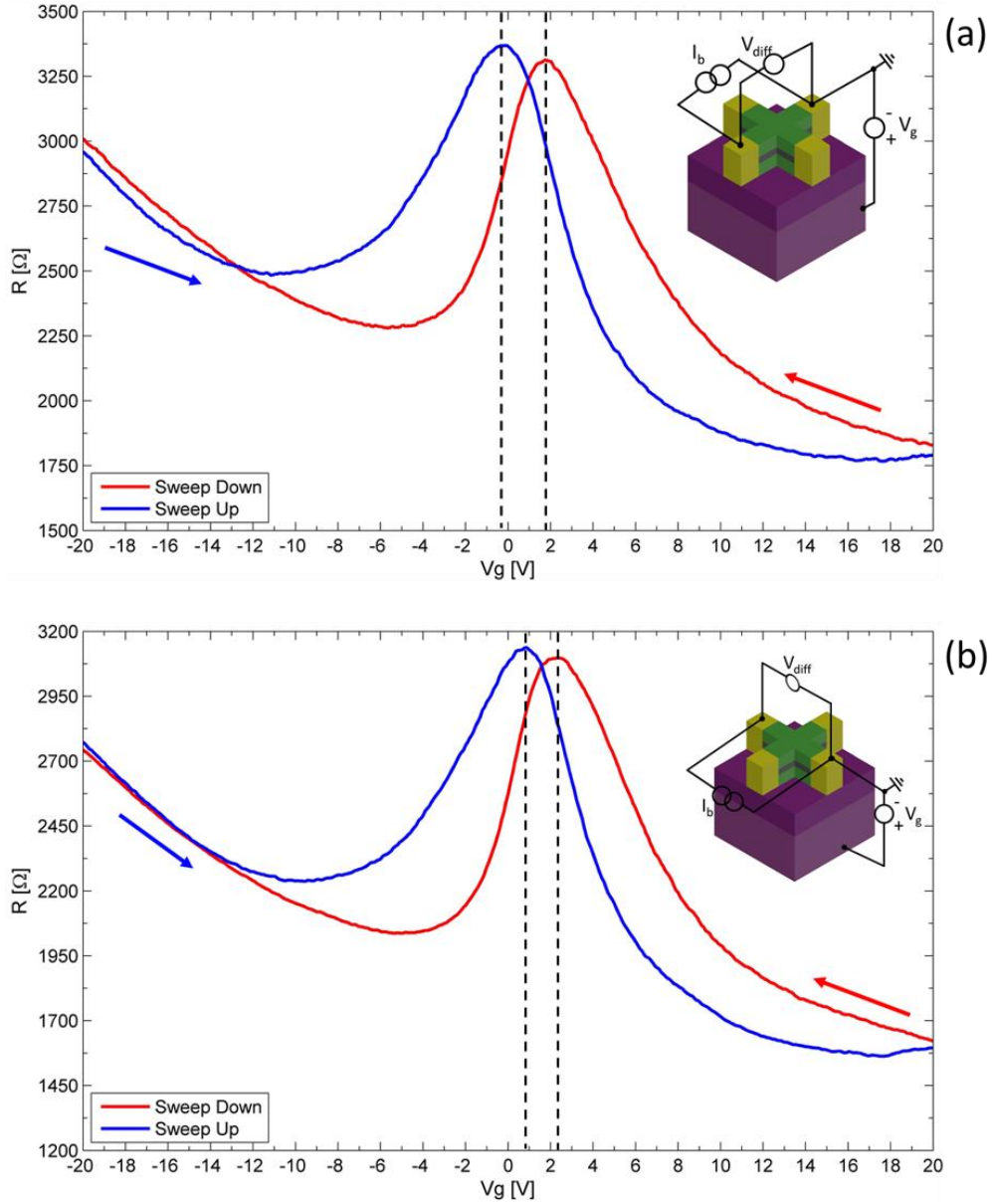


Fig. 3.11. Transfer curves measured at orthogonal channels of the Hall cross in ambient conditions and without applied magnetic field. (a) Longitudinal direction, CNP at $V_g = -0.1$ V and $V_g = 1.8$ V. (b) Transversal direction, CNP at $V_g = 0.8$ V and $V_g = 2.3$ V. The applied current was $1 \mu\text{A}$. The arrows show the direction of gate voltage sweep. The inset shows the electrical connections used for the measurements.

The dominant mechanism for the behavior of the transfer curves of Fig. 3.11(a-b) is the capacitive gate. This is inferred from the hysteresis curves and the shift of the maximum resistivity peak seen while sweeping from negative gate bias voltage towards positive values. This indicates that electrons remained trapped until the gate polarity is switched. Therefore, we investigated the effect of decreasing the sweeping rate of the gate voltage in an attempt to remove the hysteresis from the transfer curves.

The effect of reducing the gate bias voltage sweeping rate is illustrated in Fig. 3.12(a-d). A wider shift of the CNP is observed with decreasing sweeping rate. This is due to the fact that the charges are trapped for longer than a few seconds; as a result, it takes more time to reach the maximum resistivity peak. Another effect that is observed in the figures is the opposite change of the resistance peaks for gate voltage sweeping rates of 0.1 V/s, 0.5 V/s, and 0.01 V/s. This does not occur in Fig. 3.11 because p_s from the orthogonal channel total resistance (R_w , p_s , and R_s) dominates R_s , hiding this effect. The electrical connections shown in Fig. 3.12 only measured R_s .

When the voltage starts at positive (negative) gate voltage, electrons (holes) in graphene are slowly trapped into the trap sites. After some time, the graphene experiences a more negative (positive) potential than applied by the gate voltage. These trapped charges under graphene dope the graphene into opposite polarity. Therefore, the negative regimen sweeping shifts down the CNP because of charge screening from injected holes into trap sites. Similarly, the CNP shifts up because the positive regimen sweeping induces electron injection into the trap centers [73]. Finally, in the case of the sweeping rate at 0.001 V/s, it takes a much longer time for the electrons to reach the charge traps sites, preventing the shift down of the CNP.

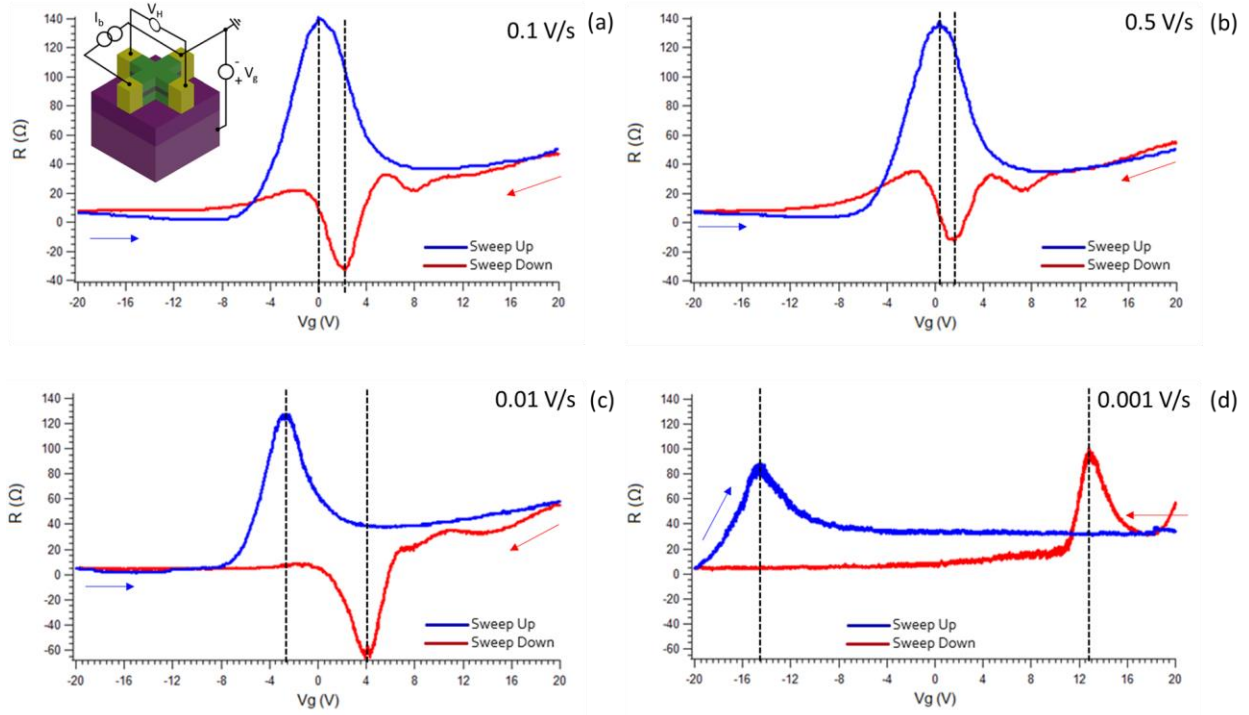


Fig. 3.12. Hall cross longitudinal orthogonal direction sweeping rates of gate voltage dependence. (a-d) R as a function of V_g . Applied current, $1 \mu\text{A}$. Sweep moves from positive to negative polarity (red line) and sweeps back to positive (blue line). Inset shows the schematic of the electrical connections used for the measurements.

The effect of sweeping rates of 0.1 V/s , 0.5 V/s , and 0.01 V/s by applying a current of $10 \mu\text{A}$ is shown in Appendix C (Fig. C.1(a-c)). As seen previously, the CNP broadens as the rate decreases, but the shift of the CNP is smaller (0.75 V) compared to the shift observed with a current of $1 \mu\text{A}$ (2.25 V) at a rate of 0.1 V/s ; see Fig. C.1(a). In Fig C.2(a-c) similar results are given for an injection current of $100 \mu\text{A}$. The results show the same behavior as with the previously applied currents. However, there is no shift of the CNP at the rate of 0.1 V/s , which is displayed in Fig. C.2(a).

The results obtained in the attempt to remove the hysteresis by changing the sweeping rate of the gate voltage agrees with Reference [73] the hysteresis increases as the sweeping rate decreases. Additionally, the results from carrying out the voltage sweep twice agree with the reported work from Reference [74]. They show that performing voltage sweeping multiple times (around 10) results in saturation of the hysteresis, meaning that it becomes independent of rate and voltage range. Our results are consistent with those reports and confirm that the hysteresis

does not depend on the magnitude of the applied current. Based on the fact that the shift of the CNP is narrower at the rate of 0.1 V/s, we used this setting for conducting sheet resistance measurements using the van der Pauw configuration. Fig. 3.13 shows the average sheet resistance as a function of gate voltage with the CNP at $V_g = 1.9$ V; the asymmetry between polarities differs by 27%.

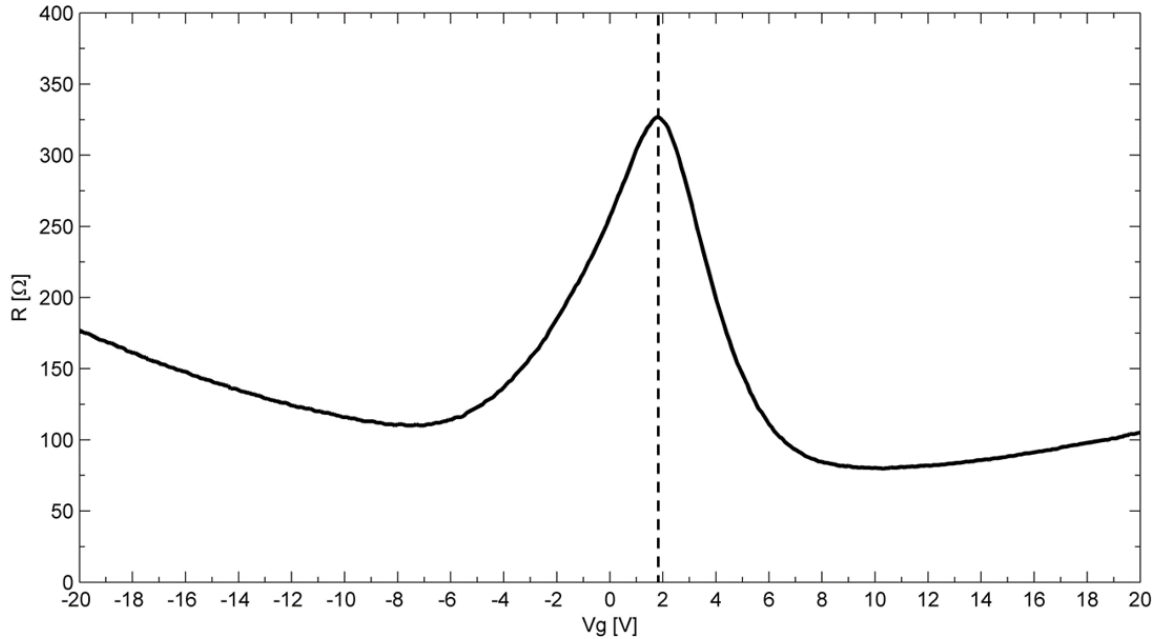


Fig. 3.13. Hall cross average R_s as a function of V_g , employing the van der Pauw configuration. Applied current, 1 μ A. CNP at $V_g = 1.9$ V.

Hall effect measurements

Sinusoidal currents of 1 μ A, 10 μ A, and 100 μ A at 7.7 Hz, fixed magnetic fields of -50 mT, 0 mT, and 50 mT, and gate voltages from -20 V to 20 V at a rate of 0.1 V/s were employed for these measurements.

The Hall-cross voltage response vs. gate voltage at different applied magnetic fields with an injection current of 100 μ A is shown in Fig. 3.14(a). As expected, the voltage increases proportionally with the positive magnetic field and decreases for the opposite polarity. The slope of the curves at a constant applied magnetic field (red and blue line) represents the change of induced electrons (holes) to holes (electrons) as the gate voltage is swept from positive (negative) to negative (positive) polarity. The intersect of the slopes also represents the position of the CNP at $V_g = 0.8$ V. Furthermore, the plot shows asymmetry between the minimum and

maximum values of the voltage in a constant applied magnetic field. The values attained for positive gate voltages are higher than those corresponding to the case of negative bias.

The carrier density (n_s) is extracted from the slope values of the three data sets at $B = -50$ mT, 0 mT, and 50 mT. The carrier mobility (μ) is derived using the sheet resistance (R_s) measurement from Fig. 3.13 and the value inferred for n_s . The current (S_I) and voltage (S_V) sensitivities are estimated from the voltage curves shown in Fig. 3.14(a). The plot of μ vs. n_s shown in Fig. 3.14(b) provides their correlation. The relationship between S_I and V_g is shown in Fig. 3.14(c). No significant hysteresis of the CNP location is seen in the curve. The obtained magnetic response parameters are presented in Table. 3.8.

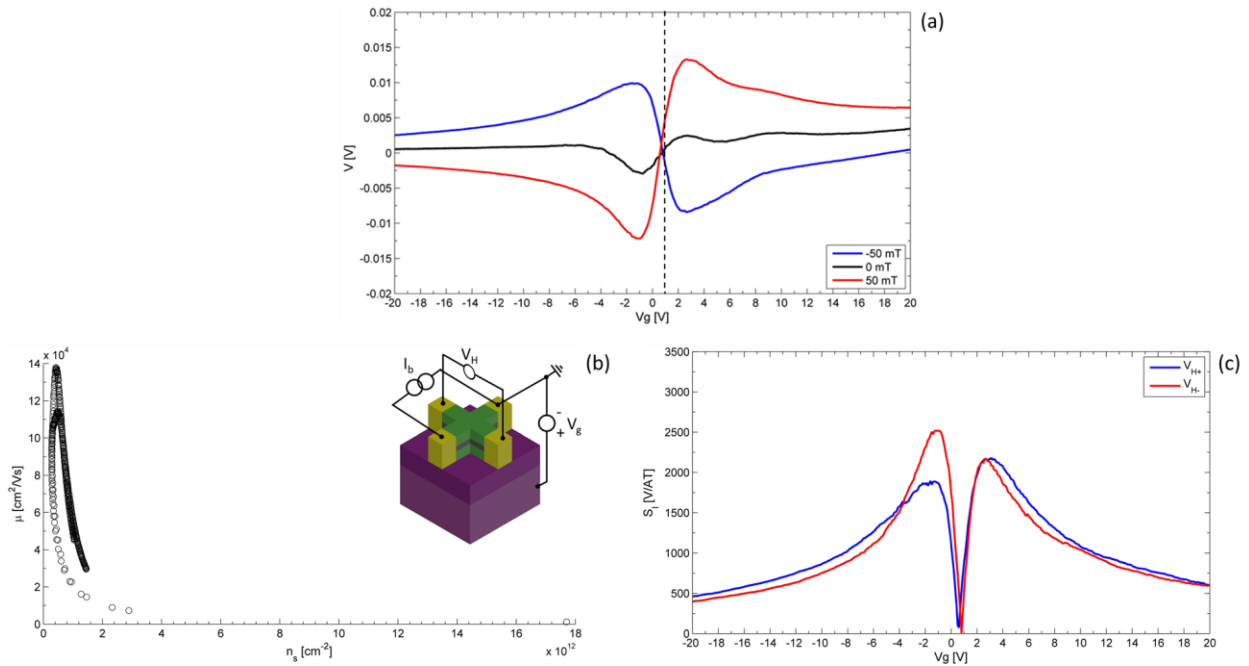


Fig. 3.14. Voltage response of the Hall cross at RT under ambient conditions at 0 and ± 50 mT. (a) V as a function of V_g . (b) μ as a function of n_s . (c) S_I as a function of V_g at V_{H+} (V_H (50 mT) – V_H (0 mT), blue line) and V_{H-} (V_H (-50 mT) – V_H (0 mT), red line). The injection current was 100 μ A. Fixed magnetic fields of -50 mT (blue line), 0 mT (black line), and 50 mT (red line). Inset show the electrical connections used for the measurements. From the schematic, I_b on the left side, V_H on the top side, and V_g on the right side.

The magnetic response of the Hall cross with an injection current of 1 μA is shown in Appendix D (Fig. D.1(a)). The plot shows asymmetry of the voltage values measured as a function of gate bias voltage polarity. Fig. D.1(b) shows μ versus n_s , while Fig. D.1(c) shows S_I versus V_g with a significant hysteresis of the CNP location. Similar results are shown in Fig. D.2A when an injection current of 10 μA is applied. Table 3.8 provides a compilation of measurements conducted under these various conditions.

EMR measurements

EMR measurements were conducted under the same conditions as the Hall measurements. However, the gate bias voltage sweep was carried out ten times to improve on previous results with only two sweeps. The magnetic response of the EMR device at a current of 100 μA is shown in Fig. 3.15(a). V_{diff} vs. V_g shows that the CNP is shifted towards the negative polarity of V_g ; this shift is attributed to holes trapped in the oxide traps under high electric fields [75]. It can also be seen that the maximum value of V_{diff} occurs with negative V_g . The extracted n_s and μ are plotted in Fig. 3.15(c), showing a more accurate estimate of these parameters owing to hysteresis saturation. The plot of S_I vs. V_g is given in Fig. 3.15(e). No hysteresis or shift of the CNP location is observed.

An additional sweep of V_g was conducted over a wider voltage range (Fig. 3.15(b)). Note that for these measurements, the gate voltage sweep was carried out only once. The purpose of this wider voltage sweep was to identify more precisely the CNP location. The plot shows the V_g value at which the maximum value of V_{diff} is obtained. Note that the CNP is shifted by 2.5 V (from -15 V to -17.5 V). Fig. 3.15(d) shows μ versus n_s , and it is seen that the maximum mobility is higher compared to the maximum mobility value from Fig. 3.15(c). Here, the effect of hysteresis saturation is clearly seen and reflected in the inaccuracy to calculate μ . Similarly, the plot of S_I vs. V_g given in Fig. 3.15(f) shows that the maximum value is smaller compared to the one from Fig. 3.15(e) even though its mobility is higher. However, S_I depends on n_s , and from Table 3.8, which presents the magnetic response parameters of the EMR device, is seen to be higher, meaning that $\Delta V/\Delta B$ is smaller at the wider range.

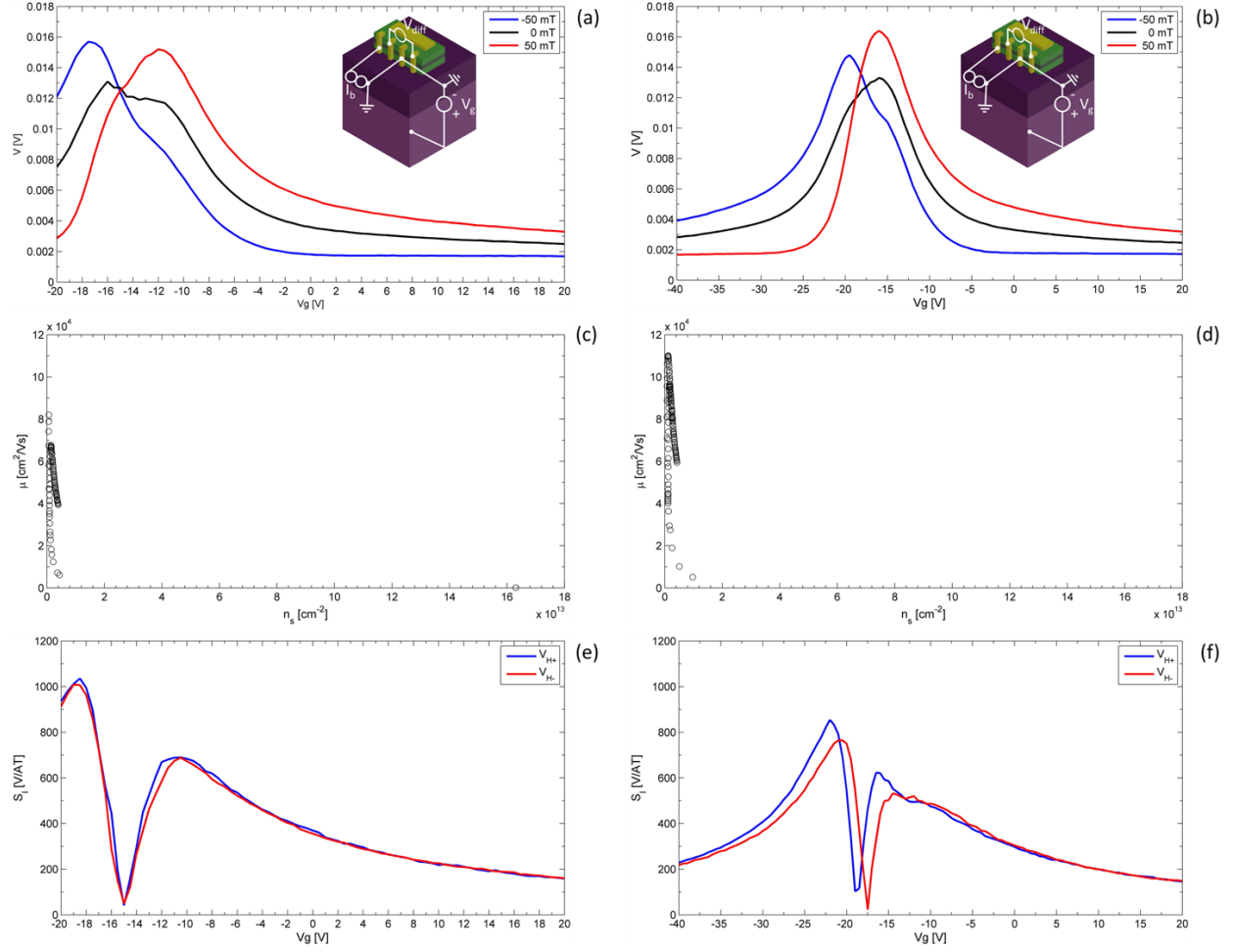


Fig. 3.15. Magnetic response of the EMR device at RT under ambient conditions. The applied gate voltage is swept from -20 V to 20 V for (a, c and d) whereas for (b, d and e) it is swept from -40V to 20V. (a) V_{diff} vs. V_g ; (b) V_{diff} vs. V_g for the wider gate voltage range (-40 V to 20 V); (c) μ as a function of n_s ; (d) μ as a function of n_s ; (e) S_I as a function of V_g . and (f) S_I as a function of V_g . V_{H+} (V_H (50mT) – V_H (0mT), blue line) and V_{H-} (V_H (-50mT) – V_H (0mT), red line) is presented in (e) & (f). Applied current, 100 μ A. Fixed magnetic fields of -50 mT (blue line), 0 mT (black line), and 50 mT (red line). Inset show the electrical connections used for the measurements. From the schematic, I_b on the left side, V_H on the top side, and V_g on the right side.

The EMR device response vs. gate bias voltage when a current of $1 \mu\text{A}$ is injected is shown in Appendix D, Fig. D.3(a). It can be seen that the CNP location is at $V_g = -5 \text{ V}$. The maximum voltage peaks occur at different values of the gate voltage for applied magnetic fields of 50 mT and -50 mT . The response for the wider gate voltage range is also illustrated in Fig. D.3(b). In this case, the CNP is shifted from -5V to -20.5V , and the maximum voltage peaks are smaller, resulting in a smaller $\Delta V/\Delta B$. This shows significant differences between the carrier density and mobility plots illustrated in Fig. D.3(c-d). At the narrow gate voltage range, n_s (see Fig. D.3(c)) is smaller, resulting in a higher value of μ than that obtained at the wider range, as seen in Fig. D.3(d). Additionally, the plot of S_I vs. V_g shown in Fig. D.3 (e-f) shows the same effect and is due to the differences in n_s . It is also seen that the S_I curve does not present hysteresis in the CNP location. Nevertheless, hysteresis is seen in the maximum voltage peaks in the narrow gate voltage range. This differs for the case when the injection current is $100 \mu\text{A}$.

The response of the EMR at a current of $10 \mu\text{A}$ for both the narrow range and wider gate voltage scan range is shown in Figs. D.4(a) and Fig. D.4(b), respectively. The plots show that the CNP localized at $V_g = -12 \text{ V}$ shifts to $V_g = -19 \text{ V}$. A major difference between the maximum voltage peaks at $B = -50 \text{ mT}$ and $B = 50 \text{ mT}$ is seen as well. In addition, plots for the relationship between μ vs. n_s as well as for S_I vs. V_g are given in Figs. D.4(c-d) and Figs. D.4(e-f), respectively. For this case, the effect of hysteresis saturation is observed, showing agreement for the case when the injection current is $100 \mu\text{A}$.

Finally, another point worth mentioning is that the CNP shifted to the left as the current increased when the voltage sweep was carried out ten times. In contrast, when the voltage was swept only once, the CNP shifted to the right as the current increased. The obtained parameters values for the magnetic response at currents of $1 \mu\text{A}$ and $10 \mu\text{A}$ are presented in Table 3.8.

Noise measurements

The Hall-cross noise measurements were performed at RT under ambient conditions in the absence of a magnetic field (B). Injection currents were $1\ \mu\text{A}$, $10\ \mu\text{A}$, and $100\ \mu\text{A}$ at $7.7\ \text{Hz}$ and the gate voltage (V_g) was swept from $-20\ \text{V}$ to $20\ \text{V}$ at a rate of $0.1\ \text{V/s}$. The data are acquired at each value of V_g during the sweep. The noise level varies as V_g changes, which allows minimization of the PSD , and thus the magnetic resolution (B_{min}) can also be optimized. The PSD vs. V_g at frequencies of $10\ \text{Hz}$ and $3\ \text{kHz}$ are shown in Fig. 3.16(a) and Fig. 3.16(b), respectively. A comparison of the PSD magnitudes shows a four-orders-of-magnitude decrement on account of the $1/f$ dependency. It can also be seen that the PSD magnitude increases as the current increases. Similarly, the B_{min} as a function of V_g at frequencies of $10\ \text{Hz}$ and $3\ \text{kHz}$ are shown in Fig. 3.16(c) and Fig. 3.16(d), respectively. B_{min} shows the same behavior as PSD with respect to the $1/f$ dependency. However, B_{min} improves as the current increases, as seen in Fig. 3.16(d). The noise measurement numerical results are presented in Table. 3.8.

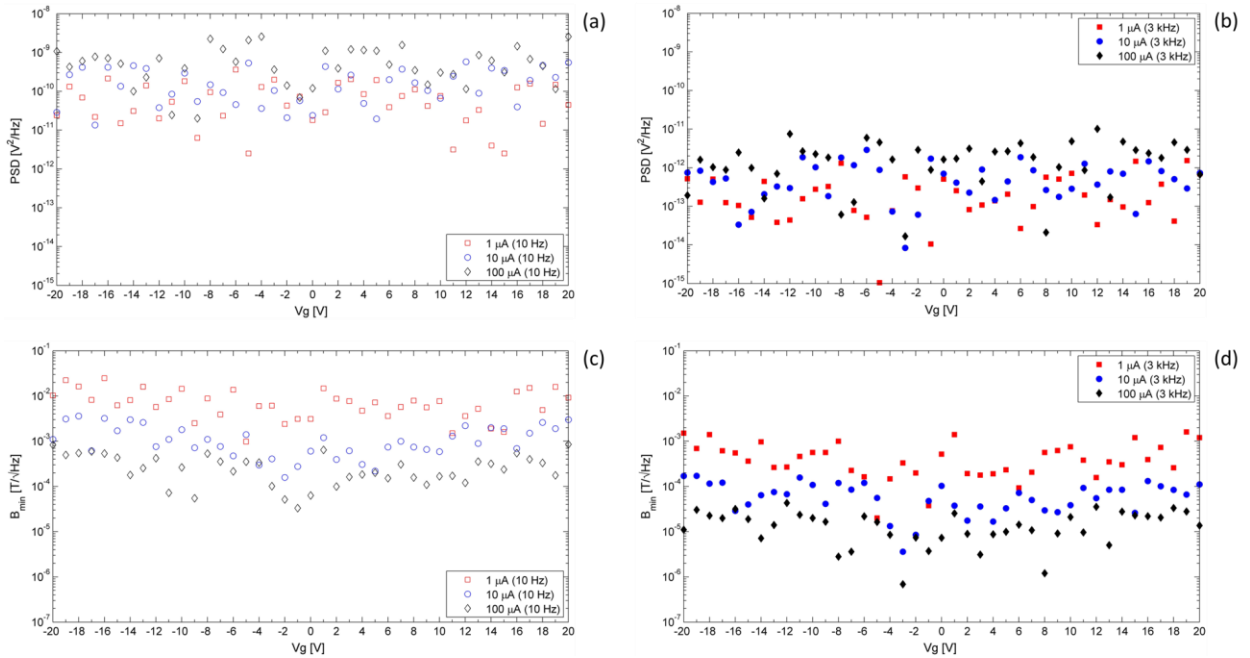


Fig. 3.16. Hall cross noise response at different gate voltages at RT under ambient conditions. PSD as a function of V_g . at (a) $10\ \text{Hz}$ and at (b) $3\ \text{kHz}$. B_{min} as a function of V_g at (c) $10\ \text{Hz}$ and at (d) $3\ \text{kHz}$. Applied currents, $1\ \mu\text{A}$ (square markers), $10\ \mu\text{A}$ (circle markers), and $100\ \mu\text{A}$ (diamond markers). The blank (filled) markers correspond to the frequency of $10\ \text{Hz}$ ($3\ \text{kHz}$).

The B_{min} value for each applied current has corresponding n_s , μ , and S_I values as presented in Table 3.9. The PSD value for the gate voltages at which B_{min} attains the lowest value is plotted as a function of frequency (f) and illustrated in Fig. 3.17(a). The corresponding derived B_{min} is shown in 3.17(b).

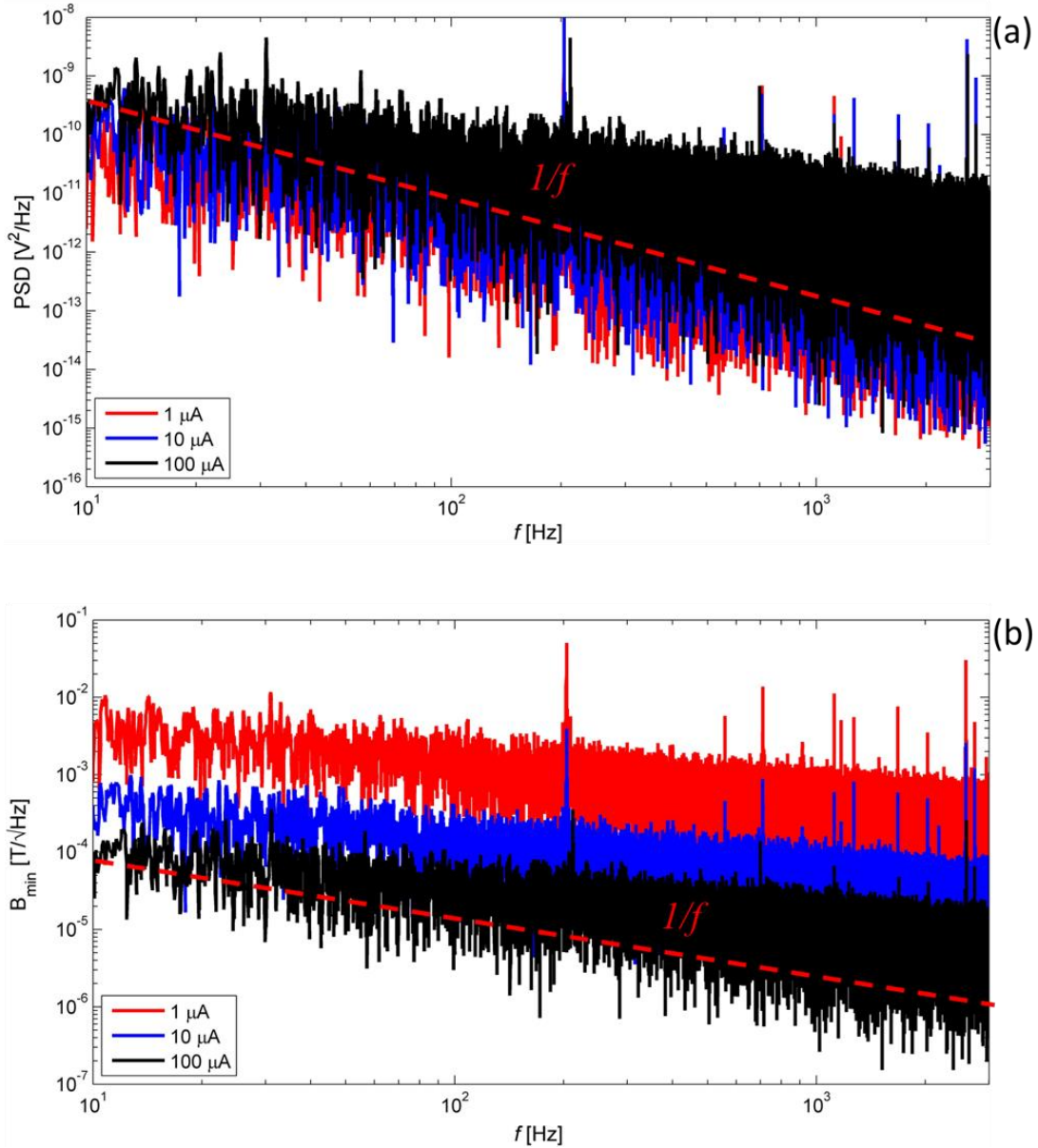


Fig. 3.17. a). PSD of B_{min} vs. f . Values are obtained at the gate bias voltage at which B_{min} minimizes. (b) B_{min} vs. f for different injected currents, 1 μA (red), 10 μA (blue), and 100 μA (black). Reference of the $1/f$ noise dependency (red dashed line).

The EMR-device noise measurements were conducted at RT under ambient conditions at zero magnetic field. For each injected AC current (7.7 Hz), the gate voltage range is swept at 0.5 V/s as follows: -12.5 V to 7.5 V for 1 μ A; 0 V to -20 V for 10 μ A and 100 μ A.

The *PSD* vs. V_g at frequencies of 10 Hz and 3 kHz are shown in Fig. 3.18(a) and Fig. 3.18(b), respectively. B_{min} vs. V_g at 10 Hz is displayed in Fig. 3.18(c), while B_{min} versus V_g at 3 kHz is shown in Fig. 3.18(d). The *PSD* and B_{min} show $1/f$ dependency and their magnitude decreases by four orders of magnitude at 3 kHz. B_{min} is observed to improve as the input current increases from 1 μ A to 10 μ A. Numerical results from this study are presented in Table 3.8.

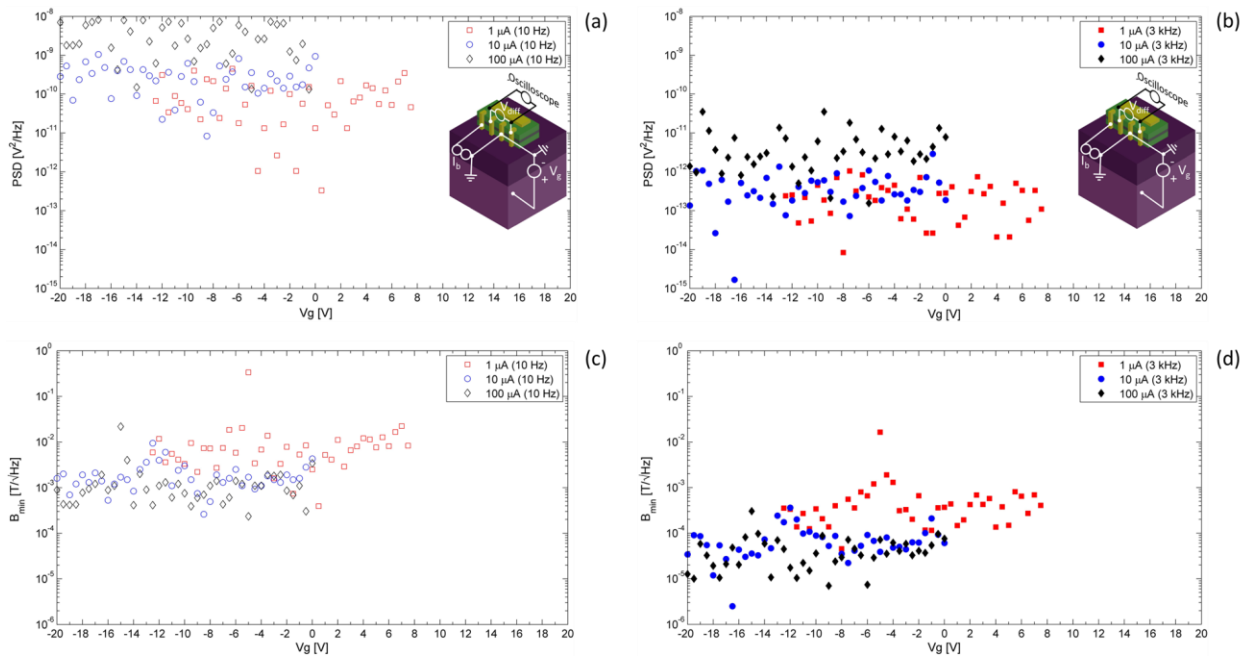


Fig. 3.18. EMR noise response vs. gate voltages at RT under ambient conditions. *PSD* vs. V_g . at (a) 10 Hz and at (b) 3 kHz. B_{min} vs. V_g at (c) 10 Hz and at (d) 3 kHz. Injected currents, 1 μ A (squares), 10 μ A (circles), and 100 μ A (diamonds). The blank (filled) markers correspond to the frequency of 10 Hz (3 kHz).

The increment of the $1/f$ noise as the bias current increases for the Hall-cross and the EMR devices agrees with studies reported in [49], [69], [76]. In addition, B_{min} improves by increasing I_b on account of the relation given in Equation (3.15). Kayyalha et al. [77] reported that the $1/f$ noise in graphene-h-BN-based devices is reduced by one order of magnitude in comparison to graphene-based devices fabricated directly on SiO_2 substrates. Our results agree with their work: the *PSD* is 10^{-15} V^2/Hz (see Table 3.8) for an injection current of 1 μ A for the trilayer (h-BN/G/h-BN) EMR device, whereas for the same injected current, the (G/ SiO_2) EMR-device

PSD is 10^{-14} V^2/Hz (see Appendix E). Furthermore, employing trilayer structures prevents environmental exposure of graphene, which results in $1/f$ noise increments, as reported by Romyantsev et al. [78].

The results from the magnetic and noise response of the Hall-cross and EMR devices are presented in Table 3.8. The difference in carrier density (n_s) and mobility (μ), vs. injection current for the different devices is first explained. The resistor employed to fix the value of the injected current to the EMR device from the output source of the lock-in amplifier does not affect the currents of 1 μA (1 $M\Omega$) and 10 μA (100 $k\Omega$). However, it affects the current of 100 μA because the resistance of the current channel is ~ 10 $k\Omega$ (see Fig. B.3). Consequently, the change of voltage due to the magnetic field is smaller and is the reason why n_s and μ of the EMR20 at 100 μA is two times higher than values measured at the other currents. The same effect is seen in case of the EMR40. The Hall-cross device is not affected by this issue because its current channel resistance is ~ 4 $k\Omega$ (see Fig. B.2). Thus, the change of voltage vs. applied magnetic field is proportional to the value of the injected currents; the values of n_s are not significant, but as expected, for μ are significant.

The hysteresis of the measured resistance vs. gate voltage illustrated in Fig. 3.11 impacts the accuracy in determining mobility (μ) from resistivity measurements. The hysteresis is attributed to the effect of adsorbates like water molecules, oxygen, and organics resulting in the generation of charge carriers and dielectric trap defects [79]–[82]. The latter occurs less frequently owing to the fact that high current injection into the SiO_2 causes a local breakdown of defects. The results of carrying out the sweep of the gate voltage ten times in the EMR device shows that the hysteresis is suppressed, in agreement with the work reported in Reference [74]. Consequently, μ is determined more accurately in the EMR devices than in the Hall-cross device.

The stack assembly was performed inside a glove box, and encapsulating graphene within h-BN protects it from environmental contaminants. These two fabrication steps prevent graphene surface contamination. However, the mechanical exfoliation was made in ambient conditions where water molecules or oxygen contaminate the surface before the stack assembly. A method to remove the hysteresis due to adsorbates is current annealing under a helium atmosphere [83], [84]. Passing a high current in graphene produces local heating, which can remove impurities from the surface. Consequently, the benefits of this process are an improvement in quality,

hysteresis reduction, and shift of the CNP back to zero. Another benefit is improvement of contact resistance [81], [85].

The current sensitivity (S_I) of the EMR20 decreases as the carrier density (n_s) increases proportionally to the applied current. The same effect is seen in the EMR40 and the Hall cross, which confirms that S_I increases (decreases) as n_s decreases (increases). On the other hand, the voltage sensitivity (S_V) of the Hall cross increases as the mobility (μ) increases because of the relationship between them. The EMR device shows a smaller sensitivity in comparison to the Hall-cross device.

The PSD of the Hall cross and the EMR20 are comparable at 3 kHz and for applied currents of 1 μA and 10 μA . The one order-of-magnitude difference between them for an injection current of 100 μA is attributed to the resistor issue explained previously. Furthermore, the Hall-cross magnetic resolution (B_{min}) is smaller compared to the EMR20 at 3 kHz and for a current of 1 μA . However, for an injection current of 10 μA , the Hall-cross B_{min} is higher than EMR20 B_{min} at 3 kHz, which shows the advantages of the EMR effect.

Finally, the Hall cross shows that its sensitivity and minimum detectable field are better than those of the EMR devices. This means that the Hall-cross signal response is higher than the EMR-device signal response. In order to confirm the advantages of the Hall cross– over the EMR device, an additional characterization is required in which the Hall-cross hysteresis is suppressed. The possible results are: i) Hall-cross S_I and B_{min} remain the same; ii) Hall-cross S_I and B_{min} are similar to those of the EMR device S_I and B_{min} ; and iii) Hall-cross S_I and B_{min} are smaller than the EMR-device S_I and B_{min} .

Table 3.8. Transport parameters and noise measurements for trilayer Hall-Cross and EMR devices at RT under ambient conditions.

I_b (μA)	n_s (cm^{-2})	μ (cm^2Vs)	S_I (V/AT)	S_V (V/VT)	PSD (V^2/Hz)		B_{min} ($T^{\wedge}Hz$)	
					10 Hz	3 kHz	10 Hz	3 kHz
Hall cross	1	2.42×10^{11} $V_g = -1.9V$	2,880 $V_g = -1.6V$	0.78 $V_g = -1.6V$	2.51×10^{-12} $V_g = -5V$	1.05×10^{-15} $V_g = -5V$	977×10^{-6} $V_g = -5V$	20×10^{-6} $V_g = -5V$
	10	2.24×10^{11} $V_g = 3V$	3,370 $V_g = 0V$	0.92 $V_g = 0V$	1.05×10^{-10} $V_g = -3V$	8.37×10^{-15} $V_g = -3V$	406×10^{-6} $V_g = -3V$	3.6×10^{-6} $V_g = -3V$
	100	2.83×10^{11} $V_g = -1.2V$	2,523 $V_g = -1.2V$	0.68 $V_g = -1.2V$	3.63×10^{-10} $V_g = -3V$	1.67×10^{-14} $V_g = -3V$	101×10^{-6} $V_g = -3V$	686×10^{-9} $V_g = -3V$
EMR 20	1	3.09×10^{11} $V_g = -8.5V$	2,136 $V_g = -9V$	-	2.15×10^{-10} $V_g = -8V$	8.37×10^{-15} $V_g = -8V$	7.2×10^{-3} $V_g = -8V$	45.3×10^{-6} $V_g = -8V$
	10	3.72×10^{11} $V_g = -15.5V$	1,708 $V_g = -15.5V$	-	4.81×10^{-10} $V_g = -16.5V$	1.67×10^{-15} $V_g = -16.5V$	1.4×10^{-3} $V_g = -16.5V$	2.5×10^{-6} $V_g = -16.5V$
	100	6.11×10^{11} $V_g = -18.5V$	1,036 $V_g = -18.5V$	-	1.52×10^{-9} $V_g = -9V$	2.10×10^{-13} $V_g = -9V$	594×10^{-6} $V_g = -9V$	7×10^{-6} $V_g = -9V$
EMR 40	1	5.07×10^{11} $V_g = -24.5V$	1,277 $V_g = -24.5V$	-	-	-	-	-
	10	3.63×10^{11} $V_g = -22.5V$	1,779 $V_g = -22.5V$	-	-	-	-	-
	100	7.89×10^{11} $V_g = -21.5V$	854 $V_g = -26.5V$	-	-	-	-	-

This work trilayer EMR, gate voltage sweeps from -20 V to 20 V (EMR20) and from -40 V to 20 V (EMR40).

3.2.4 Comparison with relevant published works

The Hall-cross and EMR device characterization results of this work are summarized in Table 3.9 and compared with reported values from the literature. The transport parameters and sensitivity values measured under ambient conditions are given in the bottom part of the table. The upper portion of the table provides the measurements conducted under vacuum conditions.

The contact resistance (p_s) reported by Wang et al. [48] of $150 \Omega \mu\text{m}$ for a metal contact of Cr//Pd/Au (1/15/50 nm) and of $180 \Omega \mu\text{m}$ for Cr/Au (10/50 nm) are one order of magnitude lower compared to that measured for both the Hall cross p_s of $2,680 \Omega \mu\text{m}$ in which a metal contact of Cr/Au (40/40 nm) was employed and the EMR device, p_s of $2,340 \Omega \mu\text{m}$, in which a Ti/Au (10 nm/60 nm) metal contact was used. It is noted that the p_s reported for our devices falls within the range of values reported by others: $1,000$ to $10^6 \Omega \mu\text{m}$ (Cr/Au (10/20 nm)) [86], $3,000 \Omega \mu\text{m}$ (Cr/Au (100/10 nm)) [87], and $5,000 \Omega \mu\text{m}$ (Cr/Au (5/150 nm)) [88].

Additionally, Giubileo et al. [61] reported a broad range of experimental contact resistance values from different metal combinations used for graphene contacts. In their comparison, they include deposition techniques, type of measurement to determine p_s , and source of graphene. Their results show that there is wide variability and not fully reproducible fabrication of graphene contacts, a challenge that needs to be addressed.

The previous comparison shows that the metal thickness and the additional layer of Pd could be factors accounting for differences in p_s . Another factor is related to the fabrication process, as the graphene surface is often contaminated by lithography photoresists and affects the contact resistance. Robinson et al. [89] reported evidence of photoresist residue on graphene after performing X-ray photoelectron spectroscopy (XPS). They show single and double bonds of carbon with oxygen that pristine graphene does not have. They reported that O_2 plasma treatment before metal deposition removes the photoresist residue and improves the contact resistance.

Table 3.9. Comparison of transport parameters and sensitivities between our devices and representative examples from the literature.

	P_s ($\Omega \mu\text{m}$)	n_s (cm^{-2})	μ (cm^2/Vs)	B (mT)	I_b (μA)	S_I (V/AT)	B_{\min} ($\text{T}/\sqrt{\text{Hz}}$)	f (kHz)
Vacuum conditions								
HCS1	150	2×10^{11}	140,000	± 50	10 100	4,100, $V_g = -10\text{V}$	$\sim 2^{-6}$ $\sim 250^{-9}$ 50^{-9}	3
Hall cross	2.78^3	2.5×10^{11}	78,000	± 50	1	2,496, $V_g = 0\text{V}$	41^{-6}	3
Ambient conditions								
Hall cross	2.68^3	3.5×10^{11} 2.8×10^{11} 3.4×10^{11}	148,000 130,000 107,000	± 50	1 10 100	1,907, $V_g = -5\text{V}$ 2,516, $V_g = -3\text{V}$ 1,883, $V_g = -3\text{V}$	20^{-6} 3.6^{-6} 686^{-9}	3
EMR20	2.34^3	3.2×10^{11} 3.9×10^{11} 9.6×10^{11}	62,540 94,630 46,770	± 50	1 10 100	2,021, $V_g = -8\text{V}$ 1,611, $V_g = -16.5\text{V}$ 656, $V_g = -9\text{V}$	45^{-6} 2.5^{-6} 7^{-6}	3
EMR1	120^3	5.5×10^{12}	1,231	± 50	1 10 100	116 ($V_g = 0\text{V}$)	1.3^{-3} 98.5^{-6} 18.1^{-6}	3
EMR2	160^3	5.7×10^{12}	1,177	± 50	1 10 100	110 ($V_g = 0\text{V}$)	1.9^{-3} 221.3^{-6} 62.4^{-6}	3

HCS1, Hall-cross device reported in Reference [49], p_s , n_s and μ are reported in Reference [48]

EMR20, this work trilayer EMR, gate voltage sweeps from -20 V to 20 V

EMR1, device with sensing area of 2.2 mm \times 1.1 mm.

EMR2, device with sensing area of 1.2 mm \times 0.6 mm.

The Hall-cross and EMR20 carrier density values are of the same order of magnitude but higher compared to that reported by Wang et al. [48], see Table 3.9. In their work, they plotted R_s as a function of V_g , showing a symmetric sharp peak. The maximum and minimum values they observed are 1,100 $\Omega/\text{sq.}$ and 40 $\Omega/\text{sq.}$, respectively. In this work, the Hall-cross R_s as a function of V_g (see Fig. 3.13) shows a broad asymmetric peak with maximum and minimum values of 325 $\Omega/\text{sq.}$ and 110 $\Omega/\text{sq.}$, respectively. This indicates a lower-quality graphene.

Comparing our mobilities values of the Hall cross and the EMR20 with values reported by the same authors, our Hall-cross high mobility values (disregarding the variability between currents) does not agree with the quality of our graphene. We know that the hysteresis exhibited in our measurements influences the determination of mobility. On the other hand, in the case of EMR20, the hysteresis is suppressed, and the mobility is inferred more accurately, showing that is smaller than 140,000 cm^2/Vs . This explains why the sensitivity of EMR20 is only a few μT . In the case of the Hall cross, inaccurate mobility determination can also explain the disagreement between measured sensitivities of hundreds of nT with inferred mobilities higher than 140,000 cm^2/Vs rather than tens of nT with the same mobility, as seen in Table 3.9.

The current sensitivity (S_I) of our Hall cross and the EMR20 are smaller when compared with that reported for S_I of 4,100 V/AT by Dauber et al. [49]. In their work, values of p_s , n_s , and μ are not reported, but they used the fabrication methodology described in Reference [48]. They encapsulated graphene in h-BN and fabricated a symmetric cross with a width of 3 μm and length of 5.2 μm (HCS1). From the two-terminal gate voltage orthogonal-direction measurements, no significant shift or hysteresis was observed, indicating the high quality of their graphene. Thus, we assume that the values of n_s and μ are comparable to the ones reported by Wang et al. [48] and given in Table 3.9. The reason for their high S_I is that the change in voltage due to the magnetic field is twice that of our Hall cross and EMR20.

The magnetic resolution (B_{min}) of our Hall-cross sensor is twenty times higher compared to the one from literature for a current of 1 μA under vacuum conditions. The value of B_{min} from Reference [49] is obtained at zero magnetic field, at a voltage of 1 mV, and a current sensitivity of 4,100 V/AT ($V_g = -5\text{V}$ (electron regimen) or $V_g = -10\text{V}$ (hole regimen)). Next, the Hall-cross B_{min} under ambient conditions is compared to the HCS1 B_{min} under vacuum conditions at a current of 100 μA . This comparison is made because the magnetometer operation for biomagnetic signal detection is in a real-life environment rather than in a shielded environment.

The difference between the values differ by a factor of 14. In the case of the EMR20 the same comparison shows a difference of three orders of magnitude between the B_{min} values.

Noise can limit the magnetic resolution of the magnetometer whose two primary electronic intrinsic noise sources are the $1/f$ noise (flicker noise) and the Johnson noise (thermal noise), as described previously in section 3.2.2. The high p_s of our Hall cross and EMR20 (see Table 3.9) increases total device resistance, which increases Johnson noise. This is reflected in the three orders-of-magnitude difference between the EMR20 PSD (10^{-13} V²/Hz) and the HCS1 PSD (10^{-16} V²/Hz) at 3 kHz for a current of 100 μ A. In the case of the Hall cross PSD (10^{-14} V²/Hz), the difference is two orders of magnitude at the same frequency and current.

Note that performing measurements under vacuum conditions decreases PSD by one order of magnitude compared to performing the measurements under ambient conditions. From our results, the Hall-cross PSD is 10^{-14} V²/Hz (see Table 3.6) at 3 kHz for a current of 1 μ A under vacuum conditions, while at ambient conditions the PSD is 10^{-15} V²/Hz (see Table 3.8) at the same frequency and current. However, the HCS1 PSD of 10^{-17} V²/Hz at 3 kHz for a current of 1 μ A differs by three orders of magnitude compared to the Hall-cross PSD at the same frequency and current under vacuum conditions.

Finally, the values presented in Table 3.10 enable one to project device response parameters for the Hall-cross and the EMR20 devices in the absence of significant hysteresis. The minimum n_s correspond to the maximum μ and S_I for all the currents, as seen in Table 3.8. The resulting Hall-cross B_{min} for a current of 100 μ A is 14.5% smaller compared to the Hall-cross B_{min} given in Table 3.9 at the same current. Similarly, the resulting EMR20 B_{min} is 22.8% compared to the EMR20 B_{min} of Table 3.9. However, as was discussed, the EMR20 data at 100 μ A are not accurate. In contrast, with an injection current of 10 μ A, the difference is only 2%. Therefore, we confirm that suppressing the hysteresis observed in the experimental results provides a more accurate estimation of intrinsic graphene properties.

Table 3.10. Extrapolated values assuming no significant hysteresis on the Hall-cross device.

	P_s ($\Omega \mu\text{m}$)	n_s (cm^{-2})	μ (cm^2/Vs)	B (mT)	I_b (μA)	S_I (V/AT)	B_{min} ($\text{T}/\sqrt{\text{Hz}}$)	f (kHz)
Ambient conditions								
Hall cross		2.4×10^{11}	150,000		1	2,880	11^{-6}	
	2.78^3	2.2×10^{11}	184,500	± 50	10	3,370	2.7^{-6}	3
		2.8×10^{11}	137,700		100	2,520	512^{-9}	
EMR20		3.1×10^{11}	147,000		1	2,130	42.8^{-6}	
	2.34^3	3.7×10^{11}	107,000	± 50	10	1,700	2.4^{-6}	3
		6.1×10^{11}	82,000		100	1,030	4.4^{-6}	

EMR20, this work trilayer EMR, gate voltage sweeps from -20 V to 20 V

The noise measurements for the EMR1 and EMR2 devices are presented in Appendix E and the obtained values given in Table 3.9. Both devices attain a sensitivity in the μT level with a current sensitivity (S_I) that is one order of magnitude smaller compared to the HCS1, the Hall cross, and the EMR20. The capping of graphene to protect it from environmental conditions is expected to enhance the performance of CVD-graphene EMR devices. Towards this end, the CVD graphene can be encapsulated using CVD-grown h-BN [90] employing the methodology described in Appendix A. The advantages are: i) reduction of p_s by nine orders of magnitude by employing an edge contact; ii) the enhancement of graphene μ , n_s , S_I , and S_V by one order of magnitude, employing h-BN as support material; iii) improvement of B_{min} by having high mobilities and low carrier densities.

4. FINITE ELEMENT MODELING (FEM) OF GRAPHENE-BASED MAGNETOMETERS

This chapter presents a finite element modeling (FEM) model of graphene-based magnetometers. The purpose of the FEM model is to develop a framework to study the behavior and performance of graphene-based devices as a function of material parameters, such as intrinsic properties, contact resistance, and device geometry. The FEM model is implemented in COMSOL Multiphysics® using its AC/DC module, which contains the physics that describes transport in the model. Simulation and experimental results of the fabricated Hall cross are compared under vacuum and ambient conditions as a benchmark. For the EMR device, experimental results under ambient conditions are used for benchmarking. An agreement is essential to provide confidence in the numerical simulations in order to expand the model for predictive optimization of the magnetometers. The results discussed focus on carrier density (n_s), carrier mobility (μ), and current sensitivity (S_I).

4.1 Hall-cross Model Definition

The model definition inputs the 2D geometry and material properties of the device into the COMSOL software. The Hall cross shown in Fig. 4.1(a) has dimensions corresponding to the fabricated device. The yellow regions are the metal contacts, while the grey area represents the h-BN/G/h-BN stack. The boundary conditions are defined by parameters such as contact resistance (ρ_s), the cross-sectional area through which the applied current (I_b) flows, a ground terminal for electric potential reference, and the magnetic field (B) applied perpendicular to the sensing area plane. Fig. 4.1(b) shows the location where I_b is applied (red line), the ground terminal (purple line), the points where potential difference (V_{diff}) (green and orange line) is acquired, and ρ_s (blue lines) as the boundary conditions employed. The mesh is the domain subdivision in small elements and is a critical parameter that impacts the precision of the simulation results. As described in Reference [91], the mesh needs to be finer near the current and voltage leads for accurate detection of the potential changes in these regions. The generated mesh of the Hall cross illustrated in Fig. 4.1(c) shows a refined and denser mesh in the contact leads.

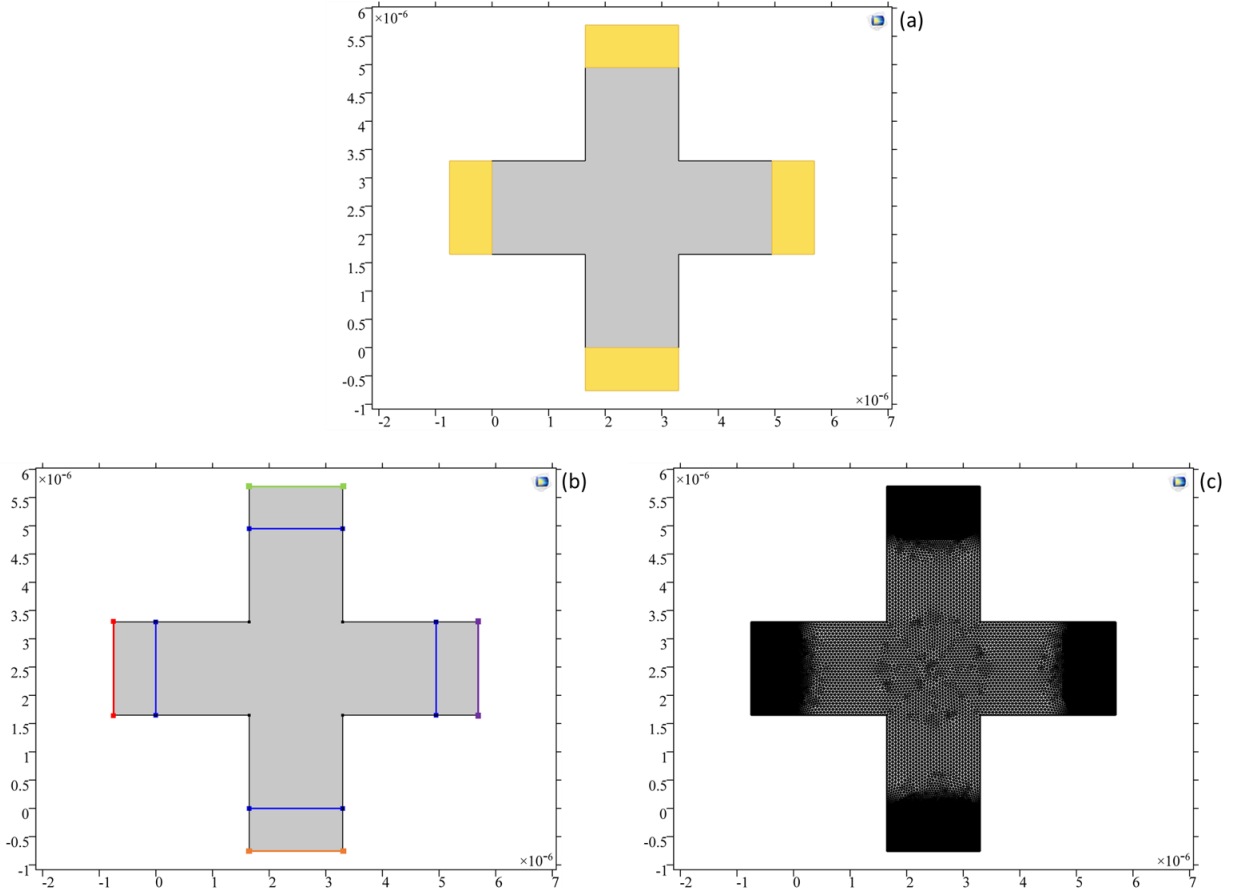


Fig. 4.1. FEM Hall cross model definition. (a) 2D geometry showing the h-BN/G/h-BN stack (grey) and the metal contacts (yellow). (b) Model boundary conditions: applied current (I_b) (red line), ground (purple line), contact resistance (p_s) (blue lines), acquired potential difference (V_{diff}) (green and orange line). (c) Mesh generated for the Hall cross.

The current flowing through the magnetometer and the voltage measured in the presence of a z-directed magnetic field (B) perpendicular to the sensing area is determined by

$$j = \sigma(B) E, \quad (4.1)$$

where j is the current density, E is the electric field, and $\sigma(B)$ is the conductivity matrix defined as

$$\sigma(B) = \frac{ne\mu}{1 + \mu^2 B^2} \begin{pmatrix} 1 & -\mu B & 0 \\ \mu B & 1 & 0 \\ 0 & 0 & 1 \end{pmatrix}, \quad (4.2)$$

where n is the carrier density, μ is the carrier mobility, and e is the electron charge. The Drude conductivity σ_0 when $B = 0$ T is given by

$$\sigma_0 = n\mu e. \quad (4.3)$$

The dimensionless magnetic field is given by

$$\beta = \mu B. \quad (4.4)$$

A moving electron charge q with a velocity v in the presence of an electric field E and magnetic field B experiences the Lorentz force given by

$$F = qE + qv \times B. \quad (4.5)$$

The EMR expresses the change of the resistance in the presence of a magnetic field (owing to the Lorentz force) compared to the resistance of the device in the absence of a magnetic field. The EMR expression is given by

$$EMR = \frac{R(B) - R(0)}{R_b}, \quad (4.6)$$

where

$$R(B) = \frac{V^+(B) - V^-(B)}{I_b} \quad (4.7)$$

is the nonlocal resistance and

$$R_b = \frac{V^+ - V^-}{I_b} \quad (4.8)$$

is the device current channel resistance when current I_b is injected through the current channel leads. The potential difference V_{diff} obtained is calculated from the following expression:

$$V_{diff} = V^+ - V^- = \int E \, dr. \quad (4.9)$$

The inputs to the FEM model for comparison of the simulation output with the experimental results are shown in Table 4.1. The experimental contact resistance (p_s), carrier density (n_s), and mobility (μ) previously calculated are the simulation inputs. For the vacuum conditions, two magnetic fields (B) of ± 50 mT and ± 5 T, and a current of $1 \mu\text{A}$ are employed as inputs as well. The input parameters for ambient-condition measurements are magnetic field of ± 50 mT and input currents of $1 \mu\text{A}$, $10 \mu\text{A}$, and $100 \mu\text{A}$. The model does not account for the gate voltage (V_g) dependence of the graphene conductivity. Therefore, the approach to employing the FEM model when considering (V_g) dependence is to use each calculated value of n_s and μ for each V_g value.

Table 4.1. FEM-model inputs to benchmark the simulations with experimental results. The derived values of n_s , μ , and p_s at different applied magnetic fields and currents are the inputs under vacuum and ambient conditions.

	P_s ($\Omega \cdot m^2$)	n_s (m^{-2})	μ (m^2/Vs)	B (T)	I_b (A)
Vacuum condition					
Dataset 1		2.53×10^{15}	7.8		
Dataset 2	9.45×10^{-13}	1.94×10^{15}	10.2	± 0.05	1×10^{-6}
Average		2.21×10^{15}	8.9		
Dataset 1	9.45×10^{-13}	3.22×10^{15}	6.1	± 5	$1 \times 10e^{-6}$
Ambient condition					
		2.44×10^{15} to 9.35×10^{16}	0.24 to 14.8		1×10^{-6}
Dataset 1	9.45×10^{-13}	2.24×10^{15} to 5.45×10^{17}	0.04 to 18.3	± 0.05	10×10^{-6}
		2.84×10^{15} to 1.77×10^{17}	0.12 to 13.6		100×10^{-6}

4.1.1 Benchmarking under vacuum conditions

The simulation output result of the surface electric potential (E) distribution through the device in the presence of a magnetic field (B) of -50 mT is shown in Fig. 4.2(a). The streamlines (black lines) show the current flow direction, whose trajectories are deflected towards the lower arm of the cross by the Lorentz force; see the direction of the small streamline peak. The surface E distribution with $B = 50$ mT displayed in Fig. 4.2(b) shows the current deflection towards the upper part of the device, streamline peak in the opposite direction, confirming the expected Hall-effect behavior. Fig. 4.2(c) shows the surface E distribution in the absence of a magnetic field. Here the flow of current is straight along with the Hall cross, and no streamline peak is seen.

The electrical potential (E) distribution along the arm orthogonal to the current flow is illustrated in Fig. 4.2(d). The plot shows the increment of the potential due to an applied magnetic field of 50 mT. For both polarities, the increment is the same because the model considers a symmetric Hall-cross-device.

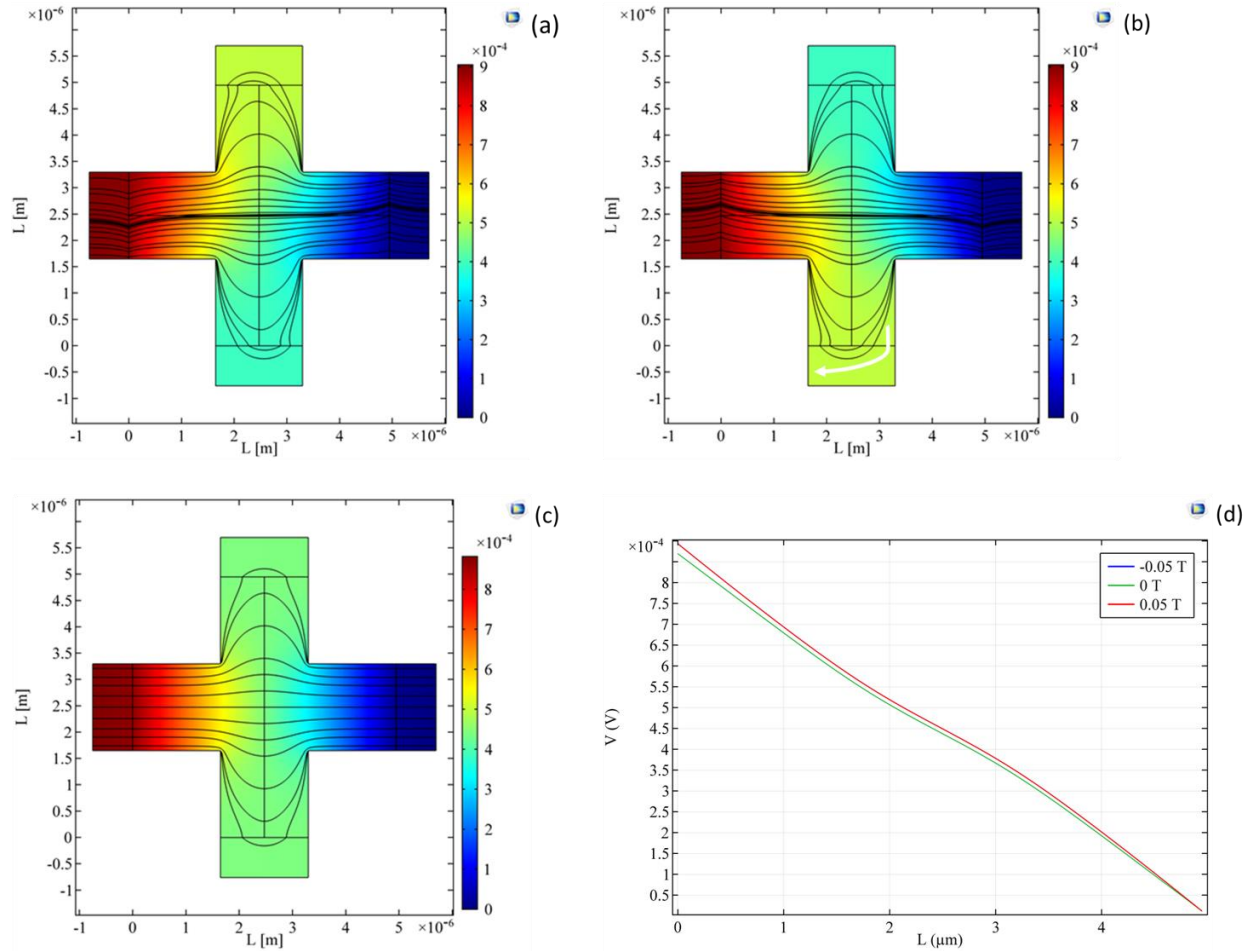


Fig. 4.2. FEM Hall simulations of the surface electric potential (E) distribution along the Hall cross arms in the presence of external fields perpendicular to the plane of the figure of: (a) -50 mT, (b) 50 mT, and (c) 0 mT. Current flow direction streamlines (black lines). (d) Electric Potential (E) distribution along the arm orthogonal to the current flow. Applied current, 1 μA .

The simulated magnetic response of the Hall cross at RT shows a linear change of the voltage (V) as a function of the magnetic field (B), as seen in Fig. 4.3(a). The plot obtained across the transversal direction shows no offset at zero magnetic fields since the electric contacts are symmetric. The slope value sign agrees with the experimental data, indicating p-type carrier charges. The carrier density (n_s) and mobility (μ) are determined as described in the experimental section. The obtained values are $n_s = 2.64 \times 10^{11} \text{ cm}^{-2}$ and $\mu = 75,000 \text{ cm}^2/\text{Vs}$. Similarly, the current sensitivity (S_I) is calculated and gives a value of $S_I = 2,366 \text{ V/AT}$. Fig. 4.3(b) shows V as a function of B along the longitudinal direction. A parabolic behavior is observed and at $\pm 50 \text{ mT}$, the voltage value is $240 \mu\text{V}$.

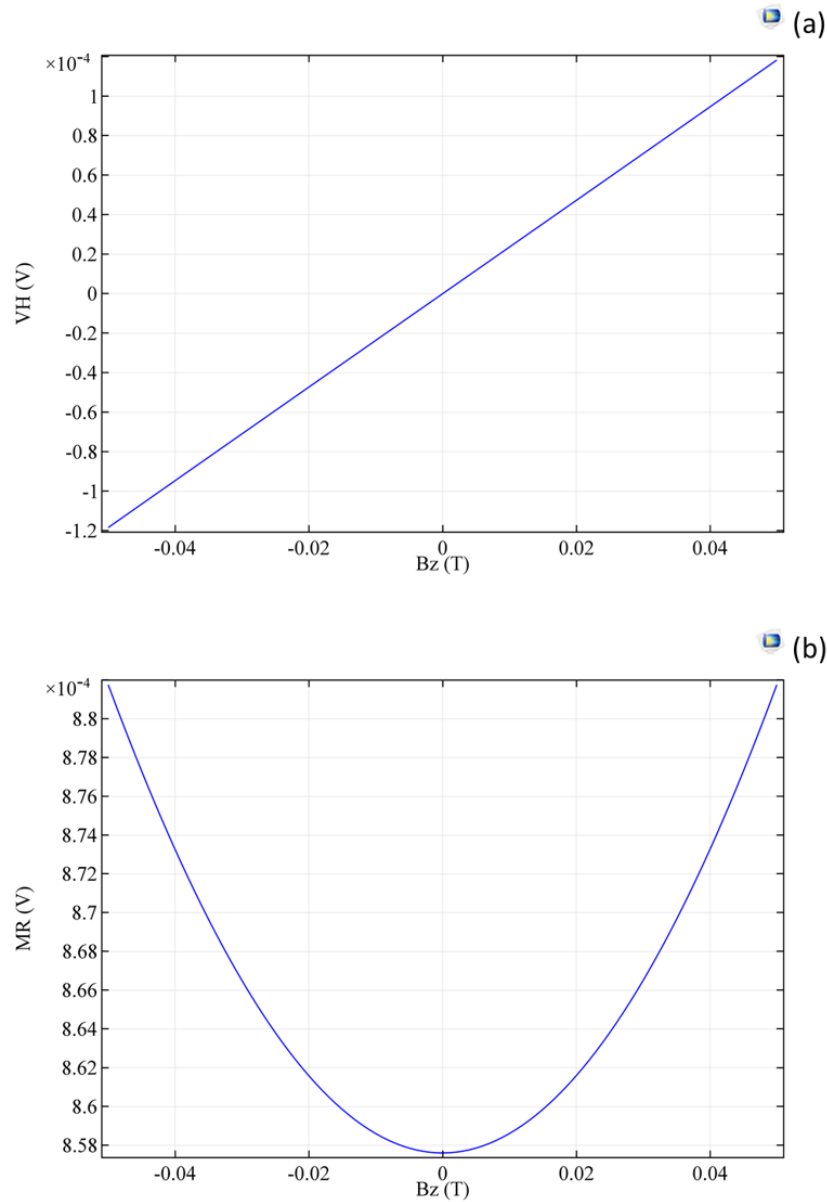


Fig. 4.3. Simulation of the magnetic response of the Hall cross under vacuum conditions at RT. (a) Longitudinal direction V as a function of B . (b) Transversal direction V as a function of B . Applied current $1 \mu\text{A}$ and magnetic field $\pm 50 \text{ mT}$.

The comparison between simulations and experimental results for the Hall-cross device is presented in Fig. 4.4(a-c). The experimental dataset 1 (blue line) and the simulated voltage (V) (red line) are plotted vs. applied magnetic field (B). Both show a linear dependency and differ by an offset of $890 \mu\text{V}$. In addition, the total $\Delta R/\Delta B$ is 249Ω for the experimental data and 240Ω for the simulation data, indicating excellent agreement between the computational model and experiments.

The comparison of V vs. B dependence using experimental dataset 2 shows the same behavior as dataset 1, but the offset difference is $540 \mu\text{V}$; see Fig. 4.4(b). Here, the total $\Delta R/\Delta B$ is 323Ω and 308Ω for the experimental and simulation data, respectively. Using the experimental voltage curve, n_s , μ , and S_I are extracted as described previously and the obtained values are $n_s = 1.94 \times 10^{11} \text{ cm}^{-2}$, $\mu = 102,000 \text{ cm}^2/\text{Vs}$, and $S_I = 3,250 \text{ V/AT}$. Similarly, from the simulated voltage curve, the inferred values are $n_s = 2.02 \times 10^{11} \text{ cm}^{-2}$, $\mu = 98,000 \text{ cm}^2/\text{Vs}$, and $S_I = 3,089 \text{ V/AT}$.

Finally, dataset 1 (blue line), dataset 2 (black line), and simulated average of the datasets (red line) graphs of V as a function of B are displayed in Fig. 4.4(c). The plots show a difference of 44.8 %, at -50 mT and of 2.3 % at 50 mT between datasets 1 & 2. Using the simulated average voltage plot, the obtained values of n_s , μ , and S_I are $2.30 \times 10^{11} \text{ cm}^{-2}$, $86,000 \text{ cm}^2/\text{Vs}$, and $2,710 \text{ V/AT}$, respectively. These numbers fall in between the experimental range of dataset 1 and dataset 2.

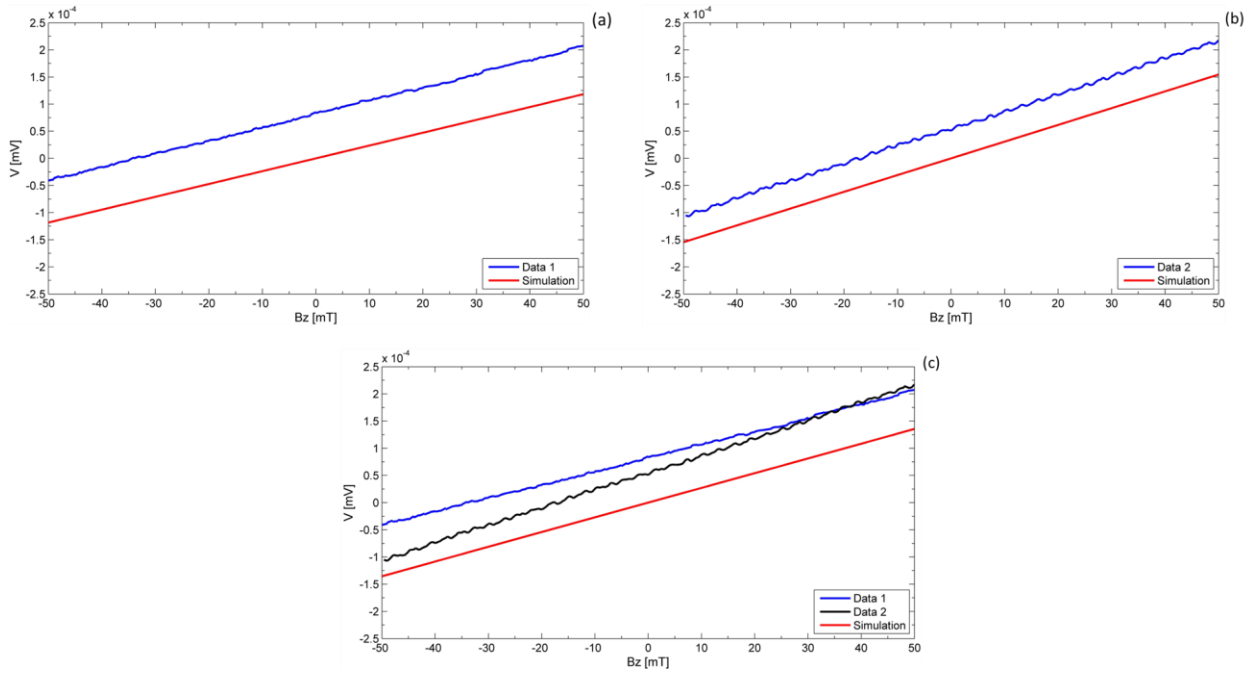


Fig. 4.4. FEM results comparison with of experimental data at RT under vacuum conditions. V vs of B of (a) dataset 1, (b) dataset 2 and (c) simulated average. Applied current, $1 \mu\text{A}$ and magnetic field, $\pm 50 \text{ mT}$. Dataset values are given in Table 4.1

The simulation results for the surface electric potential (E) distribution under applied magnetic fields of ± 5 T are shown in Fig. 4.5(a) and 4.5(b). Significant deflections of the current paths (see the streamline peaks at the upper and lower arms) are readily observed. The electrical potential (E) distribution along the arm orthogonal to the current flow (see Fig. 4.5(c)) shows that the potential increments by one order of magnitude at ± 5 T.

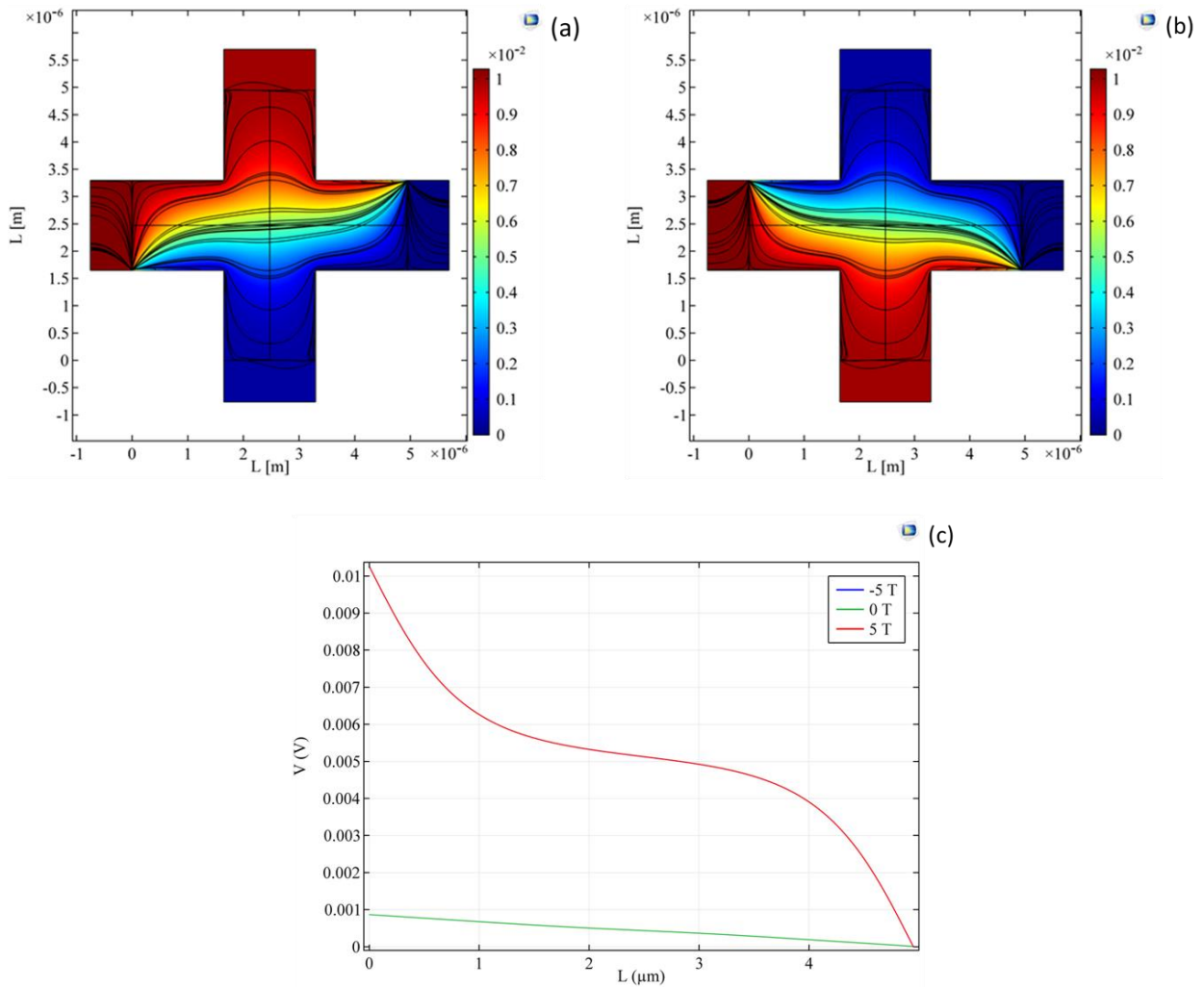


Fig. 4.5. FEM Hall simulations of the surface electric potential (E) distribution along the Hall cross arms in the presence of external fields perpendicular to the plane of the figure of: (a) -5 T and (b) 5 T. (a-b) Current flow direction streamlines (black lines). (d) Electric Potential (E) distribution along the arm orthogonal to the current flow. Applied current, 1 μ A.

The simulated magnetic response of the Hall-cross device vs. magnetic field sweep from -5 T to 5 T is presented in Fig. 4.6(a-b). The (V) vs. magnetic field (B) measured along the transversal direction of the current input shows a linear change of V , as shown in Fig. 4.6(a). The slope of the voltage curve is used to calculate values of carrier density (n_s) and mobility (μ): $n_s = 3.23 \times 10^{11} \text{ cm}^{-2}$ and $\mu = 61,260 \text{ cm}^2/\text{Vs}$. The current sensitivity (S_I) is also derived and gives $S_I = 1,927 \text{ V/AT}$. This differs from the experimental S_I by 31.1 % ($S_I = 986 \text{ V/AT}$) at -5 T and by 3.4 % ($S_I = 1,754 \text{ V/AT}$) at 5 T. The (V) vs. magnetic field (B) measured along the current path is shown in Fig. 4.6(b). A sharp parabolic response is observed, and the maximum voltages of 90 mV are obtained at ± 5 T.

Comparison of the simulated results with experiment in response to the applied magnetic field is displayed in Fig. 4.6(c). The plot shows a noticeable difference between the experimental (blue line) and the simulation (red line) data. The simulated response exhibits no saturation. Thus, the predicted value of $\Delta R/\Delta B$ is $10,000 \text{ } \Omega$ for ± 5 T, while the experimental values of $\Delta R/\Delta B$ are $4,500 \text{ } \Omega$ and $8,500 \text{ } \Omega$ for -5T and 5T , respectively. The differences between simulated and measured $\Delta R/\Delta B$ values are 37.9 % for -5 T and 8.1 % for 5 T.

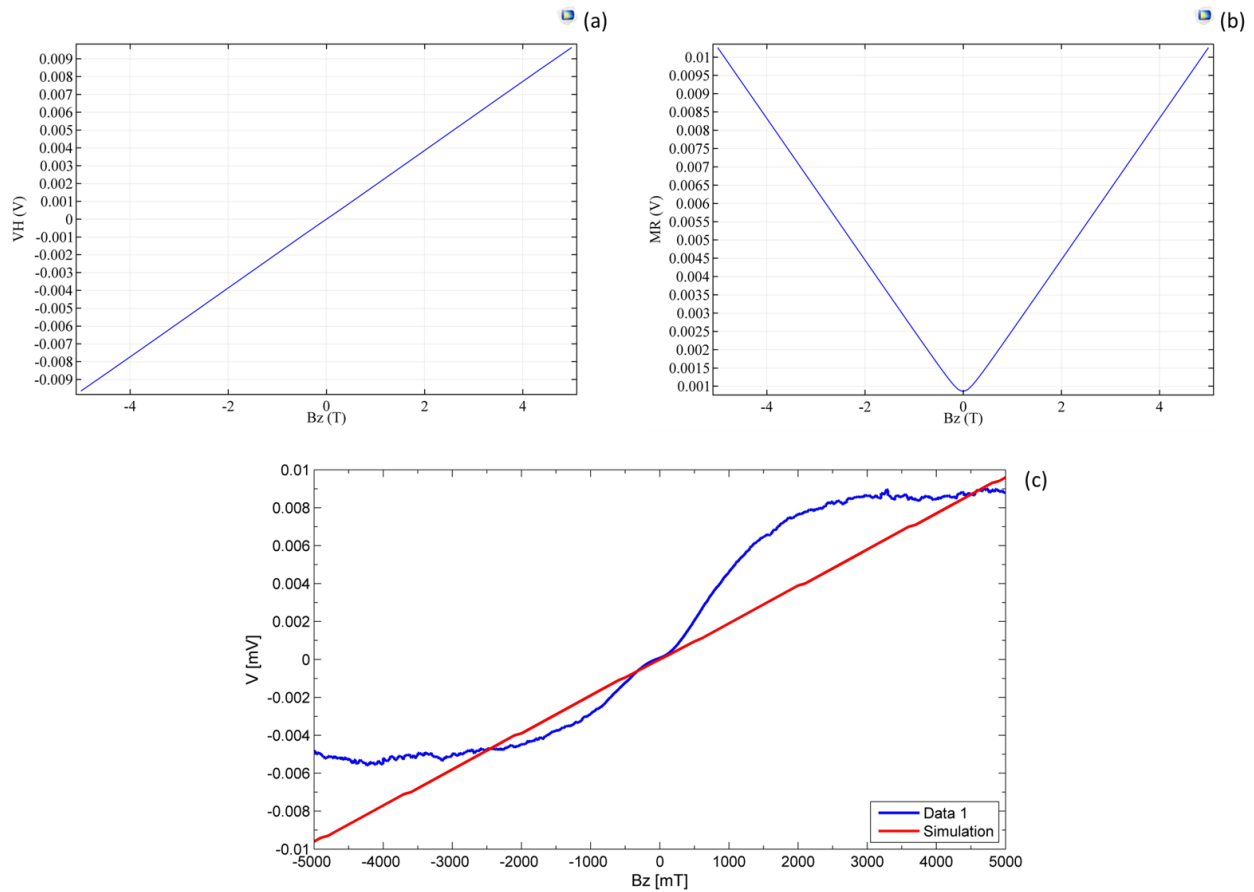


Fig. 4.6. FEM Hall simulations of voltage vs. applied magnetic field for: (a) field measured perpendicular to the injected current path and (b) along the current path. (c) Comparison between simulation and experiment of V vs. B measured perpendicular to the current path.

4.1.2 Comparison of model and experimental results for measurements done in ambient conditions

Experimental and simulation results for the device response signal (V) vs. gate voltage (V_g) for an injection current of $1 \mu\text{A}$ under magnetic fields (B) of 0 and ± 50 mT are shown in Fig. 4.7(a). The plot shows that when experimental values for carrier density (n_s) and mobility (μ) are used as input in the simulations, the computed plots do not resemble the experimental trends. The reason is that the voltage curves are symmetric in both voltage regimens of the gate voltage, but the simulation does not present hysteresis.

The slope values of the three data sets at $B = -50$ mT, $B = 0$ mT, and $B = 50$ mT are used to calculate n_s . Then, using the derived value of n_s and the sheet resistance (R_s) from Fig. 3.13, μ is

extracted. Fig. 4.7(b) displays a plot μ vs. n_s , that provides the difference between computed and experimental results. The maximum value of μ and its corresponding n_s differs by 1.8 %.

The voltage plots are employed to calculate the current sensitivity (S_I) as described previously. The S_I vs. V_g in Fig. 4.7(c) shows that the simulation follows the experimental trend. However, the simulated value of S_I is smaller than the experimental. The difference between the maximum peak of the sensitivity at the positive field (V_{H+} , blue line) and the negative field (V_{H-} , red line) is 7.8 % and 1.9 %, respectively. Another difference is the position of the minimum value of S_I , which corresponds to CNP location. The minimum value of the simulated S_I is in $V_g = 0.1$ V, while the experimental S_I of V_{H+} is in $V_g = 0.8$ V and the S_I of V_{H-} is in $V_g = -0.5$ V. This shows that the simulated S_I behavior falls within experimental S_I values, as observed in Fig. 4.7(c).

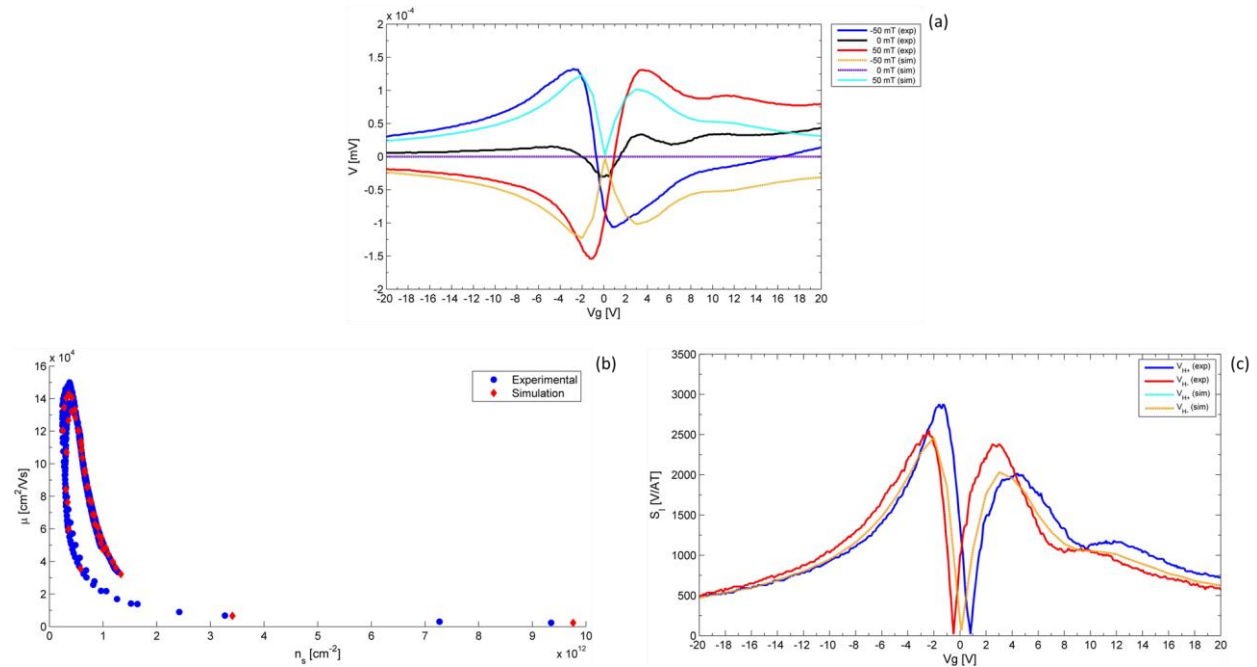


Fig. 4.7. Comparison of FEM results with experiments: (a) V vs. V_g as a function of applied magnetic field: $B = -50$ mT, 0 mT, and 50 mT (blue, black, and red lines); simulation $B = -50$ mT, 0 mT, and 50 mT (orange, purple, and cyan line). (b) μ vs. n_s : experimental data (blue circles) and simulation data (red diamonds). (c) Absolute S_I vs. V_g . Experimental data (blue and red lines) and simulation data (cyan and orange lines). Applied current, 1 μ A.

The voltage (V) dependence on gate voltage (V_g) for an injection current of 10 μA with applied magnetic fields 0 and ± 50 mT is shown in Appendix F (Fig. F.1(a)). The plot shows that the simulation data follow the trend of the experimental results. The experimental data are asymmetric at the positive polarity of V_g . The carrier density (n_s), mobility (μ), and current sensitivity (S_I) are derived as previously described. The μ vs. n_s plot shown in Fig. F.1(b) indicates a difference between the experimental and simulated μ and n_s of 1.8 %.

The simulated S_I vs. V_g plot follows the experimental tendency as well; see Fig. F.1(c). Here, the difference between the simulated and experimental S_I is 11.4 % for V_{H+} (blue line) and 6.2 % for V_{H-} (red line) at the maximum peak of S_I . Furthermore, the simulated CNP position when S_I is at its minimum is at $V_g = 1$ V, whereas the experimental S_I of V_{H+} and the S_I of V_{H-} are in $V_g = 1.5$ V and $V_g = 0.3$ V, respectively. For this current, S_I also falls in between the experimental S_I s.

The plot displayed in Fig. F.2(a) shows the voltage for an injection current of 100 μA with applied magnetic fields of 0 and ± 50 mT. Here, the experimental and simulated data from the positive polarity of B overlap, while the negative polarity shows a small difference between them at the negative range of V_g . On the other hand, for positive values of V_g the experimental and computational results show large differences. Fig. F.2(b) shows μ vs. n_s ; the difference between experimental and simulation maximum values is 1.9 %.

The simulated S_I as a function of V_g shown in Fig. F.2(c) shows an overlap of the curves in the positive range of V_g , whereas the negative V_g presents a significant difference. The experimental and simulated maximum peak of S_I observed differ by 1.7 % and 8.9 % for V_{H+} (blue line) and V_{H-} (red line), respectively. It is also seen that the experimental and simulated CNP position almost overlap. The minimum S_I is at $V_g = 0.7$ V for the simulation data. For the experimental data, the minimum S_I is at $V_g = 0.6$ V for V_{H+} and at $V_g = 0.8$ V for V_{H-} .

4.1.3 Modeling results for attaining Hall-cross devices with pT sensitivity

The agreement with experimental results gives confidence in the model to be employed for predictive design to increment device magnetic sensitivity. Towards this end, the FEM model is used to estimate the intrinsic graphene parameters and the contact resistance required to attain pT sensitivity. First, the parameters mentioned in section 1.8 are used to predict the Hall-cross magnetic response with carrier density (n_s), mobility (μ), and contact resistance (p_s) that have

been reported in the literature. Second, target values of these parameters are also considered for further sensitivity enhancement.

The predicted magnetic response at an injection current of 100 μA is shown in Fig. 4.8(a). This response corresponds to a Hall-cross device with a $n_s = 1.3 \times 10^{11} \text{ cm}^{-2}$, $\mu = 180,000 \text{ cm}^2/\text{Vs}$, and $p_s = 150 \text{ } \Omega \text{ } \mu\text{m}$. The simulated device has the same dimensions as the one fabricated in this work. The voltage (V) vs. magnetic field (B) dependence shows the expected linear response. From the curve, a current sensitivity (S_I) of 4,633 V/AT is computed. Next, the experimentally obtained PSD is replaced with a theoretical estimation of the Johnson noise power spectral density. This is derived by employing the following equation: $V_n^2 = 4k_bTR$ where k_b is the Boltzmann constant, T is the temperature in Kelvin, and R is the total device resistance. The latter is calculated using Equation (3.19). The derived Johnson PSD is $V_n^2 = 9.77 \times 10^{-19} \text{ V}^2/\text{Hz}$, which gives a magnetic resolution (B_{min}) of 2.1 nT/ $\sqrt{\text{Hz}}$.

A Hall-cross device with $n_s = 1.66 \times 10^{10} \text{ cm}^{-2}$, $\mu = 245,000 \text{ cm}^2/\text{Vs}$, and $p_s = 30 \text{ } \Omega \text{ } \mu\text{m}$ (from Reference [76]) gives the magnetic response shown in Fig. 4.8(b) for a current of 100 μA . The V vs. B response is one order of magnitude higher than the response shown Fig. 4.8(a). The S_I is calculated from the voltage curve and gives 37,744 V/AT. Next, the Johnson PSD is inferred to be $V_n^2 = 5.81 \times 10^{-18} \text{ V}^2/\text{Hz}$ and the derived B_{min} is 639 pT/ $\sqrt{\text{Hz}}$. These results indicate that significant improvements on carrier mobility and density together with suppression of contact resistance is a viable path towards pT sensitivity at RT. If we consider the possibility of cooling the device, higher sensitivities could be attained. For example, as previously stated at 60K mobilities up to 1,000,000 cm^2/Vs have been reported in graphene flakes partially decoupled from the surface of bulk graphite [52], and in suspended-graphene devices [53]. Furthermore, the same mobility at a carrier density of $\sim 3 \times 10^{12} \text{ cm}^{-2}$ is attained in h-BN/graphene/h-BN trilayers at 20K [48].

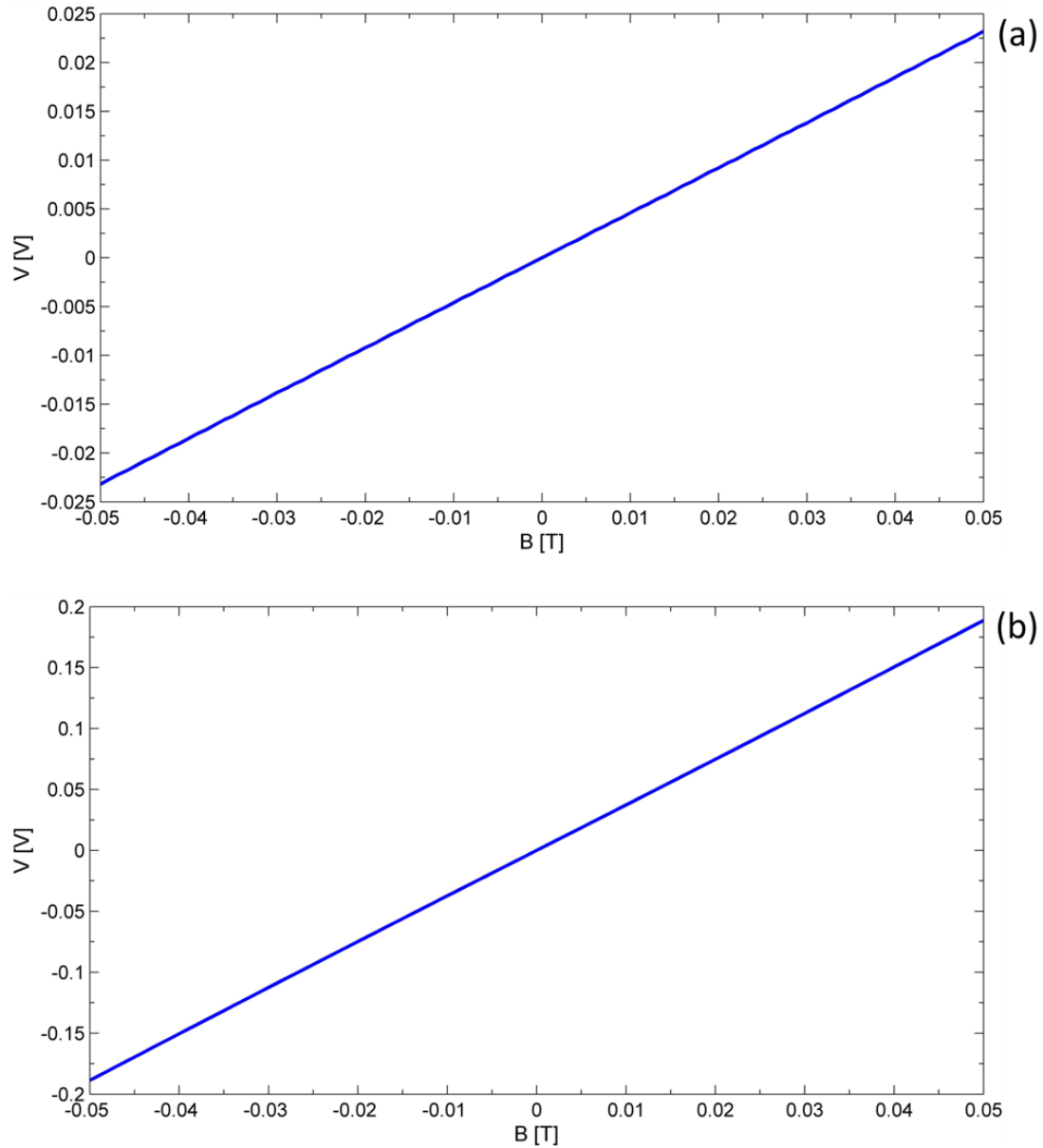


Fig. 4.8. Simulation magnetic response of the Hall cross-device at RT to predict the pT sensitivity. V as function of B for (a) $n_s = 1.3 \times 10^{11} \text{ cm}^{-2}$, $\mu = 180,000 \text{ cm}^2/\text{Vs}$, and $p_s = 150 \text{ } \Omega \text{ } \mu\text{m}$ and for (b) $n_s = 1.66 \times 10^{10} \text{ cm}^{-2}$, $\mu = 245,000 \text{ cm}^2/\text{Vs}$, and $p_s = 30 \text{ } \Omega \text{ } \mu\text{m}$. Applied current, $100 \text{ } \mu\text{A}$ and magnetic field, $\pm 50 \text{ mT}$.

4.2 EMR Magnetometer Modeling

A FEM model of an EMR graphene-h-BN magnetometer that resembles the one from Reference [1] is employed to benchmark experimental results under ambient conditions. The schematic EMR device shown in Fig. 4.9(a) is representative of the fabricated EMR device described in section 2.2.2. The graphene encapsulated in h-BN is shown in grey, the metallic shunt (area of $6 \mu\text{m} \times 1.5 \mu\text{m}$) and the metal contacts in yellow. The total size of the sensor is $8 \mu\text{m} \times 4 \mu\text{m}$ and the sensing area is $4.5 \mu\text{m} \times 1.6 \mu\text{m}$, delineated by the cyan dashed lines. The boundary conditions illustrated in Fig. 4.9(b) show the electric lead configuration I^+ , V^+ , I^- , V^- . Current is applied in the I^+ lead (red line) and exits through the I^- lead (purple line), the potential difference is acquired from the V^+ and V^- leads (green and orange line, respectively), and the regions contributing to the contact resistance (p_s) are shown with blue lines. Finally, the model mesh displayed in Fig. 4.9(c) shows a refined and denser mesh in the contacts and shunt for better accuracy and precision of the simulation results.

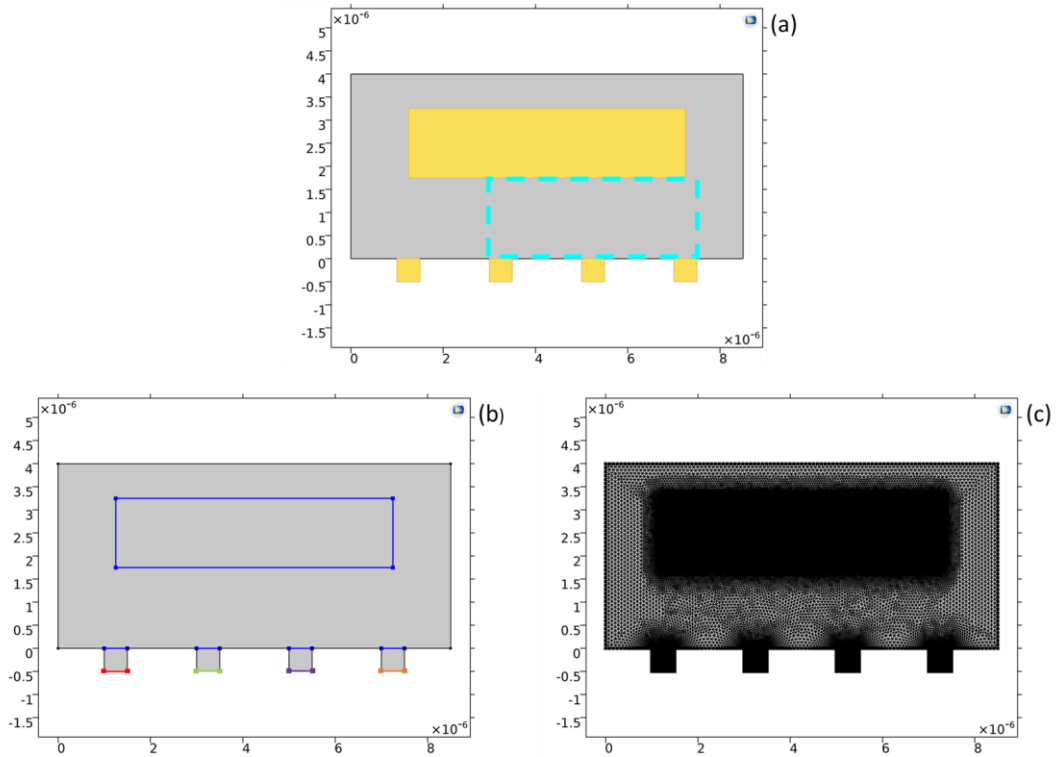


Fig. 4.9. Schematics of FEM modeling of the EMR graphene-hBN magnetometer. (a) 2D geometry, h-BN/G/h-BN (grey), metallic shunt and metal contacts (yellow), and sensing area (cyan). (b) Model boundary conditions: applied current (I_b) (red line), ground (purple line), contact resistance (p_s) (blue lines), potential difference (V_{diff}) (green and orange lines). (c) Mesh employed for the EMR device simulation.

The input parameters for the EMR-device FEM simulation are given in Table. 4.2. As described in section 4.1, the carrier density (n_s) and mobility (μ) derived for each value of the applied gate voltage are the simulation inputs. A current of 100 μ A and a magnetic field of ± 50 mT are used as experimental parameters.

Table 4.2. EMR device parameters employed for the FEM model simulation and comparison with experimental results

P_s ($\Omega \cdot m^2$)	n_s (m^{-2})	μ (m^2/Vs)	B (T)	I_b (A)
7.97×10^{-13}	6.11×10^{15} to 1.63×10^{18}	0.03 to 12.3	± 0.05	100×10^{-6}

A comparison of simulation and experimental results is presented in Fig. 4.10(a-c). The computed voltage (V) vs. gate voltage (V_g) dependence follows the trend of the experimental results; see Fig. 4.10(a). However, the simulated voltage magnitude is smaller than the measured experimental values.

The carrier density (n_s) and mobility (μ) are calculated as previously described in section 4.1.2 and plotted in Fig. 4.10(b). The μ as a function of n_s shows that the maximum value of μ and its corresponding n_s differs by 11.5% between experimental and simulation data. The current sensitivity (S_I) as a function of gate voltage (V_g) illustrated in Fig. 4.10(c) shows the simulation follows the trend of the experimental results with symmetry at the CNP location, but the significant difference is at the maximum peaks of S_I . This is related to the differences in the voltage response shown in Fig. 4.10(a).

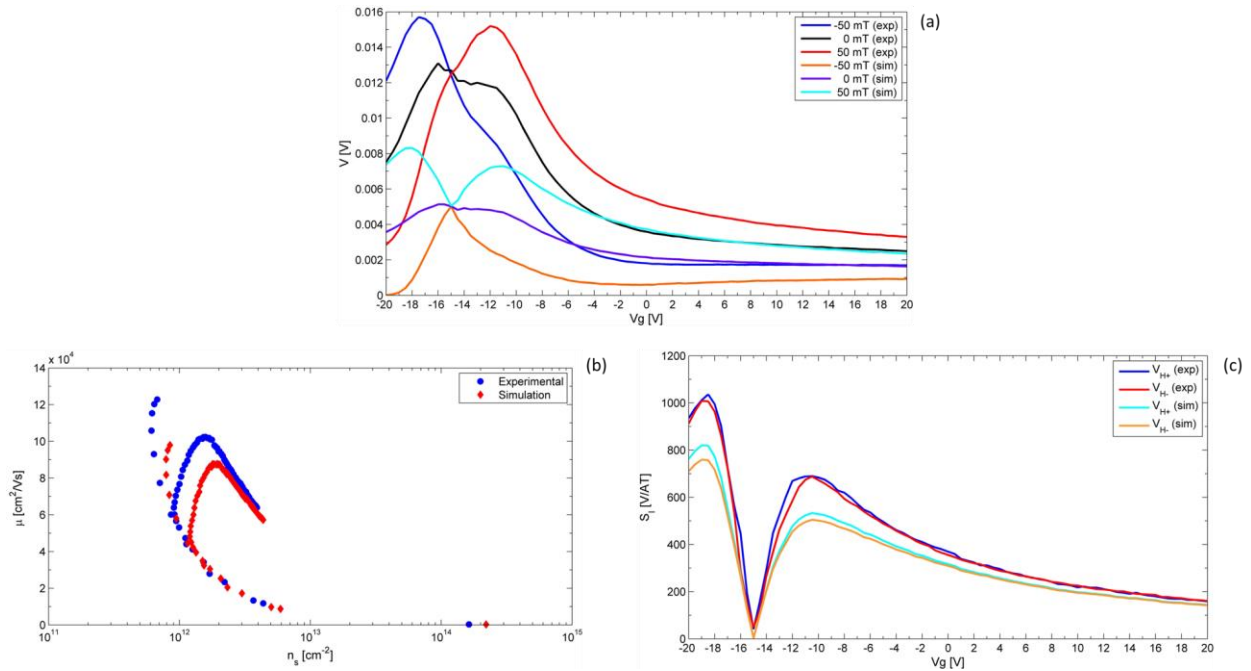


Fig. 4.10. Comparison of FEM results with experiments: (a) V vs. V_g as a function of applied magnetic field: $B = -50$ mT, 0 mT, and 50 mT (blue, black, and red lines). Simulation results $B = -50$ mT, 0 mT, and 50 mT (orange, purple, and cyan lines). (b) μ as a function of n_s . Experimental data (blue circles) and simulation data (red diamonds). (c) S_I vs. of V_g . Experimental data (blue and red lines) and simulation data (cyan and orange lines). Applied current, 100 μ A.

4.2.1 Modeling results for attaining EMR devices with pT sensitivity

The FEM modeling results agree with experimental measurements to within 11.5%, and the model can be employed for optimizing the design of EMR sensors to realize pT sensitivity. The approach used to predict pT sensitivity in section 4.1.3 is repeated here. The EMR magnetometer with $n_s \sim 1.3 \times 10^{11} \text{ cm}^{-2}$, $\mu \sim 180,000 \text{ cm}^2/\text{Vs}$, and $p_s = 150 \text{ } \Omega \text{ } \mu\text{m}$ simulation results for a current of 100 μ A is shown in Fig. 4.11(a-c).

The surface electric potential (E) in the absence of a magnetic field (B) is illustrated in Fig. 4.11(c). The streamlines show the path of the current flow in the presence of a -50 mT field in Fig. 4.11(a). The current paths deflect towards the right side of the magnetometer owing to the Lorentz force. The path traveled by charge carriers to exit the system is shorter, which decreases E , as shown in Fig. 4.11(a). Under the influence of a 50-mT field, the direction of the current

path is deflected towards the left side of the magnetometer. Here, the path the charge carrier traveled to exit the system is longer, making a significant increment in E , as seen in Fig. 4.11(b).

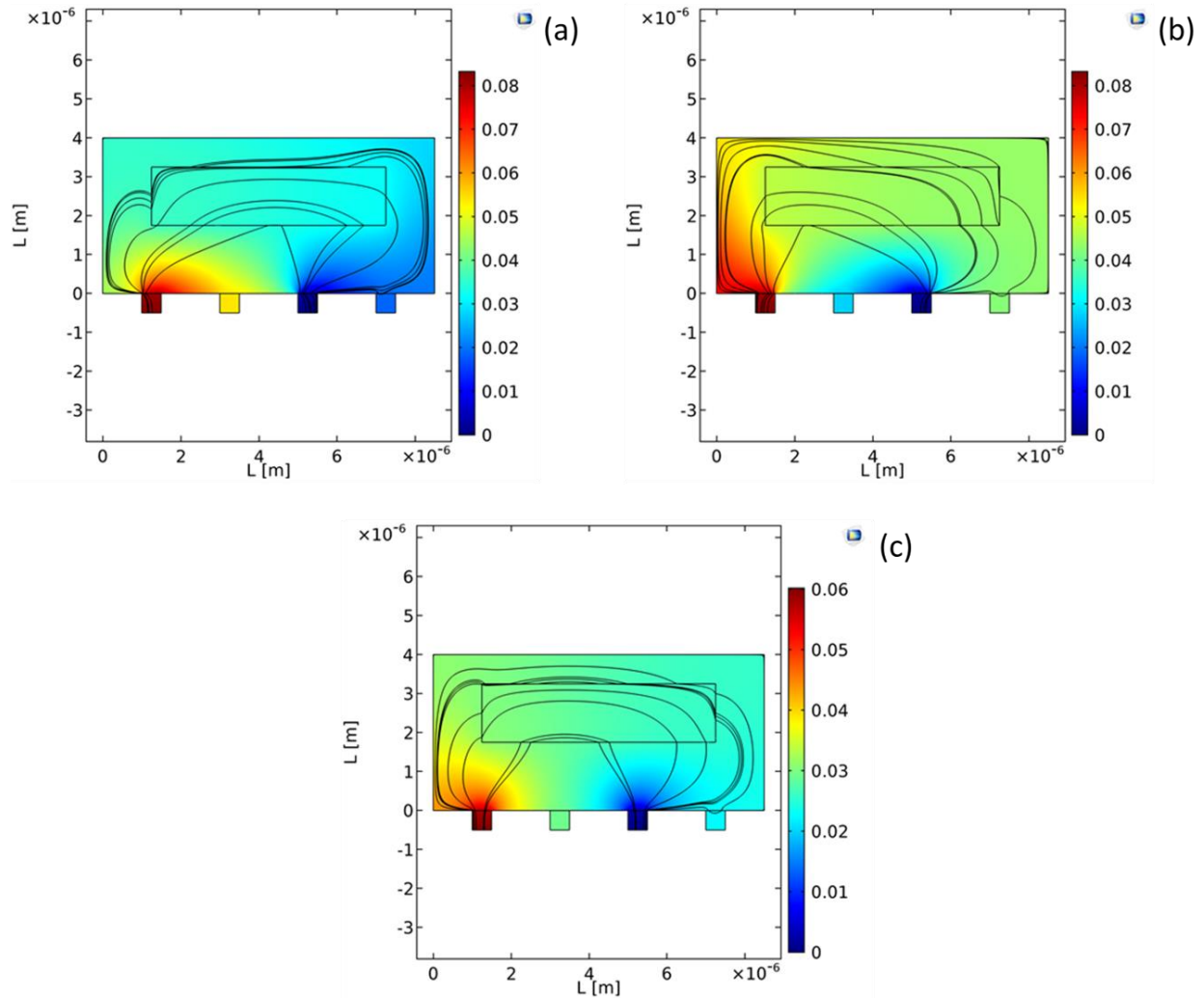


Fig. 4.11. FEM simulation of surface potentials and current paths for an EMR magnetometer with $n_s \sim 1.3 \times 10^{11} \text{ cm}^{-2}$, $\mu \sim 180,000 \text{ cm}^2/\text{Vs}$, and $p_s = 150 \text{ } \Omega \text{ } \mu\text{m}$. Surface electric potential (E) distribution along with the device at (a) $B = -50 \text{ mT}$, (b) $B = 50 \text{ mT}$, and (c) $B = 0 \text{ mT}$. (a-c) Streamlines showing the current flow path direction (black lines).

The voltage (V) response vs magnetic field (B) shown in Fig 4.12(a) indicates that the EMR magnetometer response is higher than that of the Hall device having the same mobility ($\mu = 180,000 \text{ cm}^2/\text{Vs}$). From these results, the current sensitivity (S_I) is calculated to be 5,773 V/AT at 50 mT and 4,287 V/AT at -50 mT. The calculated Johnson PSD and magnetic resolution (B_{min}) are $V_n^2 = 1.14 \times 10^{-18} \text{ V}^2/\text{Hz}$ and $B_{min} = 1.9 \text{ nT}/\sqrt{\text{Hz}}$. The equivalent response for an EMR

magnetometer with $n_s = 1.66 \times 10^{10} \text{ cm}^{-2}$, $\mu = 245,000 \text{ cm}^2/\text{Vs}$, and $p_s = 30 \text{ } \Omega \text{ } \mu\text{m}$ with the same injected current is presented in Fig. 4.12(b). The V response is one order of magnitude higher than that of the lower mobility case. The estimated (S_I) 47,332 V/AT and 32,132 V/AT at 50 mT and -50 mT, respectively. Finally, V_n^2 , and B_{min} are inferred and the obtained values are $4.4 \times 10^{-18} \text{ V}^2/\text{Hz}$ and $443 \text{ pT}/\sqrt{\text{Hz}}$.

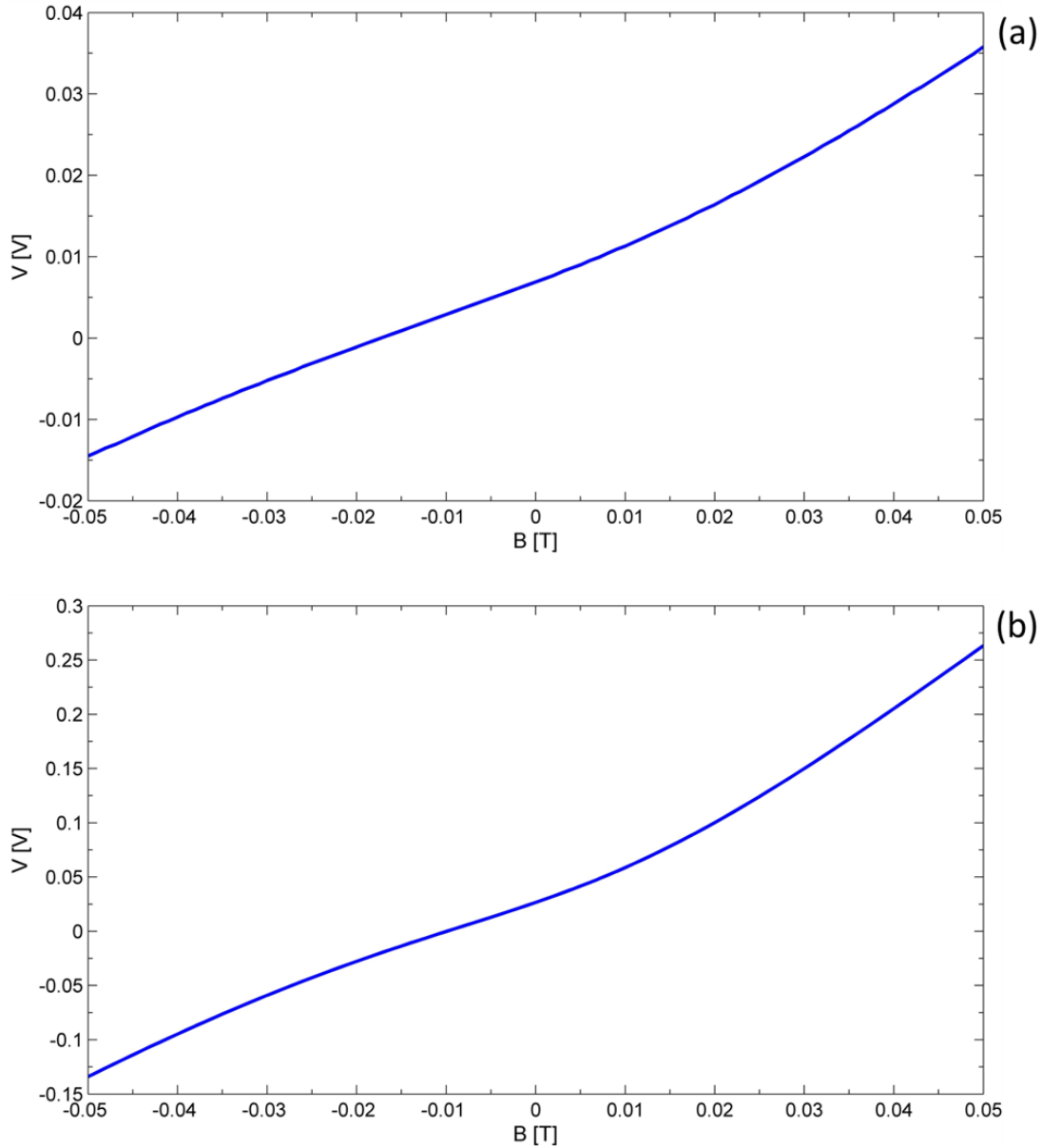


Fig. 4.12. Simulation of the magnetic response of an EMR device at with (a) $n_s = 1.3 \times 10^{11} \text{ cm}^{-2}$, $\mu = 180,000 \text{ cm}^2/\text{Vs}$, and $p_s = 150 \text{ } \Omega \text{ } \mu\text{m}$ and for (b) $n_s = 1.66 \times 10^{10} \text{ cm}^{-2}$, $\mu = 245,000 \text{ cm}^2/\text{Vs}$, and $p_s = 30 \text{ } \Omega \text{ } \mu\text{m}$. Applied current, $100 \text{ } \mu\text{A}$.

4.3 Discussion

Experimental and simulation results are presented in Table 4.4. The agreement between results have a percentage error less than 3%. Therefore, the developed FEM model simulates with high precision the experimental performance of Hall-cross magnetometers. By including the gate-voltage dependency, the model permits tuning the graphene sheet resistance. This is an important design parameter for signal-to-noise optimization. The model was also applied to predict the response of graphene-based magnetometers having optimum carrier density and mobility. Said model application indicates that a Hall cross employing graphene with a carrier mobility of 180,000 cm²/Vs and a carrier density of 1.3×10¹¹ cm⁻² can attain a sensitivity of 2.1 nT/√Hz. These values for mobility and carrier density have been reported in the literature. If the mobility can be incremented to 245,000 cm²/Vs and the carrier density decreased to 1.6×10¹⁰ cm⁻², the device would provide a sensitivity of 639 pT/√Hz. We note that Gopinadhan et al. [92] reported intrinsic graphene carrier density of the order of 10¹⁰ – 10¹¹ cm⁻² at the CNP. Regarding the mobility required, as noted earlier, at 60K a mobility of up to 1,000,000 cm²/Vs has been reported in graphene supported on bulk graphite and in suspended-graphene devices [52], [53]. The same mobility is reported in trilayer devices at 20K [48]. We expect similar values attainable at 77K, a readily available cryogenic temperature (using liquid nitrogen).

The experimental measurement for fields (B) of ±5 T presented a significant difference compared with simulation results. The physical mechanisms for nonlinear response over these larger magnetic-field scans need to be understood in terms of material properties. It is clear from the experimental results that the response exhibits various response transitions and saturation as observed by differences in the transfer curve slopes as the magnetic field is incremented. In contrast, the simulation results presented in Fig. 4.6(c) employed a simple linear approach rather than sigmoidal response.

The asymmetry between the values at the minimum and maximum magnetic-field polarities (see Fig. 3.8(b)) makes a significant difference as well. The range from -1.5 T to -0.5 T gives a slope value of 2.57 mV/T, while from 0.5 T to 1.5 T, the slope value is 4.47 mV/T. These variations impact the estimate of carrier density (n_s) and mobility (μ). For example, using a value of 2.57 mV/T yields n_s and μ values of 2.42×10¹¹ cm⁻² and 81,700 cm²/Vs, respectively, whereas using 4.47 mV/T the calculated values are $n_s = 1.4 \times 10^{11}$ cm⁻² and $\mu = 142,000$ cm²/Vs. Furthermore, the slope value from -0.5 T to 0.5 T is 2.85 mV/T, and the calculated n_s and μ

$2.19 \times 10^{11} \text{ cm}^{-2}$ and $90,400 \text{ cm}^2/\text{Vs}$, respectively. The n_s and μ variability due to the non-linear response of the sensor at $B = \pm 5 \text{ T}$ shows a limitation of the current model. Further work is needed to input the physical parameters responsible for this behavior in the model.

Table 4.3. FEM-model simulation results of the Hall cross under vacuum and ambient conditions.

	P_s ($\Omega \cdot \text{m}^2$)	n_s (m^{-2})	μ (m^2/Vs)	S_I (V/AT)	B (T)	I_b (A)
Experimental vacuum condition						
Dataset 1		2.53×10^{15}	7.8	2,496		
Dataset 2		1.94×10^{15}	10.2	3,250	± 0.05	
Average	9.45×10^{-13}	2.21×10^{15}	8.9	2,846		1×10^{-6}
Dataset 1		3.22×10^{15}	6.1	1,370	± 5	
Experimental ambient condition						
		2.44×10^{15} to 9.35×10^{16}	0.24 to 14.8	19 to 2,718		1×10^{-6}
Dataset 1	9.45×10^{-13}	2.24×10^{15} to 5.45×10^{17}	0.04 to 18.3	47 to 3,202	± 0.05	10×10^{-6}
		2.84×10^{15} to 1.77×10^{17}	0.12 to 13.6	39 to 2,354		100×10^{-6}
Simulation vacuum condition						
Dataset 1		2.64×10^{15}	7.5	2,366		
Dataset 2		2.02×10^{15}	9.8	3,089	± 0.05	1×10^{-6}
Average	9.45×10^{-13}	2.30×10^{15}	8.6	2,710		
Dataset 1		3.23×10^{15}	6.1	1,927	± 5	1×10^{-6}
Simulation ambient condition						
		2.53×10^{15} to 9.76×10^{16}	0.23 to 14.2	64 to 2,462		1×10^{-6}
Dataset 1	9.45×10^{-13}	2.33×10^{15} to 5.69×10^{17}	0.03 to 17.7	11 to 2,680	± 0.05	10×10^{-6}
		2.96×10^{15} to 1.85×10^{17}	0.11 to 13.1	34 to 2,111		100×10^{-6}

The comparative experimental and simulation results for an EMR device are presented in Table 4.5. For the results obtained the agreement shows a percentage error of 11.5%. Such a difference in the agreement between the Hall-cross and the EMR-device simulation is attributed to the input values of carrier density and mobility. When the electrical properties of graphene are characterized with the EMR device, the metallic shunt can be expected to modify interfacial material properties that can modify transport properties. This can influence the mobility and carrier-density estimates. Nevertheless, the discrepancy can be reduced by implementing the gate-voltage dependency in the model to tune the sheet resistance of graphene. From the field-effect curves these intrinsic properties can be calculated [93].

The prediction studies show that a sensitivity of 1.9 nT/ $\sqrt{\text{Hz}}$ (180,000 cm²/Vs) and of 443 pT/ $\sqrt{\text{Hz}}$ (245,000 cm²/Vs) are attainable with an EMR device. This demonstrates that the EMR design outperforms the Hall cross because it combines geometric and Hall effects, leading to a higher signal response. Devices capable of providing such sensitivities can readily be applied to the study of biomagnetic signals from the heart and skeletal muscle.

Table 4.4. Comparison of FEM simulation results with experiments for EMR devices operating at RT under ambient conditions.

P_s ($\Omega \cdot m^2$)	n_s (m^{-2})	μ (m^2/Vs)	S_I (V/AT)	B (T)	I_b (A)
Experimental ambient condition					
7.97×10^{-13}	6.11×10^{15} to 1.63×10^{18}	0.03 to 12.3	41 to 1,036	± 0.05	100×10^{-6}
Simulation ambient condition					
7.97×10^{-13}	7.9×10^{15} to 2.2×10^{18}	0.02 to 9.79	2 to 820	± 0.05	100×10^{-6}

5. CONCLUSIONS

The work presented in this dissertation describes the successful fabrication and characterization of graphene-based magnetometers from two graphene sources, mechanical exfoliation, and CVD growth. Under ambient conditions at RT, the CVD EMR device (EMR1), with mobility of $1,200 \text{ cm}^2/\text{Vs}$ and carrier density of $5.5 \times 10^{12} \text{ cm}^{-2}$ reached a sensitivity of $18 \text{ } \mu\text{T}/\sqrt{\text{Hz}}$. The sensing area of this device was $2.2 \text{ mm} \times 1.1 \text{ mm}$. Similarly, the CVD EMR device (EMR2) with a sensing area of $1.2 \text{ mm} \times 0.6 \text{ mm}$ attained a sensitivity of $62 \text{ } \mu\text{T}/\sqrt{\text{Hz}}$. Its mobility and carrier density were $1,100 \text{ cm}^2/\text{Vs}$ and $5.7 \times 10^{12} \text{ cm}^{-2}$, respectively.

Devices exposed to ambient atmospheric conditions for 24 months exhibited significant changes in material properties and performance. This is attributed to chemisorption of oxygen and water molecules. The total device resistance and Johnson noise increased, both of which limit magnetic resolution. This also resulted in shifts of the CNP voltage that impact device reproducibility in the absence of protection from ambient conditions. An important requirement for optimum device performance is the optimization of gate voltage bias to achieve the highest current and voltage sensitivities.

This work also established that the signal response in EMR devices scales with the device sensing-area size. Furthermore, their response is found to be higher than for Hall-bar devices as the EMR effect takes advantage of the Hall and geometric effects. As discussed, the mobility in CVD-graphene devices is limited by grain-boundary scattering processes and electron-phonon coupling loss mechanisms. To enhance the sensitivity of CVD graphene-based magnetometers, their encapsulation in h-BN should be pursued in future work. We anticipate that this could augment their sensitivity into the nT regime and beyond.

This dissertation also presented the successful fabrication and characterization of a Hall-cross magnetic sensor reaching a sensitivity of $686 \text{ nT}/\sqrt{\text{Hz}}$. The graphene sensor layer was characterized to have a mobility of $\sim 148,000 \text{ cm}^2/\text{Vs}$ and a carrier density $\sim 3.2 \times 10^{11} \text{ cm}^{-2}$. The intrinsic device properties were enhanced by encapsulating the graphene layer between h-BN layers. EMR sensors employing the same h-BN/graphene/h-BN structure afforded a sensitivity of $2.5 \text{ } \mu\text{T}/\sqrt{\text{Hz}}$. This device had a mobility of $\sim 94,630 \text{ cm}^2/\text{Vs}$ and carrier density $\sim 3.9 \times 10^{11} \text{ cm}^{-2}$. Encapsulation with h-BN affords environmental protection and minimizes losses in transport due to electron-phonon coupling between the graphene and the substrate material (Si/SiO₂ in this

case). This results in higher mobilities and noise reduction, and the carrier density is unaffected by undesirable doping and chemisorptive processes resulting from contamination.

The effect of adsorbates and/or contaminants incorporated into our device in the fabrication process are changes in mobility, carrier density, and contact resistance. In addition, said effects result in significant hysteresis of gate-voltage response as well as magnetoresistance that deteriorates the device performance. We note that the observed hysteresis is suppressed by conducting 10 sweep cycles of the gate-voltage range to remove trapping sites. This permitted a more precise determination of the carrier mobility.

Regarding potential improvements to the magnetic resolution of devices, injection current-induced thermal annealing is recommended to removed adsorbates from the graphene surface. Furthermore, assembly of the heterostructures using the methodology presented in Appendix A will result in cleaner interfaces, thereby improving the performance of future devices. Additional recommendations pertain to the nano-fabrication process: it is recommended that the graphene surface be cleaned prior to depositing the shunt and electrical contacts. This is projected to reduce the contact resistance and the correlated Johnson noise. Together with exploring alternative electrical-contact materials and architectures, removing contaminants from the graphene surface prior to metallization is considered an essential pathway to reduce the contact resistance from its present value of $\sim 3 \text{ k}\Omega \mu\text{m}$ to values below $150 \Omega \mu\text{m}$.

As noted, contact resistances below $150 \Omega \mu\text{m}$ can be achieved, as demonstrated in the work of Jia et al. [94]. They reported a p_s of $88 \Omega \mu\text{m}$ using Pd/Au (20/60), Zhong et al. [95] reported a p_s of $69 \Omega \mu\text{m}$ using Pd/Au (30/50), and Guinea [96] reported a p_s of $100 \Omega \mu\text{m}$ with Ni(100). In addition, Cusati et al. [97] based on modeling studies reported a predicted p_s of $30 \Omega \mu\text{m}$ using Ni as a contact material. Finally, an alternative approach to improve contact resistance is related to the geometry of the contact; for example, making graphene antidot arrays (etching holes through graphene) under the metal contact forms edge contacts. This reduces contact resistance owing to increased charge injection through graphene edges [98], [99].

We note that the graphene-based magnetometers reported in this work can be deployed significantly closer to the magnetic source than can other sensors. For example, the SQUID sensors in MEG cannot be placed less than 2 cm from the scalp t on account of their design and housing [19]. In the case of MEG using OPMs the active sensor placement is $\sim 6.5 \text{ mm}$ from the scalp [20]. Reducing the sensor-to-source distance significantly increments the amplitude

detection because of the $1/r^2$ decay of the magnetic field. The graphene-based sensors here described can be placed in direct contact with the scalp or other biomagnetic signal sources, thereby enabling the study of these signals at lower sensitivity values. Reducing the magnetic-source distance to 20 μm (the thickness of a polymer device encapsulation overlayer) by placing the sensor in contact with the scalp or skin would increment the flux amplitude between 65X (OPM) and 200X (SQUID), thereby enabling the study of biomagnetic signals with relatively slower magnetic sensitivity.

Finally, this dissertation presented a FEM model that reproduces the experimental results well, within 3% for the Hall-cross and 11.5% for the EMR devices. Thus, the model was employed to predict the response and performance of graphene-based sensors having improved intrinsic material properties and lower contact resistance. The goal of this effort is to guide the rational design of future graphene-based magnetic sensors.

The predictive studies here reported confirm that EMR devices can outperform the Hall-cross design because they combine geometry and the Hall effect to yield a higher signal response. Thus, it is predicted that an EMR device employing a graphene layer with a mobility of 180,000 cm^2/Vs can achieve a sensitivity of 1.9 $\text{nT}/\sqrt{\text{Hz}}$. Employing a higher-mobility material of 245,000 cm^2/Vs boosts the sensitivity to 443 $\text{pT}/\sqrt{\text{Hz}}$. In comparison, a Hall-cross device with identical carrier mobilities is predicted to afford sensitivities of 2.1 $\text{nT}/\sqrt{\text{Hz}}$ (180,000 cm^2/Vs) and 639 $\text{pT}/\sqrt{\text{Hz}}$ (245,000 cm^2/Vs). These sensitivities are sufficient for the study of biomagnetic signals emanating from the human heart and skeletal muscles. Furthermore, given the reduction of spacing between the magnetic signal source and the graphene-based magnetic sensors, the magnetic flux enhancement at the sense layer can enable the detection of biomagnetic signals with lower device sensitivity than that of those currently employed.

APPENDIX A. METHOD FOR FABRICATION OF BUBBLE-FREE GRAPHENE/H-BN STACKS

This appendix describes an alternative method to fabricate encapsulated graphene on h-BN. This constitutes an improvement over that described in Chapter 2.

The assembly starts by setting the sample-holder temperature at 40 °C and localizing the h-BN cap on the substrate. Once that is localized, the stamp is lowered until the PC is close to the h-BN flake, as shown in Fig. A.1(a). Next, the temperature is increased to 80 °C at a rate of 2 °C/min to expand the PC and cover the h-BN flake, as shown in Fig. A.1(b). Once the flake is fully covered, the temperature is held for 10 min before cooling to 40 °C at the same temperature rate. The PC contracts as the temperature decreases, and the adhered h-BN flake peels off (see Fig. A.1(c)) without breaking. Fig. A.1(d) shows the successful pickup of the h-BN cap. Then, the stamp is raised in order to change the substrate that contains the graphene flake.

The graphene is then located; using the micrometer stage alignment control, the stamp with the h-BN cap is placed above the graphene monolayer, as illustrated in Fig. A.1(e). The stamp is lowered until the PC is close to the graphene layer at which point the temperature is increased from 40 °C to 80 °C at a rate of 1 °C/min. As the PC expands, the h-BN is brought into contact with the graphene layer as shown in Fig. A.1(f). The temperature is held at 80 °C for 10 min to ensure that the PC fully covers the graphene. The temperature is then reduced to 40 °C at the same temperature rate. Fig. A.1(g) shows the thermal peeling of graphene being picked up by h-BN owing to the van der Waals forces. The successful retrieval of graphene as well as additional materials is shown in Fig. A.1(h). The stamp is elevated to introduce the substrate that contains the bottom h-BN flake.

The stamp containing the h-BN/G stack is placed above the substrate with bottom h-BN as shown in Fig. A.1(i). The same procedure as described in the prior paragraph is repeated. The PC with the stack covering the bottom h-BN flake is shown in Fig. A.1(j). The cooldown of the PC is done as previously described; see Fig. A.1(k). The completion of the stack fabrication is the transfer of the trilayer structure onto the substrate that will be used for patterning. This substrate has alignment marks for nano-fabrication purposes that are used as references to align the stack dropdown position. The stamp is lowered until the stack is visible (see Fig. A.1(m)), and then the temperature is increased from 40 °C to 80 °C at a rate of 2 °C/min. Fig. A.1(n) shows the

transferred stack and additional materials picked up by the PC stamp. Next, using the same increase rate, the temperature is raised from 80 °C to 160° C to exceed the PC glass-transition temperature and make it flow over the substrate. In addition, the stamp is pressed onto the substrate (see Fig. A.1(o)) to force bubbles to diffuse out. A.1(p) shows the substrate completely covered by the PC mask following the pressure step. Caution needs to be exercised not to apply excessive pressure that could break the stage glass support.

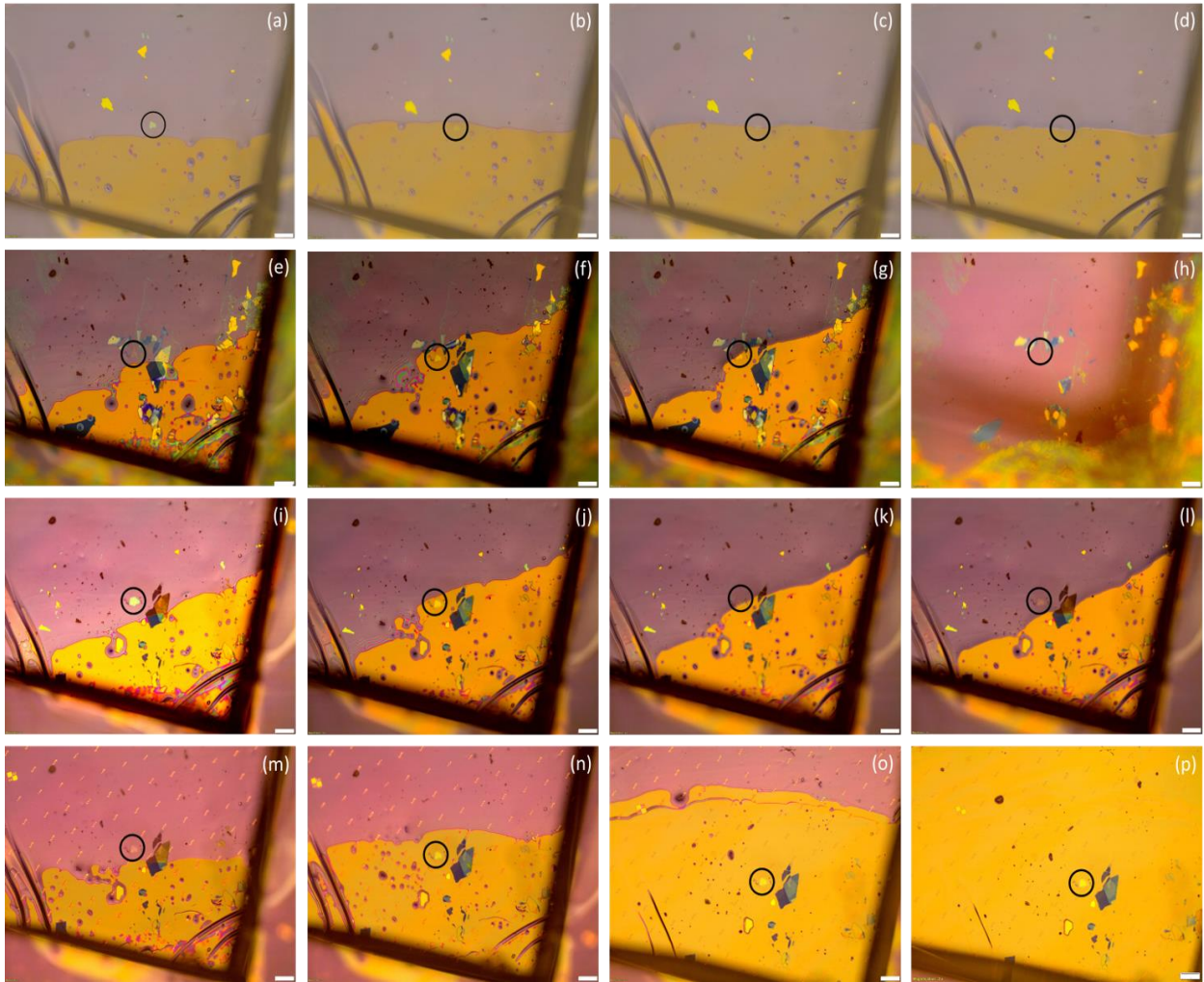


Fig. A.2. Procedure to encapsulated graphene on h-BN. (a-d) h-BN cap pickup by the polymeric stamp by the van der Waals method. (e-h) Graphene pickup by the stamp containing h-BN. (i-l) h-BN bottom pickup by the stamp containing h-BN/G stack. (m-p) Transfer of the stack to substrate with alignment marks. The black circle shows the localization of the h-BN cap, graphene, and h-BN bottom. Scale bar 200 μm .

The trilayer stack sample is inspected using an optical microscope as shown in Fig. A.2(a). The image shows the trilayer structure as well as the presence of bubbles. To identify bubble-free regions and to confirm the successful assembly of the trilayers, Raman spectroscopy and AFM were employed. The Raman spectrum and Raman maps are presented in Fig. A.2(b); they exhibit the characteristics peak for h-BN at 1366 cm^{-1} and the G and 2D graphene peaks at 1580 cm^{-1} and 2690 cm^{-1} , respectively.

The Raman map shows the area where the graphene monolayer (green) is localized within the hBN flakes (red). The AFM surface images and profile plots in Fig. A.2(c) & (d) show the spatial distribution and the height of the bubbles. Based on the profile plots and the surface images, the total stack height is determined to be $\sim 23\text{ nm}$ and the bubble-free area is $\sim 13\text{ }\mu\text{m} \times 13\text{ }\mu\text{m}$.

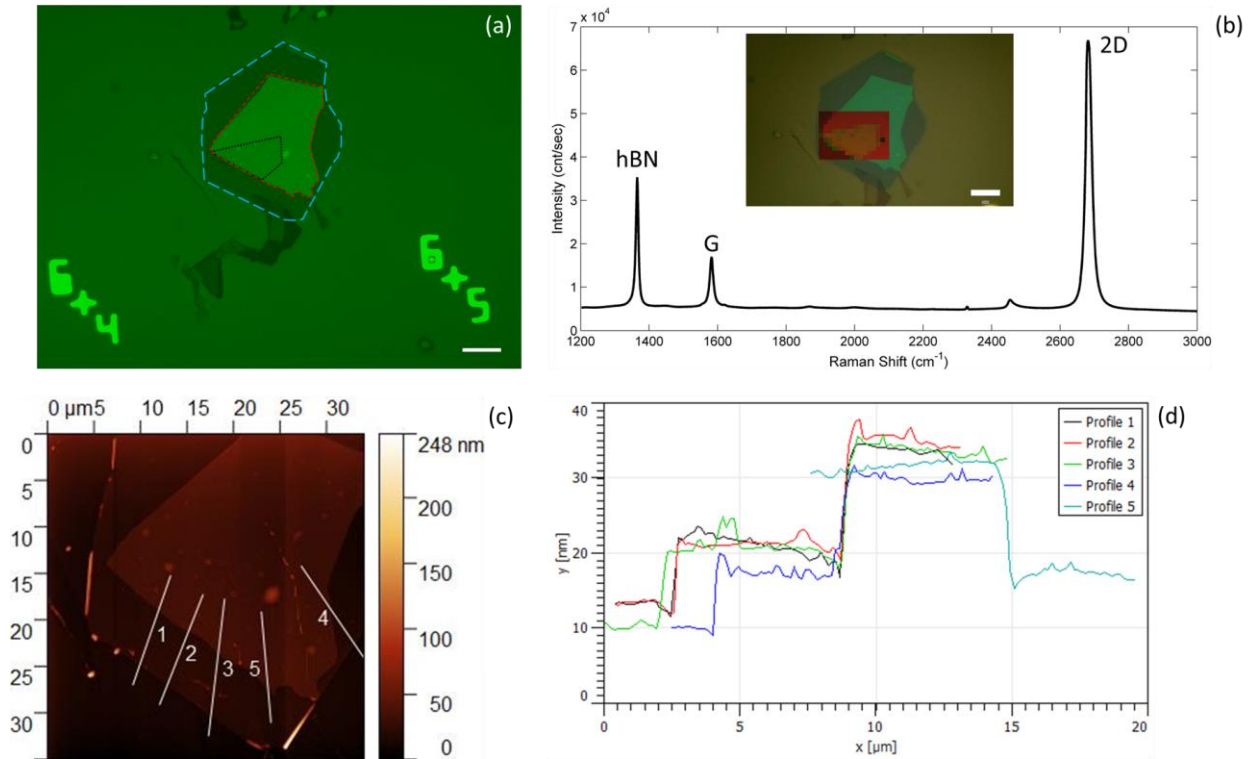


Fig. A.3. Characterization of the h-BN/G/h-BN stack. (a) Optical microscopy image of the stack: the h-BN bottom layer is outlined by with the blue dashed line, the graphene layer with the black dashed line, and h-BN cap with the red dashed line. The scale bar is $10\text{ }\mu\text{m}$. (b) Raman spectrum showing the h-BN main peak at 1366 cm^{-1} and the graphene G and 2D main peaks at 1580 cm^{-1} and 2690 cm^{-1} . The inset displays the Raman map identifying the graphene (green) and h-BN (red) flakes. The scale bar $10\text{ }\mu\text{m}$. (c) AFM surface image showing the regions used to measure topography profiles. (d) Topography profiles across the line regions shown in (c).

APPENDIX B. MEASUREMENT OF CONTACT RESISTANCE WITH THE TLM METHOD

This appendix describes the use of the TLM method to derive contact resistance (p_s) in the CVD-grown and mechanically exfoliated graphene devices as discussed in Chapter 3.

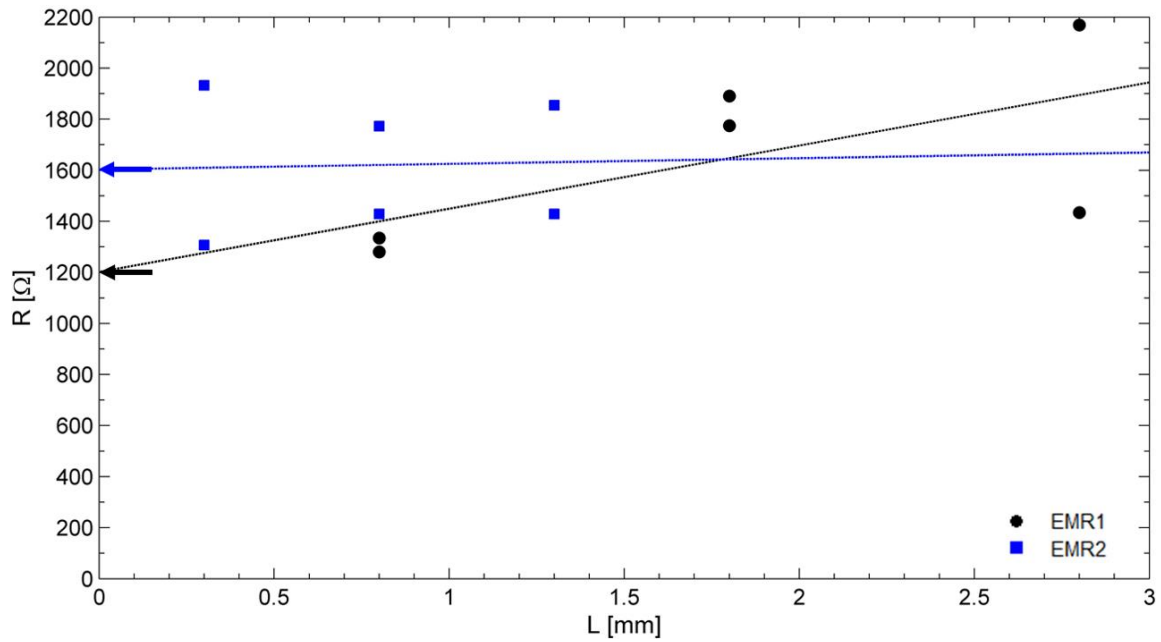


Fig. B. 4. Two-terminal resistance vs. contact spacing yields the value (at intercept) of twice the contact resistance (R_c). The measurements correspond to EMR1 (black) and EMR2 devices (blue) measured 24 months after fabrication. Arrows indicate the value of $2 \times R_c$.

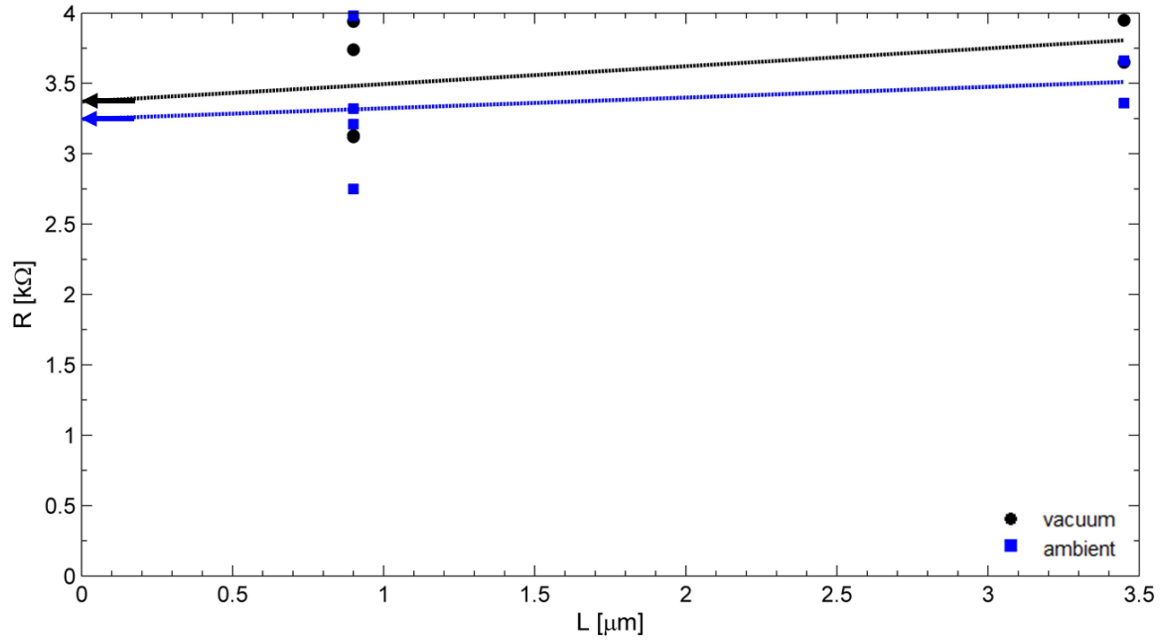


Fig. B. 5. Two-terminal resistance vs. contact spacing yields the value (at intercept) of twice the contact resistance (R_c). The measurements correspond to the Hall cross-device at RT under vacuum (black) and ambient (blue) conditions. Arrows indicate the value of $2xR_c$.

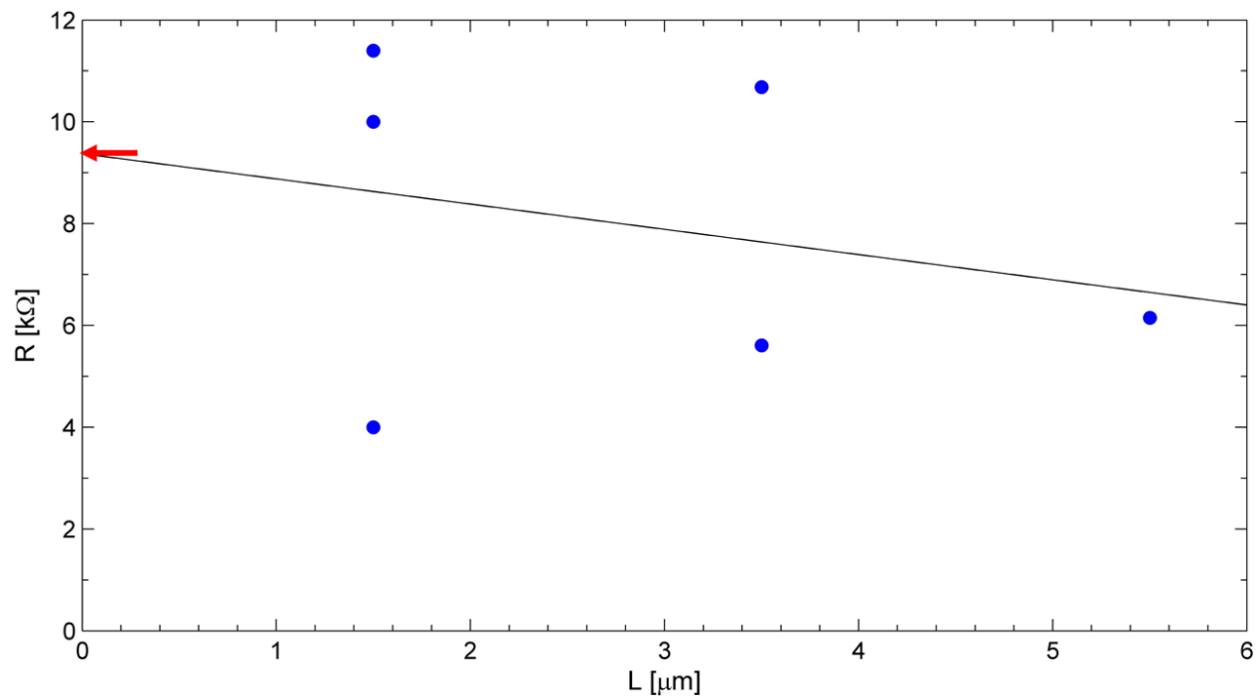


Fig. B. 6. Two-terminal resistance vs. contact spacing yields the value (at intercept) of twice the contact resistance (R_c). The measurements correspond to an unaged EMR device at RT under ambient conditions. Arrows indicate the value of $2 \times R_c$.

APPENDIX C. EFFECT OF THE SWEEPING RATE OF THE GATE VOLTAGE ON SIGNAL RESPONSE

This appendix presents the effect of decreasing the gate voltage sweeping rate for bias currents (AC) of $10\ \mu\text{A}$ and $100\ \mu\text{A}$ under ambient conditions at RT. Discussion of the results is given in Chapter 3.

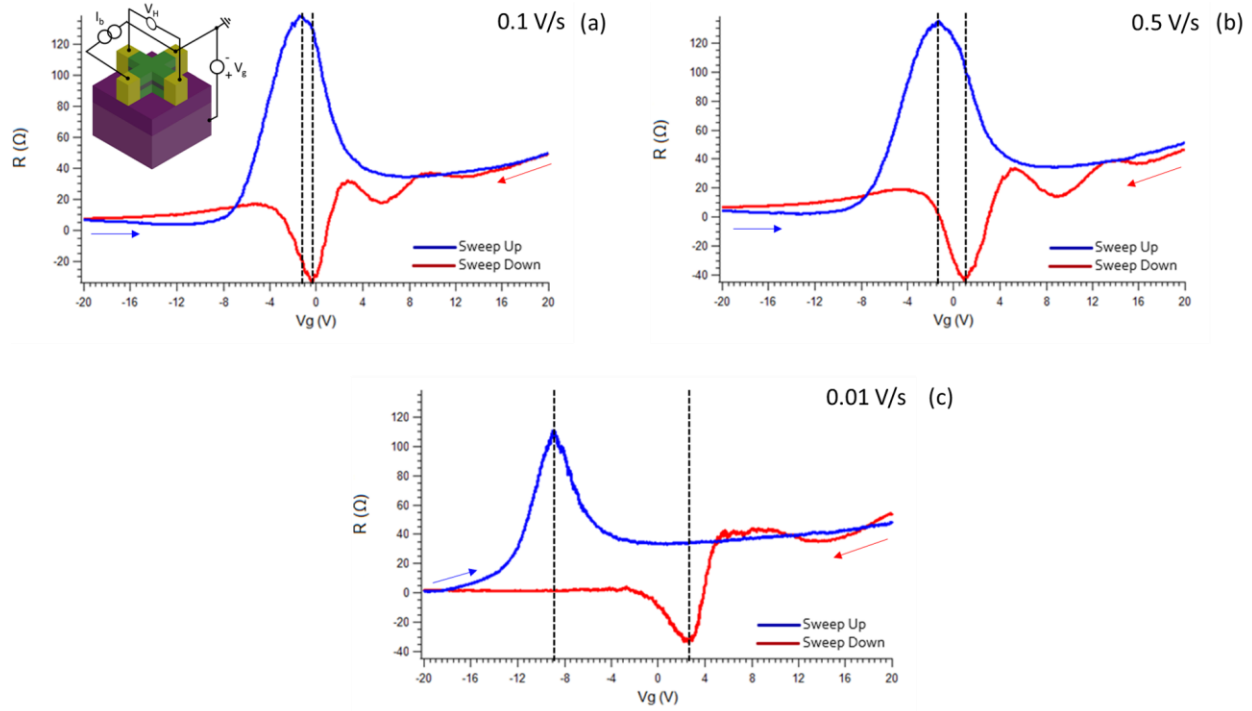


Fig. C.3. Hall cross device resistance vs. gate voltage as a function of the gate-voltage sweep rate measured perpendicular to the injection current channel. The input current was $10\ \mu\text{A}$ and the gate voltage is swept from positive (blue line) to negative polarity (red line) and repeated. The inset shows the electrical connections used for the measurements.

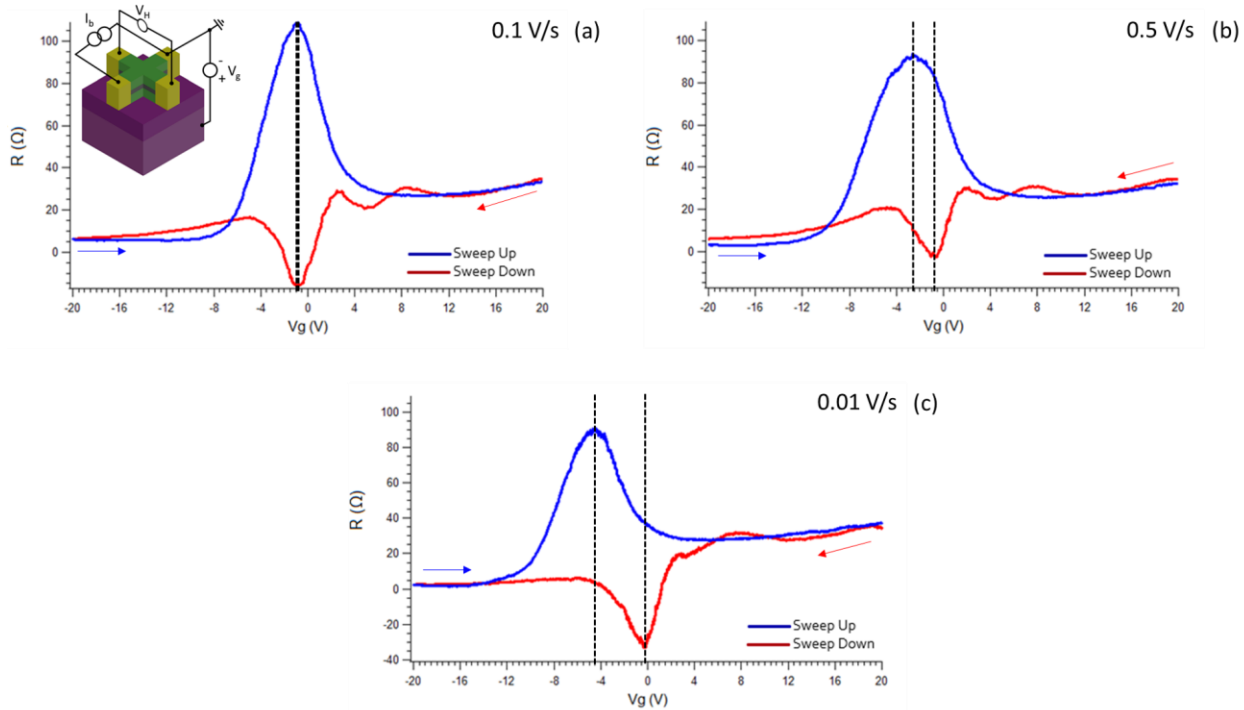


Fig. C.4. Hall cross device resistance vs gate voltage as a function of the gate-voltage sweep rate measured perpendicular to the injection current channel. The input current was $100 \mu\text{A}$ and the gate voltage is swept from positive (blue line) to negative polarity (red line) and repeated. The inset shows the electrical connections used for the measurements.

APPENDIX D. MAGNETIC RESPONSE OF THE HALL CROSS-DEVICE AND THE EMR DEVICE

This appendix presents the magnetic response of the Hall-cross device. The measurements were performed by applying bias currents of 1 μA and 10 μA at 7.7 Hz in ambient conditions. The discussion of these results is given in Chapter 3.

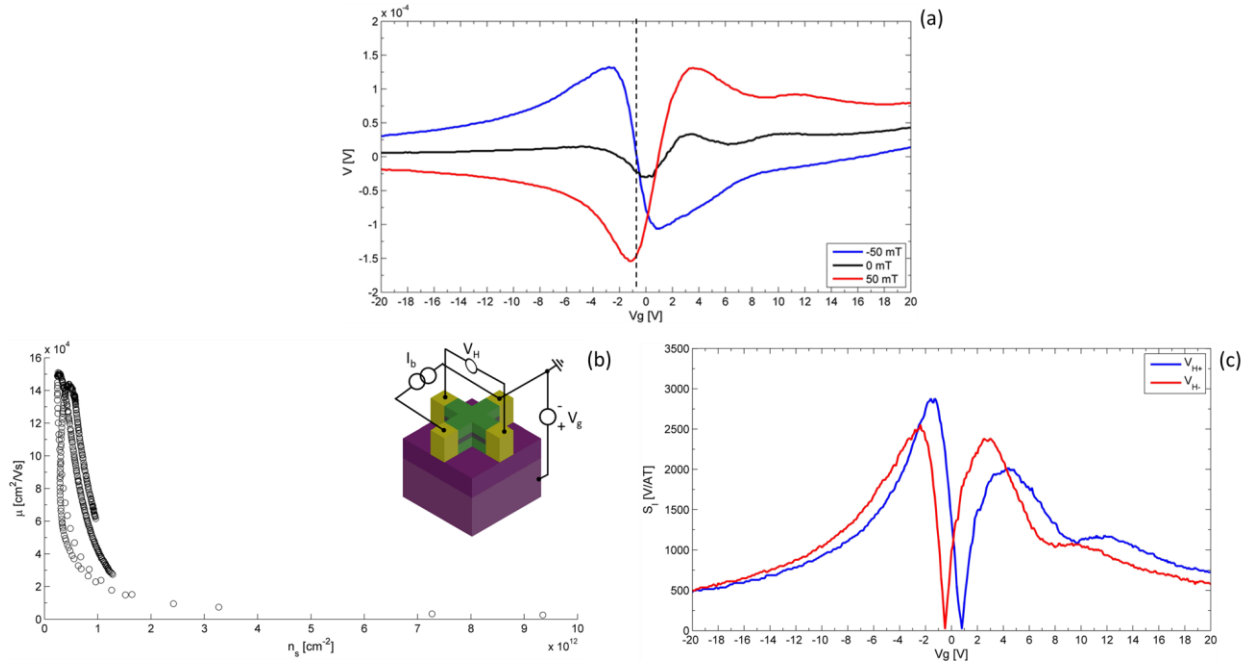


Fig. D.5. Magnetic response of the Hall cross at RT under ambient conditions. (a) V vs. V_g at three different values of the applied magnetic field: -50 mT (blue line), 0 mT (black line), and 50 mT (red line). (b) Correlation of μ and n_s . (c) S_I as a function of V_g at V_{H+} (V_H (50 mT) – V_H (0 mT), blue line) and V_{H-} (V_H (-50 mT) – V_H (0 mT), red line). The injection current was 1 μA . Inset shows the electrical connections used for the measurements. From the schematic, I_b on the left side, V_H on the top side, and V_g on the right side.

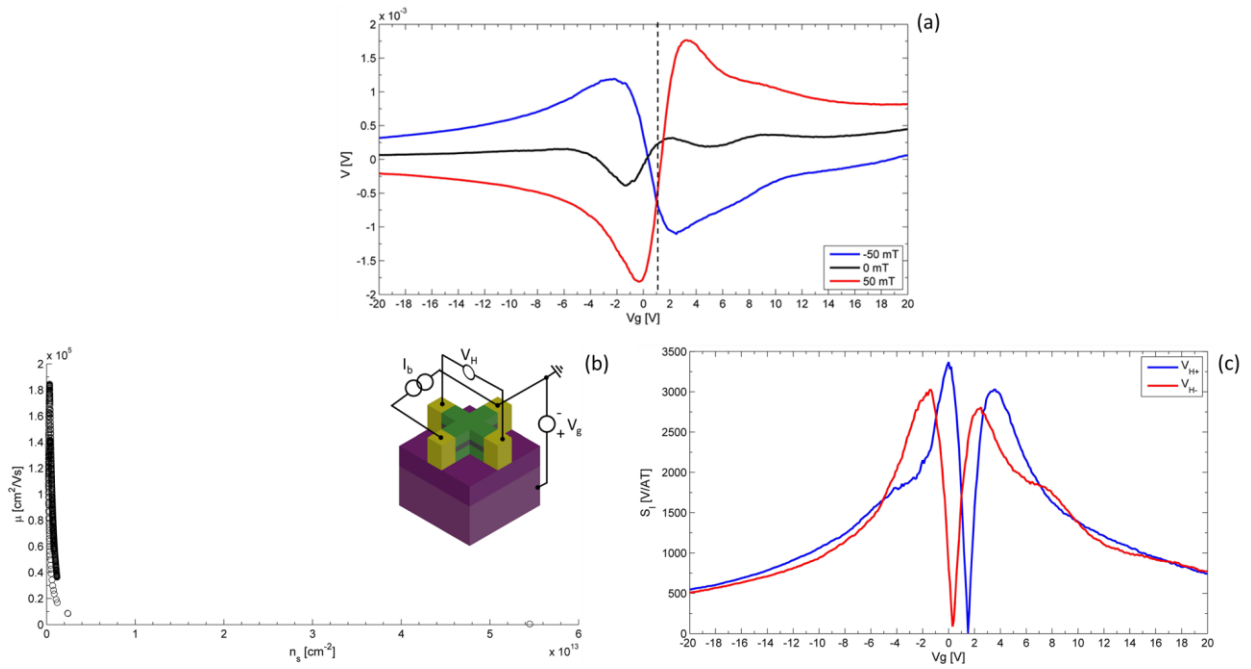


Fig. D.6. Magnetic response of the Hall cross at RT under ambient conditions. (a) V vs. V_g at three different values of the applied magnetic field: -50 mT (blue line), 0 mT (black line), and 50 mT (red line) (b) correlation of μ and n_s . (c) S_dI as a function of V_g at V_{H+} (V_H (50 mT) – V_H (0 mT), blue line) and V_{H-} (V_H (-50 mT) – V_H (0 mT), red line). The injection current was 10 μA . Inset show the electrical connections used for the measurements. From the schematic, I_b on the left side, V_H on the top side, and V_g on the right side.

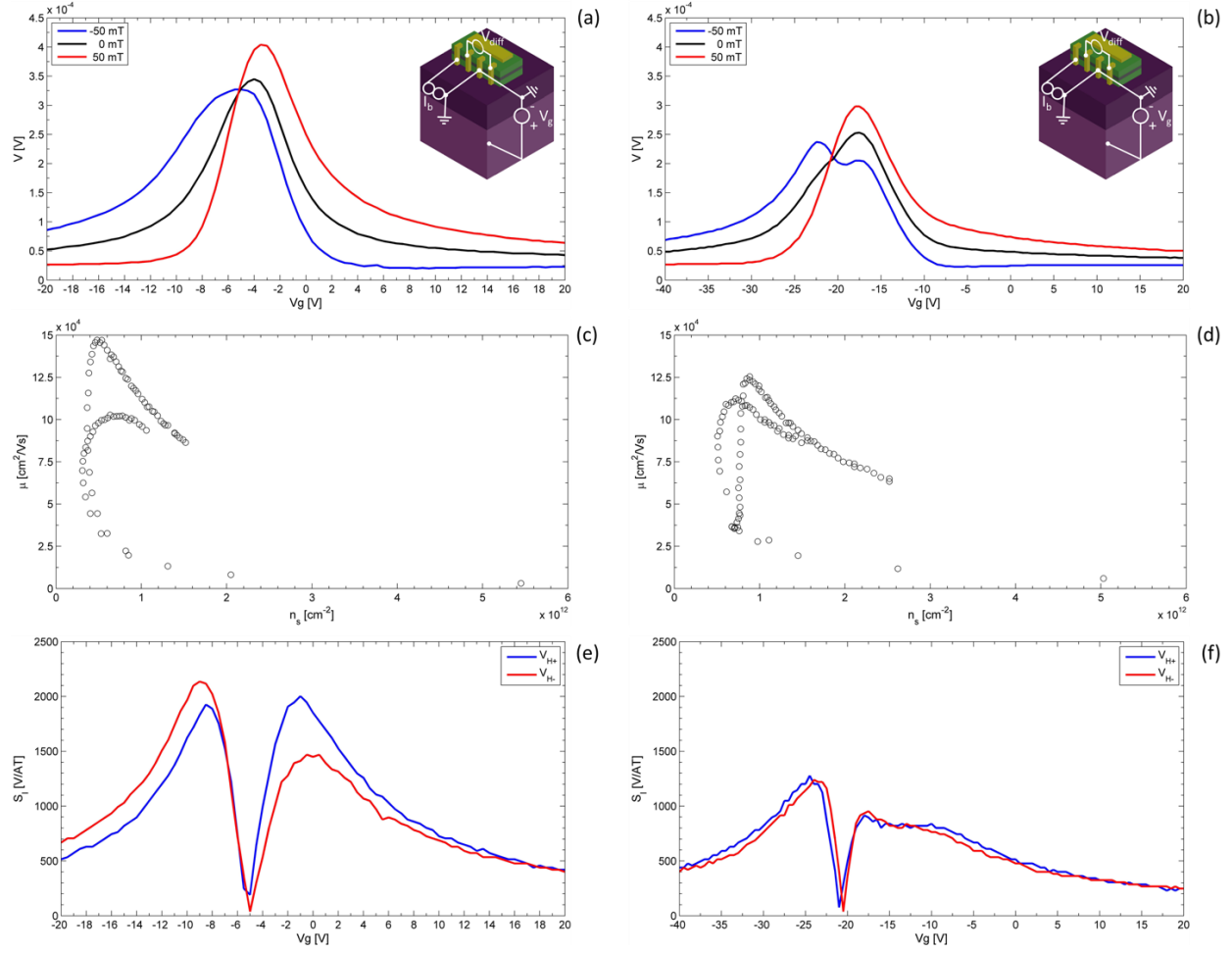


Fig. D. 7. Magnetic response of an EMR device at RT under ambient conditions. (a) V vs. V_g at three different values of the applied magnetic field: -50 mT (blue line), 0 mT (black line), and 50 mT (red line). The gate voltage bias range in (b) is twice that of (a). The correlation between μ and n_s is presented in (c) and (d) and are derived from the measurements in (a) & (b). The dependence of S_I vs. V_g at V_{H+} (V_H (50 mT) – V_H (0 mT), blue line) and V_{H-} (V_H (-50 mT) – V_H (0 mT), red line) is presented in (e) & (f). The injection current was 1 μ A. Inset show the electrical connections used for the measurements. From the schematic, I_b on the left side, V_H on the top side, and V_g on the right side.

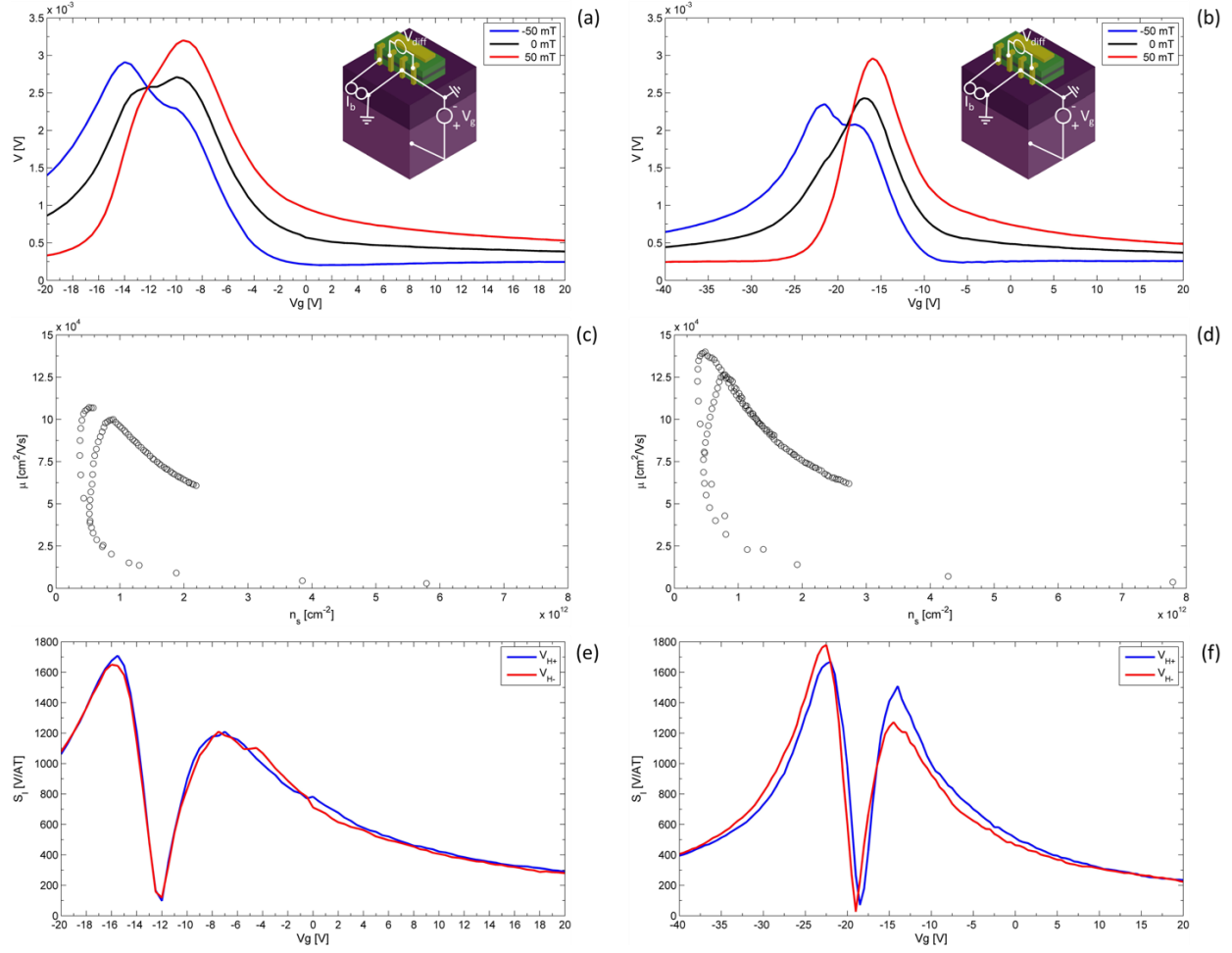


Fig. D. 8. Magnetic response of an EMR device at RT under ambient conditions. (a) V vs. V_g at three different values of the applied magnetic field: -50 mT (blue line), 0 mT (black line), and 50 mT (red line). The gate voltage bias range in (b) is twice that of (a). The correlation between μ and n_s is presented in (c) and (d) and are derived from the measurements in (a) & (b). The dependence of S_I vs. V_g at V_{H+} (V_H (50 mT) – V_H (0 mT), blue line) and V_{H-} (V_H (-50 mT) – V_H (0 mT), red line) is presented in (e) & (f). The injection current was 10 μ A. Inset shows the electrical connections used for the measurements. From the schematic, I_b on the left side, V_H on the top side, and V_g on the right side.

APPENDIX E. NOISE MEASUREMENTS OF THE CVD GRAPHENE EMR DEVICES UNDER AMBIENT CONDITIONS

This appendix describes the noise measurements of the CVD graphene EMR devices. Results are compared with those for the exfoliated-graphene Hall-cross and EMR devices. These results are discussed in chapter 3.

The noise characterization of the CVD-graphene EMR devices was performed in ambient conditions. A function generator (33521A, from Agilent) was used to apply sine-wave currents (AC) at 18.3 Hz through the current tabs. The measurement of the potential difference was made with an instrumentation amplifier (INAMP) model AD622 from Analog Devices by connecting the voltage tabs into the INAMP differential inputs. The output of the INAMP was connected to an oscilloscope (MSO-X 3014T).

The electrical circuit diagram (see Fig. E.1(a)) shows the source voltage (sine wave) and the resistor used to deliver a constant current of 1 μA , 10 μA , and 100 μA . The EMR voltage difference was amplified with a gain of 100 and later displayed in the oscilloscope. Fig E.1(b) shows the setup used to perform the measurements.

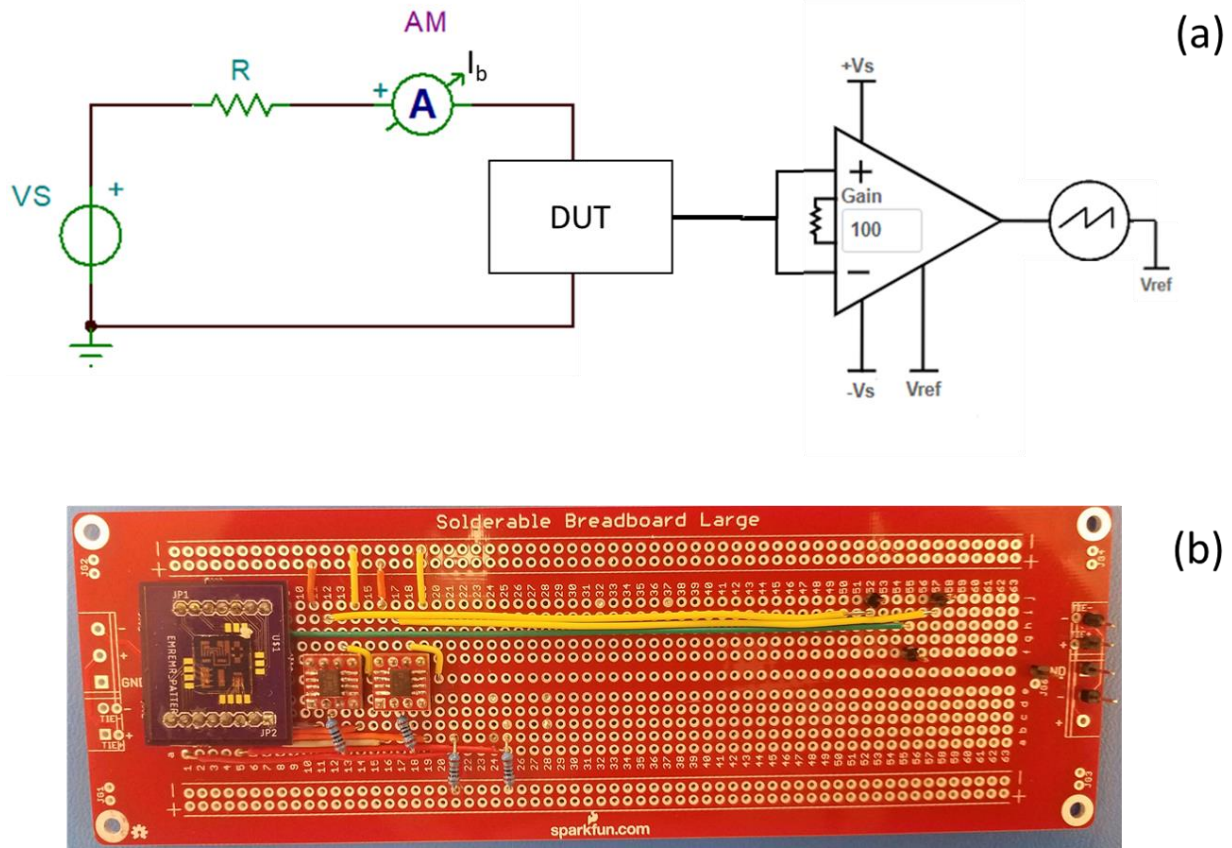


Fig. E. 4. Experimental setup for noise measurements in ambient conditions at RT. (a) Electrical circuit diagram showing the utilized components utilized, including signal amplification of 100x. (b) Photograph of the circuit employed to perform noise measurements of EMR1 and EMR2 devices.

The noise measurements were performed on devices stored for 24 months and conducted with no applied magnetic field or gate voltage, using the procedure described in section 3.2.2. The plot in Fig. E.2(a) corresponds to EMR1 and provides the *PSD* vs. frequency (*f*) dependence. It exhibits *1/f* behavior, decreasing with increasing frequency. The *PSD* values at 3 kHz are 2.10×10^{-14} V²/Hz, 1.33×10^{-14} V²/Hz, and 4.50×10^{-14} V²/Hz for injection currents of 1 μ A, 10 μ A, and 100 μ A, respectively. Fig. E.2(b) shows the magnetic resolution (B_{min}) vs. Frequency, also showing *1/f* dependency. Note that the value of B_{min} decreases as the injection current is increased. The B_{min} values are 1.3×10^{-3} T/ $\sqrt{\text{Hz}}$, 98.5×10^{-6} T/ $\sqrt{\text{Hz}}$, and 18.1×10^{-6} T/ $\sqrt{\text{Hz}}$ at 3 kHz for currents of 1 μ A, 10 μ A, and 100 μ A, respectively.

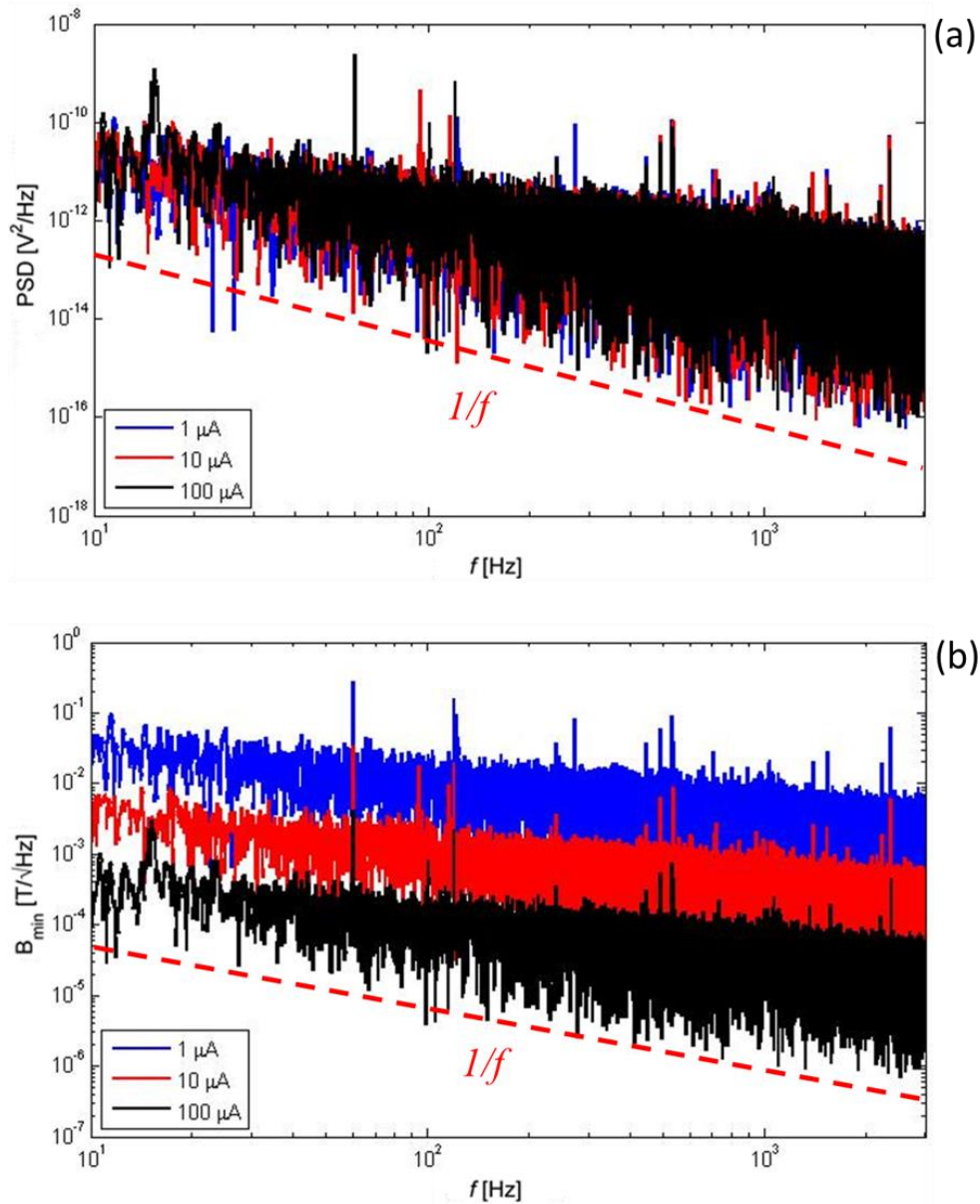


Fig. E. 5. Noise measurements for the EMR1 device, performed at RT and ambient conditions without applied magnetic field. This device was measured after being stored in the lab environment for 24 months. (a) PSD vs f . (b) B_{min} vs. f . The injection currents were: $1 \mu A$ (blue trace), $10 \mu A$ (red trace) and $100 \mu A$ (black trace). The red dashed line is drawn to illustrate $1/f$ dependency.

The plot for the EMR2 device PSD vs. f is shown in Fig. E.3(a), exhibiting $1/f$ dependency as well. The PSD values are $4.39 \times 10^{-14} \text{ V}^2/\text{Hz}$, $5.93 \times 10^{-14} \text{ V}^2/\text{Hz}$, and $4.71 \times 10^{-13} \text{ V}^2/\text{Hz}$ at 3k Hz for currents of 1 μA , 10 μA , and 100 μA , respectively. Fig. E.3(b) shows the plot for B_{min} as a function of f . As in the previous case, B_{min} improves as the current increases. The B_{min} values are $1.9 \times 10^{-3} \text{ T}/\sqrt{\text{Hz}}$, $221.3 \times 10^{-6} \text{ T}/\sqrt{\text{Hz}}$, and $62.4 \times 10^{-6} \text{ T}/\sqrt{\text{Hz}}$ at 3 kHz for currents of 1 μA , 10 μA , and 100 μA , respectively.

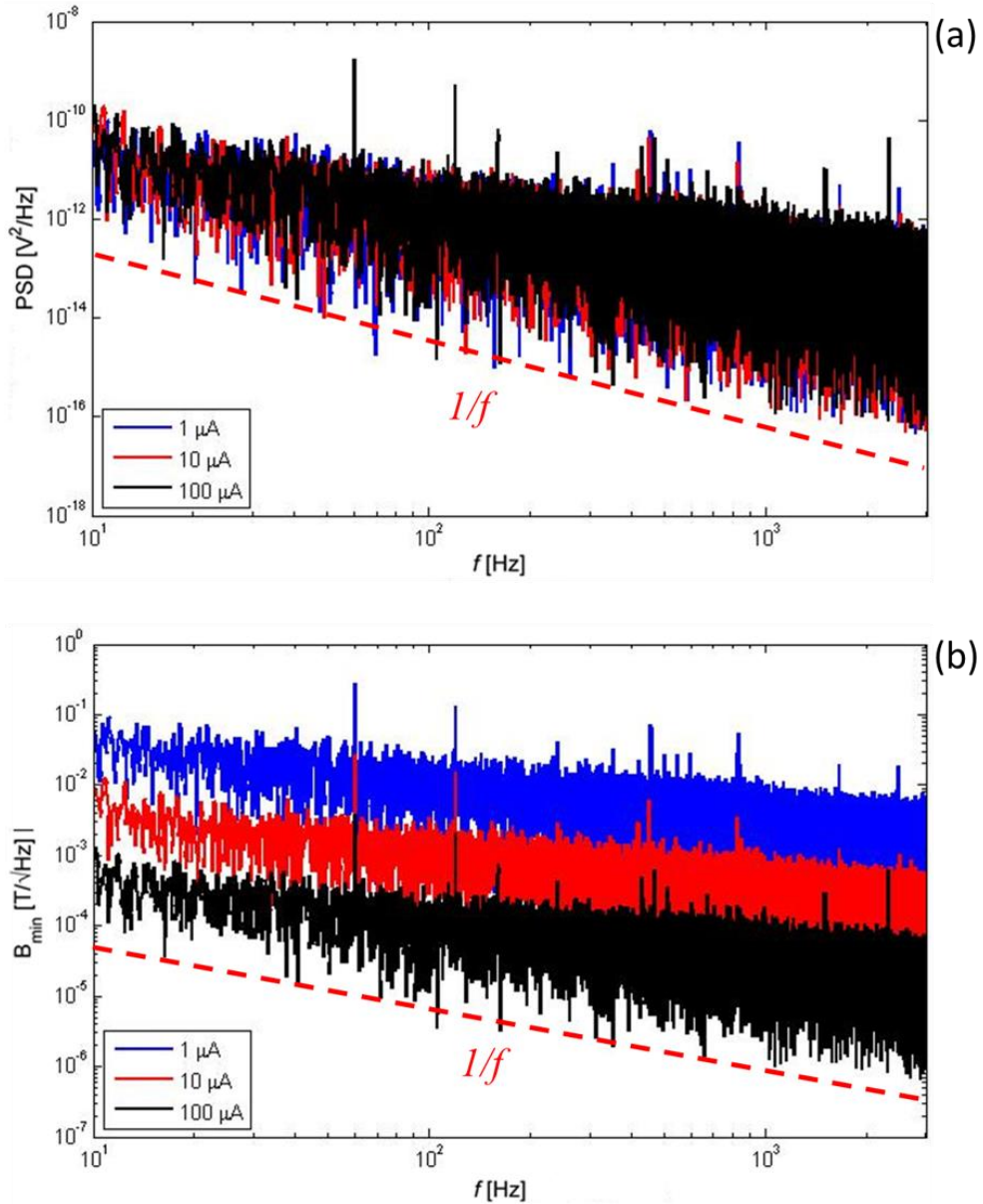


Fig. E. 6. Noise measurements for the EMR2 device, performed at RT and ambient conditions without applied magnetic field. This device was measured after being stored in the lab environment for 24 months. (a) PSD vs f . (b) B_{\min} vs. f . The injection currents were: $1 \mu\text{A}$ (blue trace), $10 \mu\text{A}$ (red trace) and $100 \mu\text{A}$ (black trace). The red dashed line is drawn to illustrate $1/f$ dependency.

APPENDIX F. COMPARISON OF FEM SIMULATION AND EXPERIMENTAL RESULTS

This appendix compares FEM-model simulation data to the experimental values for devices operated in ambient conditions at RT. The injection currents employed were 10 μA and 100 μA . The main discussion of these results is in Chapter 4.

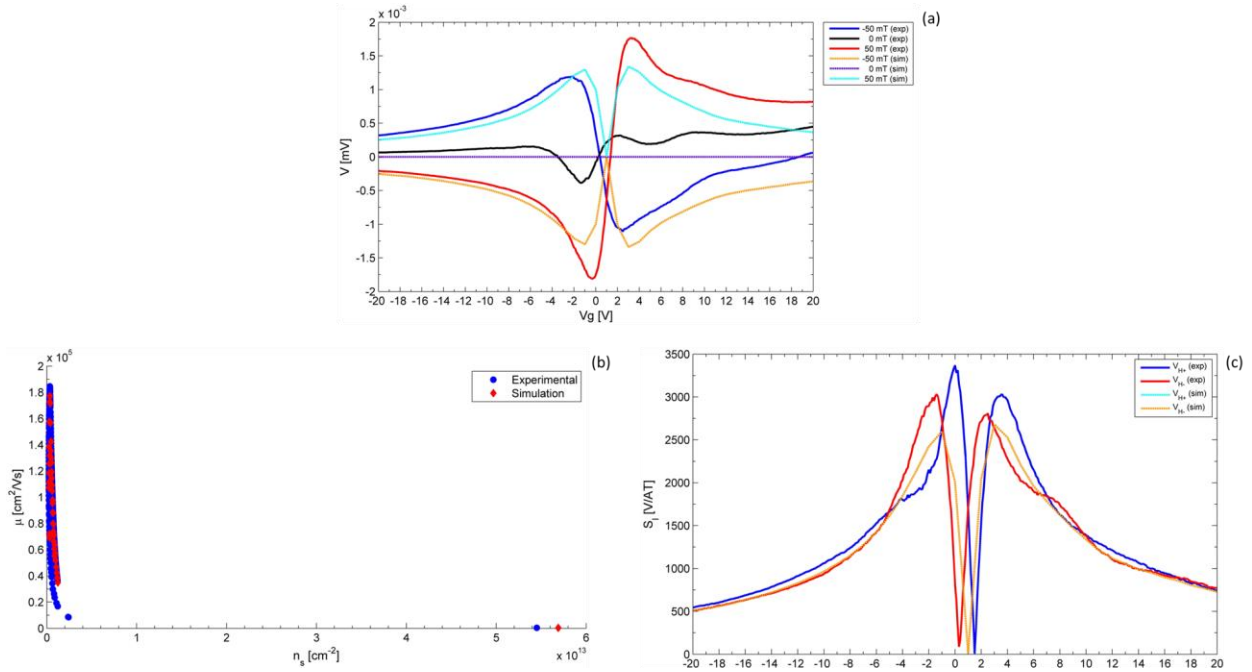


Fig. F. 3. Comparison of FEM results with experiments: (a) V vs. V_g as a function of applied magnetic field: $B = -50$ mT, 0 mT, and 50 mT (blue, black, and red lines). Simulation results $B = -50$ mT, 0 mT, and 50 mT (orange, purple, and cyan lines).

(b) μ as a function of n_s . Experimental data (blue circles) and simulation data (red diamonds). (c) S_1 vs. of V_g . Experimental data (blue and red lines) and simulation data (cyan and orange lines). Applied current, 10 μA .

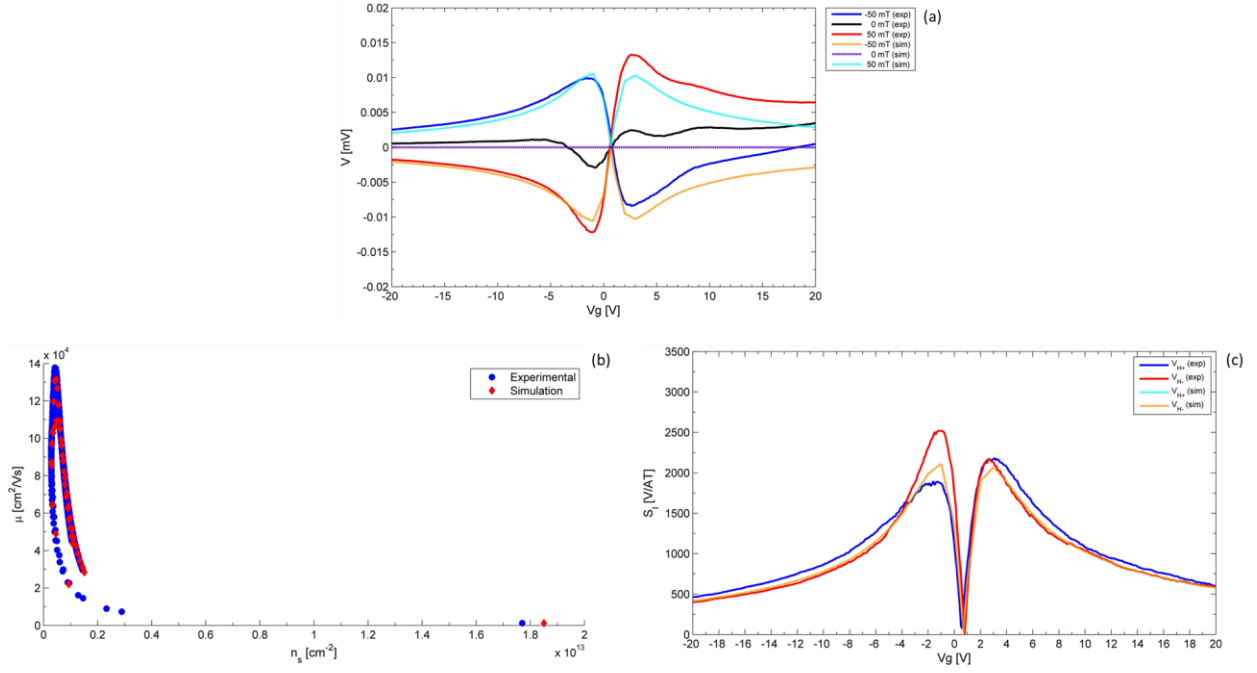


Fig. F. 4. Comparison of FEM results with experiments: (a) V vs. V_g as a function of applied magnetic field: $B = -50$ mT, 0 mT, and 50 mT (blue, black, and red lines). Simulation results $B = -50$ mT, 0 mT, and 50 mT (orange, purple, and cyan lines). (b) μ as a function of n_s . Experimental data (blue circles) and simulation data (red diamonds). (c) S_I vs. of V_g . Experimental data (blue and red lines) and simulation data (cyan and orange lines). Applied current, $100 \mu\text{A}$.

REFERENCES

- [1] S. Pisana, P. M. Braganca, E. E. Marinero, and B. A. Gurney, “Tunable nanoscale graphene magnetometers,” *Nano Lett.*, vol. 10, no. 1, pp. 341–346, 2010.
- [2] G. C. O’Neill, M. Bauer, M. W. Woolrich, P. G. Morris, G. R. Barnes, and M. J. Brookes, “Dynamic recruitment of resting state sub-networks,” *Neuroimage*, vol. 115, pp. 85–95, 2015.
- [3] L. Troebinger, J. D. López, A. Lutti, S. Bestmann, and G. Barnes, “Discrimination of cortical laminae using MEG,” *Neuroimage*, vol. 102, no. P2, pp. 885–893, 2014.
- [4] F. Martini and J. L. Nath, *Fundamentals of Anatomy & Physiology*. Pearson Education, Limited, 2008.
- [5] P. Seidel, *Applied Superconductivity: Handbook on Devices and Applications*. Wiley, 2015.
- [6] M. Hämäläinen, R. Hari, R. J. Ilmoniemi, J. Knuutila, and O. V. Lounasmaa, “Magnetoencephalography theory, instrumentation, and applications to noninvasive studies of the working human brain,” *Rev. Mod. Phys.*, vol. 65, no. 2, pp. 413–497, 1993.
- [7] M. Hämäläinen and R. Hari, “10 - Magnetoencephalographic Characterization of Dynamic Brain Activation: Basic Principles and Methods of Data Collection and Source Analysis A2 - Toga, Arthur W.,” J. C. B. T.-B. M. T. M. (Second E. Mazziotta, Ed. San Diego: Academic Press, 2002, pp. 227–253.
- [8] K. Sternickel and A. I. Braginski, “Biomagnetism using SQUIDs: Status and perspectives,” in *Superconductor Science and Technology*, 2006.
- [9] W. Andrä and H. Nowak, *Magnetism in Medicine: A Handbook*. Wiley, 2007.
- [10] C. J. Aine, “Highlights of 40 years of SQUID-based brain research and clinical applications,” *IFMBE Proc.*, vol. 28, pp. 9–34, 2010.
- [11] L. J. Larson-Prior *et al.*, “Adding dynamics to the Human Connectome Project with MEG,” *Neuroimage*, vol. 80, pp. 190–201, 2013.
- [12] Z. Liu, M. Fukunaga, J. A. de Zwart, and J. H. Duyn, “Large-scale spontaneous fluctuations and correlations in brain electrical activity observed with magnetoencephalography,” *Neuroimage*, vol. 51, no. 1, pp. 102–111, 2010.

- [13] J. C. Allred, R. N. Lyman, T. W. Kornack, and M. V. Romalis, “High-Sensitivity Atomic Magnetometer Unaffected by Spin-Exchange Relaxation,” *Phys. Rev. Lett.*, vol. 89, no. 13, p. 130801, 2002.
- [14] E. Boto *et al.*, “Moving magnetoencephalography towards real-world applications with a wearable system,” *Nature*, vol. 555, no. 7698, pp. 657–661, 2018.
- [15] C. N. Johnson, P. D. D. Schwindt, and M. Weisend, “Multi-sensor magnetoencephalography with atomic magnetometers,” *Phys. Med. Biol.*, vol. 58, no. 17, pp. 6065–6077, 2013.
- [16] V. K. Shah and R. T. Wakai, “A compact, high performance atomic magnetometer for biomedical applications,” *Phys. Med. Biol.*, vol. 58, no. 22, pp. 8153–8161, 2013.
- [17] H. J. Lee, J. H. Shim, H. S. Moon, and K. Kim, “Flat-response spin-exchange relaxation free atomic magnetometer under negative feedback,” *Opt. Express*, vol. 22, no. 17, p. 19887, 2014.
- [18] O. Alem, A. M. Benison, D. S. Barth, J. Kitching, and S. Knappe, “Magnetoencephalography of Epilepsy with a Microfabricated Atomic Magnetode,” *J. Neurosci.*, vol. 34, no. 43, pp. 14324–14327, 2014.
- [19] J. Iivanainen, M. Stenroos, and L. Parkkonen, “Measuring MEG closer to the brain: Performance of on-scalp sensor arrays,” *Neuroimage*, vol. 147, no. September 2016, pp. 542–553, 2017.
- [20] E. Boto *et al.*, “A new generation of magnetoencephalography: Room temperature measurements using optically-pumped magnetometers,” *Neuroimage*, vol. 149, 2017.
- [21] S. a. Solin, “Enhanced Room-Temperature Geometric Magnetoresistance in Inhomogeneous Narrow-Gap Semiconductors,” *Science (80-.)*, vol. 289, no. 5484, pp. 1530–1532, 2000.
- [22] C. H. Möller, O. Kronenwerth, D. Grundler, W. Hansen, C. Heyn, and D. Heitmann, “Extraordinary magnetoresistance effect in a microstructured metal-semiconductor hybrid structure,” *Appl. Phys. Lett.*, vol. 80, no. 21, pp. 3988–3990, 2002.
- [23] K. S. Novoselov, “Electric Field Effect in Atomically Thin Carbon Films,” *Science (80-.)*, vol. 306, no. 5696, pp. 666–669, Oct. 2004.
- [24] K. S. Novoselov *et al.*, “Two-dimensional gas of massless Dirac fermions in graphene,” *Nature*, vol. 438, no. 7065, pp. 197–200, 2005.

- [25] Y. Zhang, Y. W. Tan, H. L. Stormer, and P. Kim, “Experimental observation of the quantum Hall effect and Berry’s phase in graphene,” *Nature*, vol. 438, no. 7065, pp. 201–204, 2005.
- [26] V. P. Gusynin and S. G. Sharapov, “Unconventional integer quantum hall effect in graphene,” *Phys. Rev. Lett.*, vol. 95, no. 14, pp. 2–5, 2005.
- [27] N. M. R. Peres, F. Guinea, and A. H. Castro Neto, “Electronic properties of disordered two-dimensional carbon,” *Phys. Rev. B - Condens. Matter Mater. Phys.*, vol. 73, no. 12, pp. 1–23, 2006.
- [28] C. Lee, X. Wei, J. W. Kysar, and J. Hone, “Measurement of the Elastic Properties and Intrinsic Strength of Monolayer Graphene,” *Science (80-.)*, vol. 321, no. 5887, pp. 385–388, Jul. 2008.
- [29] A. A. Balandin *et al.*, “Superior thermal conductivity of single-layer graphene,” *Nano Lett.*, vol. 8, no. 3, pp. 902–907, 2008.
- [30] S. Ghosh *et al.*, “Dimensional crossover of thermal transport in few-layer graphene,” *Nat. Mater.*, vol. 9, no. 7, pp. 555–558, 2010.
- [31] K. V. Zakharchenko, M. I. Katsnelson, and A. Fasolino, “Finite temperature lattice properties of graphene beyond the quasiharmonic approximation,” *Phys. Rev. Lett.*, vol. 102, no. 4, pp. 2–5, 2009.
- [32] J. H. Los, K. V. Zakharchenko, M. I. Katsnelson, and A. Fasolino, “Melting temperature of graphene,” *Phys. Rev. B - Condens. Matter Mater. Phys.*, vol. 91, no. 4, pp. 1–6, 2015.
- [33] R. R. Nair *et al.*, “Fine structure constant defines visual transparency of graphene,” *Science (80-.)*, vol. 320, no. 5881, p. 1308, 2008.
- [34] K. F. Mak, M. Y. Sfeir, Y. Wu, C. H. Lui, J. A. Misewich, and T. F. Heinz, “Measurement of the optical conductivity of graphene,” *Phys. Rev. Lett.*, vol. 101, no. 19, pp. 2–5, 2008.
- [35] M. Holz, O. Kronenwerth, and D. Grundler, “Enhanced sensitivity due to current redistribution in the Hall effect of semiconductor-metal hybrid structures,” *Appl. Phys. Lett.*, vol. 86, no. 7, pp. 1–3, 2005.
- [36] T. H. Hewett and F. V Kusmartsev, “Extraordinary magnetoresistance: sensing the future,” *Cent. Eur. J. Phys.*, vol. 10, no. 3, pp. 602–608, 2012.
- [37] S. El-Ahmar and A. A. Pozniak, “Modeling the planar configuration of extraordinary magnetoresistance,” *J. Phys. D. Appl. Phys.*, vol. 48, p. 205101, 2015.

- [38] E. Stolyarova *et al.*, “High-resolution scanning tunneling microscopy imaging of mesoscopic graphene sheets on an insulating surface,” *Proc. Natl. Acad. Sci. U. S. A.*, vol. 104, no. 22, pp. 9209–9212, 2007.
- [39] M. Ishigami, J. H. Chen, W. G. Cullen, M. S. Fuhrer, and E. D. Williams, “Atomic structure of graphene on SiO₂,” *Nano Lett.*, vol. 7, no. 6, pp. 1643–1648, 2007.
- [40] J. Chen, C. Jang, S. Xiao, M. Ishigami, and M. S. Fuhrer, “Intrinsic and extrinsic performance limits of graphene devices on SiO₂,” *Nat. Nanotechnol.*, vol. 3, no. 4, pp. 206–9, 2008.
- [41] D. B. Farmer, V. Perebeinos, Y. M. Lin, C. Dimitrakopoulos, and P. Avouris, “Charge trapping and scattering in epitaxial graphene,” *Phys. Rev. B - Condens. Matter Mater. Phys.*, vol. 84, no. 20, pp. 1–5, 2011.
- [42] C. Dean *et al.*, “Graphene based heterostructures,” *Solid State Commun.*, vol. 152, no. 15, pp. 1275–1282, 2012.
- [43] K. I. Bolotin, K. J. Sikes, J. Hone, H. L. Stormer, and P. Kim, “Temperature-dependent transport in suspended graphene,” *Phys. Rev. Lett.*, vol. 101, no. 9, pp. 1–4, 2008.
- [44] K. I. Bolotin *et al.*, “Ultrahigh electron mobility in suspended graphene,” *Solid State Commun.*, vol. 146, no. 9–10, pp. 351–355, 2008.
- [45] P. J. Zomer, S. P. Dash, N. Tombros, and B. J. Van Wees, “A transfer technique for high mobility graphene devices on commercially available hexagonal boron nitride,” *Appl. Phys. Lett.*, vol. 99, no. 23, pp. 98–101, 2011.
- [46] P. J. Zomer, M. H. D. Guimarães, N. Tombros, and B. J. Van Wees, “Long-distance spin transport in high-mobility graphene on hexagonal boron nitride,” *Phys. Rev. B - Condens. Matter Mater. Phys.*, vol. 86, no. 16, pp. 2–5, 2012.
- [47] N. Petrone *et al.*, “Chemical vapor deposition-derived graphene with electrical performance of exfoliated graphene,” *Nano Lett.*, vol. 12, no. 6, pp. 2751–2756, 2012.
- [48] L. Wang *et al.*, “One-Dimensional Electrical Contact to a Two-Dimensional Material,” *Sci. (New York, N.Y.)*, vol. 342, no. November, pp. 614–617, 2013.
- [49] J. Dauber *et al.*, “Ultra-sensitive Hall sensors based on graphene encapsulated in hexagonal boron nitride,” *Appl. Phys. Lett.*, vol. 106, no. 19, 2015.

- [50] D. G. Purdie, N. M. Pugno, T. Taniguchi, K. Watanabe, A. C. Ferrari, and A. Lombardo, “Cleaning interfaces in layered materials heterostructures,” *Nat. Commun.*, vol. 9, no. 1, pp. 1–12, 2018.
- [51] X. Li *et al.*, “Large-Area Synthesis of High-Quality and Uniform Graphene Films on Copper Foils,” *Science (80-.)*, vol. 324, no. 5932, pp. 1312–1314, 2009.
- [52] P. Neugebauer, M. Orlita, C. Faugeras, A. L. Barra, and M. Potemski, “How perfect can graphene be?,” *Phys. Rev. Lett.*, vol. 103, no. 13, pp. 2–5, 2009.
- [53] D. C. Elias *et al.*, “Dirac cones reshaped by interaction effects in suspended graphene,” *Nat. Phys.*, vol. 7, no. 9, pp. 701–704, 2011.
- [54] A. K. Geim and K. S. Novoselov, “The rise of graphene.,” *Nat. Mater.*, vol. 6, no. 3, pp. 183–91, 2007.
- [55] T. Taniguchi and K. Watanabe, “Synthesis of high-purity boron nitride single crystals under high pressure by using Ba-BN solvent,” *J. Cryst. Growth*, vol. 303, no. 2, pp. 525–529, 2007.
- [56] I. Childres, L. Jauregui, W. Park, H. Cao, and Y. Chen, “Raman Spectroscopy of Graphene and Related Materials,” *New Dev. Phot. Mater. Res.*, pp. 1–20, 2013.
- [57] R. V. Gorbachev *et al.*, “Hunting for monolayer boron nitride: Optical and raman signatures,” *Small*, vol. 7, no. 4, pp. 465–468, 2011.
- [58] H. Zhang *et al.*, “Atomic force microscopy for two-dimensional materials: A tutorial review,” *Opt. Commun.*, vol. 406, no. March 2017, pp. 3–17, 2018.
- [59] “Handbook of Chemistry and Physics 100th Edition.” [Online]. Available: http://hbcponline.com/faces/documents/12_21/12_21_0002.xhtml. [Accessed: 17-Nov-2019].
- [60] S. M. Song, J. K. Park, O. J. Sul, and B. J. Cho, “Determination of work function of graphene under a metal electrode and its role in contact resistance,” *Nano Lett.*, vol. 12, no. 8, pp. 3887–3892, 2012.
- [61] F. Giubileo and A. Di Bartolomeo, “The role of contact resistance in graphene field-effect devices,” *Prog. Surf. Sci.*, vol. 92, no. 3, pp. 143–175, 2017.
- [62] Y. J. Yu, Y. Zhao, S. Ryu, L. E. Brus, K. S. Kim, and P. Kim, “Tuning the graphene work function by electric field effect,” *Nano Lett.*, vol. 9, no. 10, pp. 3430–3434, 2009.

- [63] X. Cui *et al.*, “Multi-terminal transport measurements of MoS₂ using a van der Waals heterostructure device platform,” *Nat. Nanotechnol.*, vol. 10, no. 6, pp. 534–540, 2015.
- [64] C. R. Dean *et al.*, “Hofstadter’s butterfly and the fractal quantum Hall effect in moiré superlattices,” *Nature*, vol. 497, no. 7451, pp. 598–602, 2013.
- [65] T. Uwanno, Y. Hattori, T. Taniguchi, K. Watanabe, and K. Nagashio, “Fully dry PMMA transfer of graphene on h-BN using a heating/ cooling system,” *2D Mater.*, vol. 2, no. 4, 2015.
- [66] A. Castellanos-Gomez *et al.*, “Deterministic transfer of two-dimensional materials by all-dry viscoelastic stamping,” *2D Mater.*, vol. 1, no. 1, 2014.
- [67] W. Pan *et al.*, “Biaxial compressive strain engineering in graphene/boron nitride heterostructures,” *Sci. Rep.*, vol. 2, pp. 2–7, 2012.
- [68] F. Pizzocchero *et al.*, “The hot pick-up technique for batch assembly of van der Waals heterostructures,” *Nat. Commun.*, vol. 7, no. May, 2016.
- [69] D. K. SCHRODER, *MATERIAL AND DEVICE SEMICONDUCTOR MATERIAL AND DEVICE Third Edition*, Third Edit. Hoboken, New Jersey: John Wiley & Sons, Inc., 2006.
- [70] H. Xu, L. Huang, Z. Zhang, B. Chen, H. Zhong, and L. M. Peng, “Flicker noise and magnetic resolution of graphene hall sensors at low frequency,” *Appl. Phys. Lett.*, vol. 103, no. 11, 2013.
- [71] “The Hall Effect | NIST.” [Online]. Available: <https://www.nist.gov/pml/engineering-physics-division/popular-links/hall-effect/hall-effect>. [Accessed: 01-Nov-2019].
- [72] A. A. Balandin, “Low-frequency 1/f noise in graphene devices,” *Nat. Nanotechnol.*, vol. 8, no. 8, pp. 549–555, 2013.
- [73] H. Wang, Y. Wu, C. Cong, J. Shang, and T. Yu, “Hysteresis of electronic transport in graphene transistors,” *ACS Nano*, vol. 4, no. 12, pp. 7221–7228, 2010.
- [74] C. J. Shih, G. L. C. Paulus, Q. H. Wang, Z. Jin, D. Blankschtein, and M. S. Strano, “Understanding surfactant/graphene interactions using a graphene field effect transistor: Relating molecular structure to hysteresis and carrier mobility,” *Langmuir*, vol. 28, no. 22, pp. 8579–8586, 2012.
- [75] S. Wang, Z. Jin, X. Huang, S. Peng, D. Zhang, and J. Shi, “Abnormal Dirac point shift in graphene field-effect transistors,” *Mater. Res. Express*, vol. 3, no. 9, 2016.

- [76] M. Marzano, A. Cultrera, M. Ortolano, and L. Callegaro, “A correlation noise spectrometer for flicker noise measurement in graphene samples,” *Meas. Sci. Technol.*, vol. 30, no. 3, 2019.
- [77] M. Kayyalha and Y. P. Chen, “Observation of reduced 1/f noise in graphene field effect transistors on boron nitride substrates,” *Appl. Phys. Lett.*, vol. 107, no. 11, 2015.
- [78] S. Rumyantsev, G. Liu, W. Stillman, M. Shur, and A. A. Balandin, “Electrical and noise characteristics of graphene field-effect transistors: Ambient effects, noise sources and physical mechanisms,” *J. Phys. Condens. Matter*, vol. 22, no. 39, 2010.
- [79] Z. M. Liao, B. H. Han, Y. B. Zhou, and D. P. Yu, “Hysteresis reversion in graphene field-effect transistors,” *J. Chem. Phys.*, vol. 133, no. 4, 2010.
- [80] Y. G. Lee *et al.*, “Fast transient charging at the graphene/ SiO₂ interface causing hysteretic device characteristics,” *Appl. Phys. Lett.*, vol. 98, no. 18, pp. 98–101, 2011.
- [81] H. Xu, J. Wu, Y. Chen, H. Zhang, and J. Zhang, “Substrate engineering by hexagonal boron nitride/sio₂ for hysteresis-free graphene FETs and large-scale graphene p-n junctions,” *Chem. - An Asian J.*, vol. 8, no. 10, pp. 2446–2452, 2013.
- [82] T. Lohmann, K. Von Klitzing, and J. H. Smet, “Four-Terminal magneto-Transport in graphene p-n junctions created by spatially selective doping,” *Nano Lett.*, vol. 9, no. 5, pp. 1973–1979, 2009.
- [83] J. Moser, A. Barreiro, and A. Bachtold, “Current-induced cleaning of graphene,” *Appl. Phys. Lett.*, vol. 91, no. 16, pp. 1–4, 2007.
- [84] S. K. Jang, J. Jeon, S. M. Jeon, Y. J. Song, and S. Lee, “Effects of dielectric material properties on graphene transistor performance,” *Solid. State. Electron.*, vol. 109, pp. 8–11, 2015.
- [85] H. Ramamoorthy and R. Somphonsane, “In-situ current annealing of graphene-metal contacts,” *J. Phys. Conf. Ser.*, vol. 1144, no. 1, 2018.
- [86] K. Nagashio, T. Nishimura, K. Kita, and A. Toriumi, “Contact resistivity and current flow path at metal/graphene contact,” *Appl. Phys. Lett.*, vol. 97, no. 14, pp. 8–11, 2010.
- [87] E. Watanabe, A. Conwill, D. Tsuya, and Y. Koide, “Low contact resistance metals for graphene based devices,” *Diam. Relat. Mater.*, vol. 24, pp. 171–174, 2012.

- [88] A. Di Bartolomeo *et al.*, “Charge transfer and partial pinning at the contacts as the origin of a double dip in the transfer characteristics of graphene-based field-effect transistors,” *Nanotechnology*, vol. 22, no. 27, 2011.
- [89] J. A. Robinson *et al.*, “Contacting graphene,” *Appl. Phys. Lett.*, vol. 98, no. 5, pp. 96–99, 2011.
- [90] M. H. Khan *et al.*, “Few-atomic-layered hexagonal boron nitride: CVD growth, characterization, and applications,” *Mater. Today*, vol. 20, no. 10, pp. 611–628, 2017.
- [91] M. Holz, O. Kronenwerth, and D. Grundler, “Magnetoresistance of semiconductor-metal hybrid structures: The effects of material parameters and contact resistance,” *Phys. Rev. B*, vol. 67, no. 19, p. 195312, 2003.
- [92] K. Gopinadhan *et al.*, “Extremely large magnetoresistance in few-layer graphene/boron–nitride heterostructures,” *Nat. Commun.*, vol. 6, p. 8337, 2015.
- [93] H. Zhong, Z. Zhang, H. Xu, C. Qiu, and L. M. Peng, “Comparison of mobility extraction methods based on field-effect measurements for graphene,” *AIP Adv.*, vol. 5, no. 5, 2015.
- [94] Y. Jia *et al.*, “Toward High Carrier Mobility and Low Contact Resistance: Laser Cleaning of PMMA Residues on Graphene Surfaces,” *Nano-Micro Lett.*, vol. 8, no. 4, pp. 336–346, 2016.
- [95] H. Zhong *et al.*, “Realization of low contact resistance close to theoretical limit in graphene transistors,” *Nano Res.*, vol. 8, no. 5, pp. 1669–1679, 2015.
- [96] F. Guinea, “Charge distribution and screening in layered graphene systems,” *Phys. Rev. B - Condens. Matter Mater. Phys.*, vol. 75, no. 23, pp. 1–7, 2007.
- [97] T. Cusati *et al.*, “Electrical properties of graphene-metal contacts,” *Sci. Rep.*, vol. 7, no. 1, pp. 1–11, 2017.
- [98] L. Anzi *et al.*, “Ultra-low contact resistance in graphene devices at the Dirac point,” *2D Mater.*, vol. 5, no. 2, 2018.
- [99] S. Min Song, T. Yong Kim, O. Jae Sul, W. Cheol Shin, and B. Jin Cho, “Improvement of graphene-metal contact resistance by introducing edge contacts at graphene under metal,” *Appl. Phys. Lett.*, vol. 104, no. 18, 2014.
- [100] “Nervous Tissue - Anatomy and Physiology - OpenStax.” [Online]. Available: <https://openstax.org/books/anatomy-and-physiology/pages/12-2-nervous-tissue>. [Accessed: 07-Nov-2019].

[101] “Communication Between Neurons - Anatomy and Physiology - OpenStax.” [Online]. Available: <https://openstax.org/books/anatomy-and-physiology/pages/12-5-communication-between-neurons>. [Accessed: 07-Nov-2019].

PUBLICATIONS

A. R. Monroy-Pelaez, A. Llacsahuanga, Y. P. Chen, and E. Marinero, Graphene-based magnetometers: magnetic resolution dependence on material properties and fabrication, *Materials Chemistry and Physics*.

A. R. Monroy-Pelaez, A. Kildishev, and E. Marinero, Towards pT sensitivity in graphene-based EMR devices at room temperature, predictive studies using FEM simulations, *IEEE Sensors Journal*.

A. R. Monroy-Pelaez, H. Fowler, L. Regalado, E. Rogers, R. Shi, and E. Marinero, Graphene-based magnetometers for biomagnetic signal detection: opportunities and challenges, *IEEE Sensors Journal*